ISAS - INTERNATIONAL SCHOOL
FOR ADVANCED STUDIES

The X-ray Properties of Blazars

Thesis submitted to the
International School for Advanced Studies, Trieste, Italy
- Astrophysics Sector -
in partial fulfillment of the requirements for the degree of

Philosophiæ Doctor

CANDIDATE

Rita M. Sambruna

SUPERVISORS

Prof. Laura Maraschi
Prof. Aldo Treves
Dr. C. Meg Urry

October 1994

TRIESTE

**SISSA - SCUOLA
INTERNAZIONALE
SUPERIORE
DI STUDI AVANZATI**
TRIESTE
Strada Costiera 11

To Joseph

and

To Elena

ABSTRACT

Rosat pointed observations of a complete sample of radio-selected BL Lacs (RBLs) have been analyzed. The 0.15 – 2.0 keV energy distributions of RBLs are well fitted by a single power law model with Galactic absorption; for three bright sources more complex spectral shapes are indicated. The Rosat energy distributions of RBLs are broad, spanning a large range of photon indices (1 – 3). No differences are found comparing the Rosat spectral index distributions of RBLs and those of X-ray selected BL Lacs (XBLs), while both classes have steeper Rosat spectra than Flat Spectrum Radio Quasars (FSRQs). A reanalysis of the *Einstein* IPC data indicates that RBLs have flatter spectra in the range 0.3 – 3.5 keV than in the Rosat range. The Rosat photon indices correlate with the redshifts for the three classes together. Within the single class, a correlation is present between the Rosat and the radio flux density.

The multifrequency spectra of the three Blazar samples have been studied. Radio-selected objects are characterized by steep radio-to-optical continua, while in X-ray selected sources the bulk of the emission is at higher energies (UV/soft X-rays). We found that the radio-to-optical spectral index is correlated with the shape of the X-ray continuum and with the bolometric luminosity and/or redshift, and that the three classes have different spectral properties but form a continuous sequence rather than separate populations.

The radio to X-ray emission of Blazars has been interpreted using homogeneous and inhomogeneous Synchrotron-Self Compton models. It is shown that the observed differences of the three classes can not be reconciled within the beaming scheme in terms of different orientation of the jet only. Rather, a spread of intrinsic parameters is required, with X-ray selected objects having higher magnetic fields and smaller dimensions than the radio-selected ones. We conclude that, from the point of view of their continuum emission, Blazars form a unique population dominated by the same emission mechanism operating on different physical scales.

Acknowledgements

This Thesis contains the results of the work performed at the Space Telescope Science Institute during the last year of my PhD program. Thus, as a first thing, I want to thank Profs. Sciama and Treves for allowing me to work abroad, and for always supporting me in my scientific interests, and Dr. A. Wilson and Prof. Nino Panagia for enrolling me in the graduate student program at the Institute.

STScI is really an excellent place to do science. A big thanks to the whole STScI staff for creating a stimulating and efficient environment. In particular, thanks to Jamie Lipinski, Alex Framarini, Harry Payne, and all the computer assistants for being so available and nice at any time I needed help.

I had many inputs (scientific and non) during the morning science coffees, of whom Mario Livio is the perfect host. Among all, Kirk Korista, Mike Eracleous, Anne Kinney, Brian Espey were pleasant companions.

I really enjoyed every moment of my PhD research time; I hope that all the fun I had will accompany me along my entire career in Astronomy. However, things would have been not so good without the many friends and colleagues, both at STScI and at SISSA, with whom I shared scientific and less scientific times.

Among them, it's a pleasure to thank the other graduate students at STScI (Jesus Burgos, Guido De Marchi, Jack Gallimore, Varsha Kulkarni, John Mulchaey, Paola Sartoretti, Eline Tolstoy, Fang Zhou), with whom I shared the "bunker" offices in the Ground floor, promptly renamed the Great floor; Jon Saken for the discussions about the wonders of IDL versus IRAF, Colorado versus Maryland, and for the many car rides; Mike Eracleous for loving soccer; Michael Dahlem for not loving soccer; Alberto Conti and Francesca Primas for dreaming American; Anna Pasquali for the evenings with her, me, and *The Fugitive.* Thank

you Elena Pian and Paolo Catelan for sharing the office, the science, and the tea bags during my first three years at SISSA.

Thanks to Gabriele Ghisellini for explaining me the mysteries of the accelerating jets and for providing me his code, and to Paolo Padovani for the discussions about the correlation analysis;

Thank you my good friend Ron Kollgaard for your patience with my continuous questions about "radio stuff";

Thank you Greg Madejski for introducing the wonders of Washington (and for things more scientific);

Thank you Paul Haines for your friendship. We all hope that you will finally come back to the States, one day.

Thanks to Antonio Lanza, John Miller, Massimo Persic, Paolo Salucci, Mike Smith, who with their teaching contributed to the growth of my culture.

A special thanks to Diane Gilmore, a real IRAF expert, who taught me everything about the reduction and analysis of the Rosat data. I will never forget that Diane gave me her house at the beginning of my stay in Baltimore, and hanged around with me looking for apartments until I found one.

Thanks also to Jane Turner and Ian George, who always promptly assisted me with IRAF and Rosat. Karen Smale was most helpful with advice and assistance.[1]

I saved the biggest thanks to the end. My deep, deep gratitude to Laura Maraschi and Meg Urry. Without their support, teaching, discussions, and friendship, simply I wouldn't make it. They have always been there for me every time I needed them; to clarify and develop ideas, to solve doubts (many) and crises.

---

[1] I would also like to acknowledge the use of data obtained through the High Energy Astrophysics Science Archive Research Center Online Service, provided by the NASA-Goddard Space Flight Center.

But I feel I owe them more than science. With their example, they both showed me that it is possible to be an astronomer *and* to have a normal life, including a family. I'm lucky enough that I can think of them as my friends.

With Meg's family (Andy, Amelia, Sophia) I spent many wonderful, relaxing hours. Thank you all for being our, Joseph's and mine, "adoptive" family and also for allowing us to have a garden.

Joseph has been a continuous source of strength during all these years. My eternal gratitude, and much more, for all his patience and love.

The final thought is for my family in Italy, in particular for my sister Elena. This Thesis is also dedicated to her memory.

CONTENTS

TABLES

FIGURES

The X-ray Properties of Blazars

CHAPTER I

Blazars: an Enigmatic Class of Active Galactic Nuclei

1.1 Observational Traits of Blazars

Among Active Galactic Nuclei (AGNs), Blazars are characterized by the most rapid variability at all observed frequencies. Other fundamental observational traits of Blazars are the high luminosities, the polarization of the radio and optical light ($> 3\%$), and the compactness of the radio emission. Depending on the presence and strength of emission lines, Blazars are classified as BL Lacertae objects (BL Lacs in the following) when they have absent or weak emission lines. Blazars with strong and broad emission lines are variously classified as Highly Polarized Quasars (HPQs), Optically Violently Variable Quasars (OVVs), Core Dominated Quasars (CDQs), or Flat Spectrum Radio Quasars (FSRQs). Here we refer to strong-lined Blazars as FSRQs. The strength of the emission lines is the only commonly accepted criterion to distinguish the quasar-like Blazars from BL Lacs, although this distinction remains arbitrary because of the variability of the continuum (e.g., Antonucci 1993). There are a few transitional objects, that is, objects originally classified as BL Lacs which were later observed to have strong and broad emission lines during, presumably, states of faint continuum emission (e.g., Stickel et al. 1991).

BL Lacs and FSRQs share the properties of a non-thermal continuum emission. A non-thermal origin was originally suggested by the first measurements in the radio band, implying compact emission regions with characteristic brightness temperatures $\sim 10^{12}$ °K, and in some cases even more (e.g., Ghisellini et al. 1993). The most natural interpretation, which also accounted for the observed polarization, was synchrotron emission. The smooth continuum of Blazars, which extends from radio to UV frequencies, suggested that the synchrotron mechanism was responsible for the emission up to at least 10^{15} Hz.

It was immediately realized that due to the high particle and radiation densities in the region(s) emitting in the radio, the radio photons should have been up-scattered to X-ray frequencies by the relativistic electrons (Synchrotron-Self Compton, SSC). In fact, since the first X-ray satellites were launched, Blazars were recognized to be X-ray emitters (e.g., Schwartz et al. 1978; Piccinotti et al. 1982). However, the Self-Compton flux calculated turned out to exceed the observed X-ray flux by many orders of magnitude ("Compton catastrophe"), a paradox resolved by assuming relativistic motion of the emitting plasma, so that the observed fluxes would be overestimated by Doppler-enhancement and the variability timescales would appear shorter (Marscher et al. 1979; Urry & Mushotzky 1982).

The recent detection of several Blazars at γ-ray energies, with high luminosities and rapid variabilities (Fichtel et al. 1993; Hartman et al. 1993) provided further support for the presence of relativistic motion in this class of objects. Independent of the model for the production of γ-rays, the requirement of transparency of the emission region to pair production through photon-photon interactions leads to a lower limit for the Doppler factor. For example, for 3C 279, the brightest γ-ray source in the sky, a lower limit of ~ 5 is derived from the observed luminosity and variability (Maraschi, Ghisellini, & Celotti 1992).

It is also remarkable that in many cases γ-rays dominate the energy output of Blazars, at least in the high state (e.g., Maraschi, Ghisellini, & Celotti 1994). Variability in the γ-rays is however a common property of Blazars, with a duty cycle (i.e., fraction of the time spent in the high state) probably less than 100%. Current models identify the production mechanism of γ-rays in Blazars as the Compton up-scattering of synchrotron UV photons internal to the source (Maraschi et al. 1992), or of ambient X-ray photons (Blandford 1993), or also UV photons coming from thermal emission from an accretion disk (Dermer & Schlickeiser 1993) and/or the regions responsible for the emission lines (Sikora, Begelman, & Rees 1994).

1.2 Models for Blazars

1.2.1 THE BEAMING MODEL

One of the most popular views about Blazars is the beaming model (from an original idea of Blandford & Rees 1978). The observational properties of the continuum are explained assuming that the radiation arises via the SSC mechanism, probably in an elongated structure (a jet) pointing toward the observer, in a cone of of semiangle $\sim \frac{1}{\Gamma_{\rm B}}$, where $\Gamma_{\rm B}$ is the bulk Lorentz factor of the emitting plasma.

Further evidence suggested inhomogeneity of the jet, that is, magnetic fields and particle densities varying along the jet, which can be thought of as "blobs" of plasma emitting locally via SSC. It is also believed that an acceleration mechanism of the blobs can explain some observed properties of the continuum emission (see below). Several classes of smooth inhomogeneous jet models have been developed so far (Marscher 1980; Königl 1981; Ghisellini, Maraschi, &

Treves 1985; Hutter & Mufson 1986; Ghisellini & Maraschi 1989), differing in the initial assumption about the jet geometry and the parameterization of the physical quantities and their variations along the jet. For reviews of these models see Urry (1988), Maraschi (1992), and Kollgaard (1994). A particular jet model will be discussed in Chapter 6.

The beaming hypothesis implies the existence of a "parent population", that is, intrinsically similar objects with the jet pointing at large angles with respect to the observer. The beaming unification scheme indicates the Fanaroff-Riley I and II radio galaxies as the parent populations of BL Lacs and FSRQs, respectively (Browne 1983; Barthel 1989; Padovani & Urry 1990, 1991), although the distinction may not be so sharp (Kollgaard et al. 1992).

It appears that BL Lacs are found in rich clusters of galaxies (Ulrich 1978; Smith, O'Dea, & Baum 1993; Stickel, Fried, & Kühr 1993; Wurtz et al. 1993; Falomo, Pesce, & Treves 1993a, 1993b, 1994; Pesce, Falomo, & Treves 1994), and that they frequently have close companions (e.g., Falomo et al. 1991; Falomo, Pesce, & Treves 1994), possibly suggesting that the BL Lac phenomenon can be related to the galaxy interactions. Moreover, the comparison of the enviroments of the BL Lacs and of their presumed parent objects provides an independent method to verify the beaming hypothesis.

1.2.2 THE GRAVITATIONAL MICROLENSING MODEL

An alternative explanation of Blazars is provided by the gravitational microlensing hypothesis (Ostriker & Vietri 1985, 1990), according to which BL Lacs are the images of distant quasars lensed by the stars in a foreground galaxy. In this hypothesis, the continuum emission would be amplified (by a factor $\sim$

10) with respect to the emission lines, because of a preferential amplification of the spatially smaller continuum emitting region.

There is growing evidence that this model can not explain BL Lacs as a class. Padovani (1992a) calculated the mean amplification factor for the optical fluxes of a complete sample of BL Lacs, and showed that this should be of order unity, while a mean factor of order 10 is required by the model. Gabuzda et al. (1989, 1992) showed that the polarization structure of a sample of BL Lacs is fundamentally different than for HPQs, the former having a polarization angle preferentially oriented in a direction parallel to the VLBI axis, while in HPQs it is oriented perpendicularly. BL Lacs and FSRQs seem to differ also in their X-ray energy distributions (Worrall & Wilkes 1990; Sambruna et al. 1994a), which should not be affected by microlensing unless a substantial fraction of the X-ray emission is extended.

These arguments suggest that BL Lacs and FSRQs are intrinsically different classes, which can not be reconciled in the context of gravitational microlensing. However, microlensing may be important in some *single* sources (e.g., Stickel et al. 1991).

1.2.3 THE EVOLUTIONARY UNIFIED MODEL

Based on the analysis of the radio-optical counts of FSRQs and (a small number) of BL Lacs, the evolutionary unified model (Vagnetti, Giallongo, & Cavaliere 1991; Vagnetti & Spera 1994) postulates that BL Lacs are the products of the evolution of FSRQs (a sort of "quasar-remnant"), as an effect of the cosmological increase of the beamed component with respect to the "isotropic" component, responsible for the emission lines, in the sense of a higher beaming factor with decreasing redshift. The implications for the parent populations would predict an evolutionary link between FRI and FRII (Vagnetti & Spera 1994), which seems improbable given the higher numerical density of FRI.

This model tries, in particular, to account for the presence among Blazars of objects which are "transitional", having BL Lac properties and strong emission lines. However, the sample of FSRQs used by Vagnetti et al. (1991) included several Blazars later re-classified as BL Lacs and appearing in complete samples (Stickel et al. 1991). In fact, a test of the model on the basis of radio and optical data for two complete samples of BL Lacs and FSRQs (Padovani 1992a) showed that the predicted optical evolution of BL Lacs is inconsistent with that of FSRQs. In addition, very strong evolution would be implied by the unbeamed properties of the two sample, like, for example, the distributions of the extended radio components. Padovani also showed that BL Lacs are intrinsically weaker in line luminosity with respect to FSRQs, although he compared a very small number of objects at different redshifts.

Moreover, the distributions of the Doppler factors of the two classes seem in disagreement with the expectations of the model, BL Lacs being characterized on average by smaller factors than quasars (Ghisellini et al. 1993). However, the values of the beaming factor derived from the SSC are only lower limits; in addition, the samples studied in this analysis were formed by all the Blazars for which published VLBI and X-ray fluxes were available, thus possibly being affected by biases toward the sources with higher enhancement factors.

1.3 Radio-selected and X-ray Selected BL Lacs

BL Lacs were originally discovered through their radio emission (e.g., Stein, O'Dell, & Strittmatter 1976). These earlier "samples" of BL Lacs required a non-thermal continuum emission, no emission lines, high luminosity and rapid variability, high and variable degree of polarization, for the classification of an object as a BL Lac. The same criteria basically applied also for the objects first discovered in X-ray surveys (Piccinotti et al. 1982; Schwartz & Ku 1983).

A more quantitative definition of radio- and X-ray selected objects can be given on the basis of the ratio of the X-ray-to-radio flux (Ledden & O'Dell 1985; Stocke et al. 1985). "X-ray normal" and "X-ray strong" BL Lacs were found to have different broad band continua, with X-ray normal Blazars (the majority at that time) having steeper radio-to-optical and radio-to-X-rays continua than X-ray strong objects, considered "less representative" of the class.

The subsequent X-ray surveys increased the number of known BL Lacs. X-ray searches proved to be more efficient in finding BL Lacs (Piccinotti et al. 1982; Remillard et al. 1990; Giommi et al. 1991; Stocke et al. 1991), in particular when combined with radio and optical measurements (Schachter et al. 1993), than those in the radio (Kühr & Schmidt 1990; Stickel et al. 1991) or in the optical (Fleming et al. 1993).

X-ray selected (XBLs) and radio-selected (RBLs) BL Lacs were observed to differ in many properties, in addition to the continuum shape. XBLs outnumber RBLs of equal X-ray flux by a factor $\gtrsim 10$ (Urry, Padovani, & Stickel 1991), and are distributed at lower redshifts than RBLs, with a negative evolution (e.g., Celotti et al. 1993; Wolter et al. 1994, and references therein). Also, XBLs have lower variability and degree of polarization, higher starlight fraction in their optical spectra, and flatter radio to UV energy distributions than RBLs (Stocke et al. 1985; Ghisellini et al. 1986; Pian & Treves 1993; Jannuzi, Green, & French 1993), while the X-ray luminosity distributions do not differ significantly (Maraschi et al. 1986).

Recent analysis of the broad-band energy distributions showed that the radio to X-ray continua of RBLs and XBLs can be described by two power laws (Pian et al. 1994a), with a peak of the emission which is located at different frequencies for the two classes (Giommi, Ansari, & Micol 1994). XBLs are characterized by a peak of the synchrotron output at 10^{15-16} Hz, while the bulk of the emission in RBLs and FSRQs is at lower frequencies, typically IR/Optical. In addition, a second rising component, identified with the Compton component and extending to γ-rays, would be more predominant in the radio-selected Blazars (Maraschi, Ghisellini, & Celotti 1994).

Thus, fundamental observational distinctions characterize the X-ray selected from the radio-selected Blazars. How can these different properties be explained? Are we looking at *intrinsically* different populations?

1.4 Interpreting the RBL/XBL phenomenon

Because RBLs do not differ from XBLs in the distributions of the X-ray luminosities, while they are more luminous at the lower frequencies, the X-ray surveys should not discriminate among the two types of BL Lacs, leading to the conclusion that XBLs are intrinsically more numerous than RBLs (Maraschi et al. 1986). Moreover, analysis of the luminosity functions of XBLs and RBLs relative to low-luminosity radio galaxies led to the conclusion that the radio emission is more beamed than the X-rays (Urry et al. 1991).

The higher beaming of the radio emission can be the result of an increasing Lorentz factor and/or collimation along the jet (Ghisellini & Maraschi 1989, Celotti et al. 1993). In this scheme, RBLs and XBLs are the same intrinsic phenomenon seen at different viewing angles. XBLs should be the objects oriented at large angles ($\sim 15^\circ - 30^\circ$; e.g., Urry & Padovani 1994),[1] with a greater probability of being intercepted by the observer. RBLs and FSRQs would be the more aligned ($\sim 10^\circ - 15^\circ$) counterparts, and the emission coming from the external regions in these objects is enhanced with respect to XBLs. The Compton component, which is related to the beaming, would be directly intercepted, leading to the prediction that RBLs should have flatter distributions than XBLs in the X-ray band.

An alternative scheme has been recently put forward by Giommi & Padovani (1994) and Padovani & Giommi (1994), based on the observed difference in the multiwavelength spectra of the two classes. Based on the assumption that the spread in the position of the synchrotron peak is intrinsic, and calculating the X-ray number counts of XBLs starting from the radio counts of RBLs, the authors show that RBL-like sources should be more numerous that XBL-like ones. In other words, the observed RBLs come from a higher luminosity tail of the radio luminosity function; however, going down to radio luminosities comparable to those of XBLs, it is predicted that RBLs would be more numerous than XBLs. Therefore, the present higher overabundance of the latter would be due to the fact that the limiting thresholds of the current X-ray surveys happened to be just below the peak of their spectra. Deeper surveys (like the Rosat All Sky Survey) would be expected to pick more objects with RBL-like behavior.

The beaming model starts from the observational findings that the X-

---

[1] Technically, an XBL is seen at angles spanning the entire range $0^\circ - 30^\circ$.

ray luminosities of RBLs and XBLs are the same, and that the latter are less luminous at the lower frequency. The prediction is that XBLs are more abundant than RBLs. The opposite result is obtained in the Giommi & Padovani model, which, curiously, is based on a similar observational scenario. While the solution seems to reside in deeper X-ray and radio surveys, the fundamental question, common to both models, is now the origin of the observed spread of the continuum shape in the two classes.

1.5 X-ray Studies of Blazars

The X-ray band turns out to be critical to the models discussed above, in that it is the range where the synchrotron and Compton components overlap, and so their relative contribution to the overall spectrum can be quantified. In addition, the recent detections of several Blazars in the γ-ray band makes the study of the production of the high energies even more important.

Different variability and spectral behavior is expected in the context of the predominance of the synchrotron or IC mechanisms. The two processes can also coexist in individual objects or statistically in classes of objects. In this context, the systematic studies of the X-ray properties of classes of Blazars are clearly relevant.

Previous analysis of Blazars in X-rays relied mainly on the data gathered with the *Einstein*, EXOSAT, and GINGA satellites, and on heterogeneous "samples" of objects. The first cumulative studies of the average energy distributions of 13 BL Lacs, observed with the *Einstein* Imaging Proportional Counter in $0.2 - 3.5$ keV, yielded an average photon index of ~ 2.1 (Madejski & Schwartz 1989). A mean of ~ 2.5 was obtained by Maraschi & Maccagni (1988), who reviewed the EXOSAT results obtained in 0.1 – 10 keV for a total of 12 BL Lacs by different authors. Compared to other AGNs, BL Lacs turned out to have the steepest X-ray slopes observed. For example, Seyfert galaxies, radio-loud and radio-quiet quasars studied at energies $\gtrsim$ 2 keV have mean slopes of 1.7, 1.6, and 1.9, respectively (Turner & Pounds 1989; Lawson et al. 1992).

Different X-ray energy distributions also seem to be present for the different Blazar classes. A first report by Ohashi (1989) of results obtained from the GINGA data, based however on only 3 XBLs and 2 RBLs, yields mean photon indices of $\gtrsim$ 2.7 and $\sim$ 1.8, respectively, in the 2 – 35 keV range. An interesting comparison for a larger group of Blazars was performed by Worrall & Wilkes (1990), on the basis of data obtained with the *Einstein* IPC for a group of 12 HPQs, 19 CDQs, 24 RBLs, and 6 XBLs. The X-ray slopes of HPQs and CDQs were found to be distributed around the same mean photon index ($\sim$ 1.5), while a steeper value, $\sim$ 2.0, was derived for both RBLs and XBLs.

The EXOSAT satellite observed 21 Blazars (11 XBLs, 5 RBLs, and 5 HPQs) with statistics high enough to allow spectral analysis in 0.1 – 10 keV (Sambruna et al. 1994a,b). XBLs were found to have steeper average spectra than HPQs (mean photon index 2.49 ± 0.32 and 1.50 ± 0.17, respectively). The distribution for RBLs had a mean around 1.88, but with a wide spread ($\pm$ 0.63).

The picture emerging is that of a clear division in X-ray energy distributions between XBLs and FSRQs, the former having steeper X-ray slopes than the latter, with RBLs somewhat intermediate. This suggests that FSRQs and RBLs are more dominated by an SC component in their X-ray emission than XBLs.

For XBLs, the steepness of the X-ray spectra suggests a synchrotron origin. This interpretation is qualitatively supported by the observational evidence that the spectra of XBLs steepen at the higher energies (convex spectra; Barr, Giommi, & Maccagni 1988; Barr et al. 1989; Madejski & Schwartz 1989; Garilli & Maccagni 1990; Sambruna et al. 1993; Sembay et al. 1993; Sambruna et al. 1994a,b), and by the spectral variability (a flattening of the spectrum when the intensity increases; George, Warwick, & Bromage 1988; Giommi et al. 1990; Sambruna et al. 1994a).

In conclusion, the X-rays are a powerful diagnostic of the physics of Blazars. Important information about the geometrical and physical condition of the jet have been provided by comparing the statistical properties of XBLs, RBLs, and HPQs. Unfortunately, all this information relied on inhomogeneous, inconsistently defined groups of objects, and on data often of poor statistics. The Rosat satellite, launched in 1990, offered the unique opportunity to study the X-ray properties of complete samples of radio- and X-ray selected Blazars in a soft energy range (0.1 – 2.0 keV), with higher spectral resolution and lower internal background compared to previous experiments. The only two complete, large samples of RBLs and XBLs defined at that time were the 1 Jy sample of RBLs of Stickel et al. (1991) and the sample of XBLs discovered by the *Einstein* Extended Medium Sensitivity Survey (Stocke et al. 1991; Morris et al. 1991).

This dissertation contains the results of the analysis of the Rosat data for the RBL sample. It can be divided in two parts. First, the energy distribution obtained for the complete sample of RBLs in the Rosat range is presented, using various methods. The RBL spectral properties are then compared to those of the EMSS XBLs (Perlman 1994, and related papers), and of a complete samples of FSRQs observed by Rosat, available in the literature. The *Einstein* IPC data are also reconsidered in light of the Rosat observations for the three samples. In addition, the Rosat spectra of the brightest sources are analyzed in more detail, with particular care for the effects of the still poorly calibrated problems of the detector.

In the second part of the Thesis we examine the implications of the Rosat data with respect to the emission at the lower energies, comparing the two-points spectral indices of RBLs with those of the other Blazar classes, and correlating the broad-band indices with other physical quantities. Specific theoretical models are used to interpret the results in the attempt to quantify the more relevant physical quantities characterizing the emission in the various Blazar classes.

CHAPTER II

Rosat Observations of Radio-Selected BL Lacs

2.1 The 1 Jy Sample of RBLs

2.1.1 DEFINITION CRITERIA

A sample of RBLs was drawn from the complete catalog of radio sources stronger than 1 Jy at 5 GHz of Kühr et al. (1981) with the following selection criteria (Stickel et al. 1991):

1) the source has a flat radio spectrum, $\alpha_r \geq -0.5$ ($S_\nu \propto \nu^{\alpha_r}$);

2) the optical counterpart is brighter than V=20 mag on the Sky Survey Plates;

3) Any emission line in the optical spectrum has a rest-frame equivalent width (EW) < 5 Å.

Thirty-four sources were found to fulfill these requirements, with the addition of nine RBL candidates (objects satisfying criteria 1 and 2 but for which spectroscopy was missing). All objects, except two, were also found to be strongly polarized ($>$ 3 %), thus satisfying one of the "historical" observational characteristics of this class of AGN.

As discussed in Stickel et al., the more delicate of the selection criteria listed above is the strength of the emission lines. Criterion 3 above is the only one commonly accepted to distinguish a BL Lac from an HPQ/OVV, but the situation is not always unambiguous. As is known, several objects were seen to show emission lines similar to quasars when they were observed in states of minimum light. The crucial point here is that the detection of strong lines in the optical spectra may be strongly dependent on the variable strength of the continuum emission and on the signal-to-noise of the available spectroscopy. Repeated high-quality spectroscopy for BL Lacs, although ideal, is impractical for the large amount of telescope time required. To avoid biasing the sample against more observed objects, criterion 3 was applied to the first optical spectrum obtained for each object. This led to the retention of objects considered "borderline", like 0235+164, 0537–441, 1308+326, in the sample.

For 25 out of 34 RBLs precise measurements of redshift are available from Stickel et al. The redshift of 0454+844 was recently measured (z=0.112; Brunner et al. 1994 and reference therein), as was a more refined lower limit for another one, 0716+714 ($z > 0.3$). For the remaining objects, in four cases there are lower limits obtained from intervening absorption systems and in another four cases the redshift is still unknown. The redshift distribution of the 1 Jy RBLs is shown in Figure 2.1 (upper panel). As Stickel et al. note it is uniform up to $z \sim 1$, with an average $\langle z \rangle = 0.56$. In the radio band, RBLs show positive evolution, with $\langle V/V_{max} \rangle = 0.60 \pm 0.05$ (Stickel et al. 1991).

Interestingly, three RBLs of the 1 Jy sample (0235+164, 0537–441, and 0716+714) are among the strongest extragalactic γ-ray sources observed with the EGRET instrument on GRO, sensitive in the energy range 100 MeV – 10 GeV. [1] For another object, 2005–489, a marginal γ-ray detection at energies $E \geq$ 100 MeV is given, while for all the remaining sources a 2σ upper limit is present in the EGRET database.

The criteria used to select the RBLs of the 1 Jy sample are similar

---

[1] Only one XBL, Mrk 421, presently has a positive detection in γ-rays.

to those used to define the XBLs of the *Einstein* Extended Medium Sensitivity Survey (EMSS; Gioia et al. 1990; Stocke et al. 1991), thus providing us with two complete samples of RBLs and XBLs self-consistently defined and of comparable sizes. Beside criterion 3 above, an additional criterion was used to select the BL Lac objects from the EMSS. As evidence for a non-thermal continuum, a CaII break smaller than 25% in the spectra of the optical counterparts (the usual value for an elliptical galaxy is 50%) was required. Morris et al. (1991) extracted a complete sample of 22 XBLs by adding the further constraints in flux ($F_x \geq 5 \times 10^{-13}$ ergs cm^{-2} s^{-1}) and declination ($\delta \geq -20^\circ$). The EMSS XBLs turned out to be more nearby than RBLs, with a redshift distribution peaked at $\langle z \rangle = 0.305$ (Figure 2.1, lower panel), with negative evolution in the X-ray band (Morris et al. 1991).

The different evolution properties of RBLs and XBLs have been recently confirmed by the reanalysis of their luminosity functions in radio, optical, and X-rays by Celotti et al. (1993) and Wolter et al. (1994). It is also shown that RBLs are rarer objects in X-rays and optical, while in radio the number counts of the two classes are similar, although XBLs are less luminous.

2.1.2 THE 1 JY RBLS VERSUS EMSS XBLS AND OTHER BLAZAR CLASSES

In recent years, several authors studied the properties of the 1 Jy RBLs in radio, IR, and optical and compared them to those of the EMSS XBLs and available samples of HPQ/OVVs.

Padovani (1992b) examined the distributions of the radio, optical, and X-ray luminosities of the 1 Jy RBLs and the EMSS XBLs using data collected from the literature. He found that RBLs are systematically more luminous

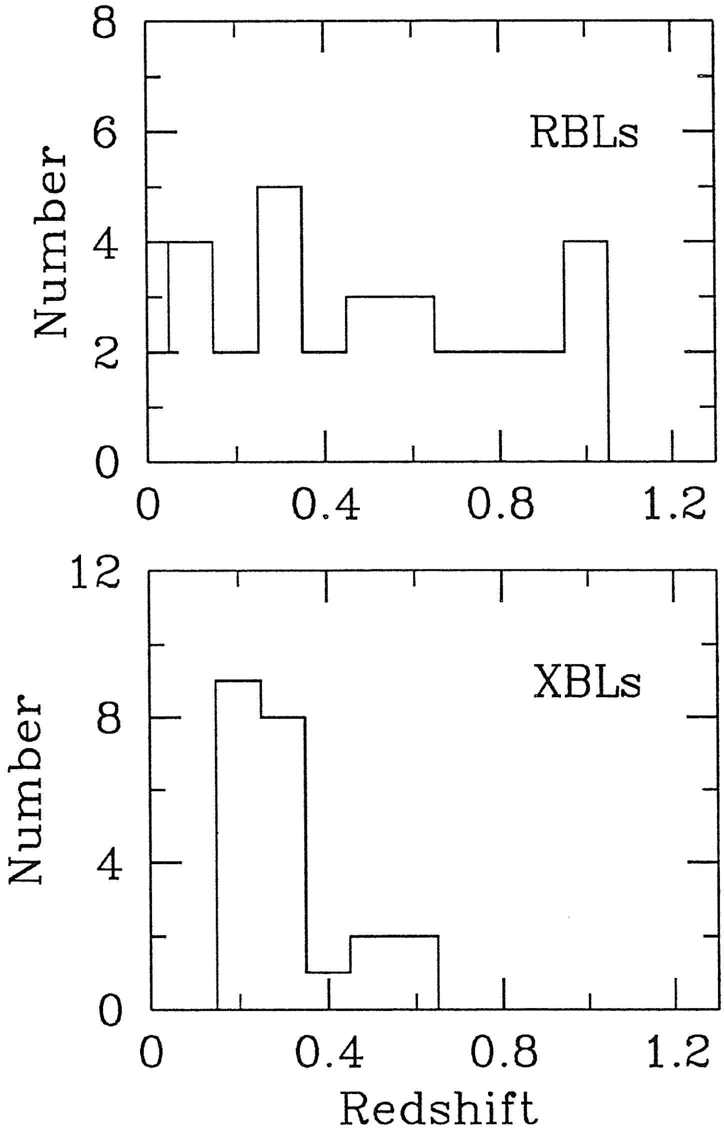

Figure 2.1: Redshift distributions of the 1 Jy radio-selected BL Lacs (top panel) and the X-ray selected BL Lacs from the *Einstein* Extended Medium Sensitivity Survey (bottom panel). RBLs span a large range from zero to 1, with average redshift z $\sim$ 0.56. XBLs are clustered between 0.2 and 0.6, with average z $\sim$ 0.3.

at all wavelengths than XBLs, although with some overlap between the two classes, and concluded that the radio-selected objects are affected by higher beaming than the X-ray selected ones. The same conclusion was reached by Perlman & Stocke (1993) and Laurent-Muehlesein et al. (1993), comparing the radio morphologies of the two classes. As discussed above (Introduction), similar conclusions were previously obtained for incomplete samples by Ledden & O'Dell (1985), Stocke et al. (1985), Maraschi et al. (1986).

A continuity of properties between the two samples was later noted by Gear (1993) in a study of the IR (JHK) colors of a subset of RBLs and XBLs. He showed that both samples form a single population with a luminosity dependent shape (the higher the IR luminosity, the steeper the slope of the IR continuum). He argued that this is probably due to an increasing contribution of the non-thermal emission for higher redshift RBLs with respect to the more nearby XBLs.

Padovani (1992a) compared the 1 Jy RBLs to a sample of flat spectrum radio sources, including HPQs and LPQs, and showed that RBLs are on average less luminous at all observed frequencies from radio to X-rays.

Padovani (1992a,b) found that the distribution of the extended (unbeamed) radio luminosities of RBLs do not differ from that of FRI radio galaxies, contrary to Flat Spectrum Radio Quasars (FSRQs) which are as luminous as FRII. This led to the conclusion that RBLs and FSRQs are different populations with no connection, *"examples of similar relativistic phenomena in radio galaxies of different powers"* (Padovani 1992a). This conclusion was strengthened by Gabuzda et al. (1989, 1992), who, from VLBI radio maps, found that RBLs have different polarization morphologies than quasars. Their evidence ruled out any connection between BL Lacs and FSRQs as a class, e.g. the hypothesis of gravitational lensing (although this is *not* ruled out for *single* objects).

Another conclusion of Padovani (1992a,b), based on the similarity of extended radio emission for RBLs and FRI galaxies, is that RBLs would form a unique population, without distinction between the low-redshift ($z \lesssim 0.3$), "BL Lac type" and the high-redshift, "quasar-like" sources, a distinction postulated by Burbidge & Hewitt (1987). However, from radio maps at 5 GHz taken with the VLA for 13 RBLs of the 1 Jy sample, Kollgaard et al. (1992) found that 8 objects had morphology and polarization consistent with FRII galaxies. All these sources are at $z \gtrsim 0.3$. Stickel et al., comparing the distributions of the line luminosities available for RBLs with those of distant quasars, found a dichotomy between distant and nearby RBLs. The latter are clearly less luminous than quasars in their line emission; on the contrary, for the more distant RBLs the line luminosity distribution has a substantial overlap with that of quasars.

In summary, the average properties of the 1 Jy RBLs have been the subjects of several recent studies. The principal conclusion is that RBLs have intermediate properties between XBLs and HPQ/OVVs concerning redshift distributions and continuum/line luminosity. However, it is not clear at this point to what extent the three classes of Blazars are distinct populations, or are manifestations of a single, intrinsic phenomenon with continuous properties. To this regard it is worth mentioning the "unification" scheme for RBLs and FSRQs proposed by Maraschi & Rovetti (1994). These authors show that there exists a continuity of properties of the *beamed* emission between these two classes. They would thus differ only in the strength of the emission lines and in the radio morphology, which in the authors' suggestion would depend *"on the global power and/or on the ambient medium surrounding the central engine"*.

2.1.3 OTHER BLAZAR SAMPLES USED IN THIS WORK

The properties of the 1 Jy RBLs will be compared in the following to those of other Blazars. Beside the EMSS XBLs, a group of XBLs and FSRQs, for which Rosat data are published, will be considered.

The group of XBLs comprises 8 BL Lacs from the HEAO-1 Large Area Sky Survey (LASS). The LASS catalog consists of 842 sources detected in the energy range 0.8 – 20 keV, with a flux limit of 250 nJy at 5 keV (Wood et al. 1984). At present, about 75% of the sources detected have been identified (Remillard et al. 1990), in particular the BL Lacs recognized so far number 29 in total. They have been classified on the basis of a featureless optical continuum, variability and/or polarization of the optical or radio counterpart, and compact radio emission. Eight of them, appearing in the preliminary list of Schwartz et al. (1989), were detected during the Rosat All-Sky Survey (RASS) with enough counts to allow spectral statistics. The Rosat data were analyzed by Brinkmann & Siebert (1994). These objects will be referred to in the following as the "LASS XBLs". Clearly, the sample is not complete nor statistical. However, the LASS XBLs form a group of bright objects selected at harder energies than the EMSS XBLs, therefore making a comparison of the energy distributions in the Rosat range interesting.

A sample of 8 FSRQs is also used in the analysis. These quasars are a subset of a complete sample of flat spectrum radio sources, selected at 1.4 and 5 GHz with the requirement $\alpha_r < 0.5$ ($S_\nu \sim \nu^{-\alpha_r}$), in the region of the sky north of $\delta = 70°$ and at galactic latitudes $> 10°$. Beside the 8 quasars, the complete sample of flat spectrum radio sources also includes 5 BL Lacs, all appearing in the 1 Jy sample (0454+844, 0716+714, 1749+701, 1803+784, 2007+777). Rosat observations of this sample have been published by Brunner et al. (1994). We have added 5 FSRQs from the Pearson-Readhead sample (Pearson & Readhead 1988), whose Rosat data are available from the archive, in order to increase the number of quasars. These objects are listed in Appendix 1. Although not complete, the 13 quasars form a reasonably sized group of quasar-like Blazars for which spectral information in the Rosat range are available.

2.2 Rosat Observations of the 1 Jy RBLs

Because of the recent definition of the two samples, systematic comparisons of the RBL and XBL behavior in X-rays were not possible, until the launch of the Rosat satellite in 1990. This offered the unique opportunity to study the two samples in the same energy range in a uniform way. Several observation proposals were successfully submitted to observe in pointed mode most of the RBLs of the 1 Jy sample (Feigelson et al. 1993; Urry et al. 1993a), while several single sources were already observed by various PIs in other runs. The Colorado group lead the program of observations of the EMSS XBLs (Stocke et al. 1993).

In total, 31 out of the 34 RBLs of the 1 Jy sample were observed in pointed mode by the Rosat PSPC. Data are presently available for 29 sources (proprietary and from the public archive). These objects are listed in column 1 of Table 2.1 with their redshifts (column 2), taken from Stickel et al. (1991), unless otherwise noted. Listed in column 3 are the values of the absorption due to cold gas in the Galaxy (column density N_H, in cm^{-2}) in the direction of the target. The Galactic absorption was taken from the EINLINE database, which interpolates the value from the 21 cm map of the Galaxy (Stark et al. 1992), or, whenever possible, from Elvis et al. (1987). In the first case the uncertainties are of the order of 1 $\times 10^{20}$ cm^{-2}, while the Elvis et al. measurements are more accurate ($\pm 1 \times 10^{19}$ cm^{-2}). The latter values are indicated in the Table.

The log of the Rosat observations is given in columns 4-6, which list the date of the observation, the exposure time, and the total source count rate. Three objects (0851+202, 1749+096, and 2005-489) were observed twice. Effective exposures are listed in the Table, that is, exposures corrected for the time intervals of variable or anomalous background. The total counts of the source were extracted, as described below, in the energy range 0.15 – 2.0 keV.

Three sources, 0716+714, 1652+398, and 2005-489, were observed in long exposures and in a bright state ($\gtrsim$ 15,000 photons). In one case (1514-241=AP Lib) there was no detection. For five other sources (0454+844, 0814+425, 0820+225, 0828+493, and 2254+074) less than 100 counts were observed. In subsequent observations, more counts were found for this source (Brunner et al. 1994). For a few sources the Rosat data have been already published by other authors; references are quoted in column 7.

Eighteen sources in Table 2.1 were also detected during the RASS. In column 8 we list the corresponding count rates, obtained from the automatic search performed by NASA. For several objects, substantial variability is inferred comparing the intensities in the RASS and in the pointed observation. We searched also for the objects for which pointed Rosat observations were not performed. The only object detected is 1807+698 = 3C 371 at a count rate 0.206 ± 0.023. Enough counts were found to allow spectral analysis (Fink et al. 1992).

Several objects of Table 2.1 were previously observed with the *Einstein* IPC experiment. The comparison with these previous observations is the subject of a later Section (see Chapter 4).

Table 2.1: Rosat Observations of the 1 Jy RBLs

Source	z	Galactic N_H ($\times 10^{20}$ cm^{-2})	Pointed Mode Date of Obs.	Pointed Mode Exposure (s)	Pointed Mode Count Rate (cts s^{-1})	Refs. ^{a}	RASS C. Rate ^{b} (cts s^{-1})
0048-097	···	3.52	93 Jul 4	8363	0.377 ± 0.007	···	0.244 ± 0.027
0118-272	> 0.557	1.53	93 Jul 10	2635	0.130 ± 0.008	···	0.086 ± 0.029
0426-380	> 1.030	1.94	93 Aug 2	4048	0.042 ± 0.004	···	0.075 ± 0.023
0454+844	0.112 ^{c}	6.31	91 Apr 4	3358	0.008 ± 0.005	1	···
0537-441	0.896	4.0	91 Apr 10	2598	0.343 ± 0.011	2	0.189 ± 0.028
0716+714	> 0.3 ^{d}	3.7	91 Mar 8	18143	0.841 ± 0.007	1,3	0.144 ± 0.023
0735+178	> 0.424	4.54	92 Oct 28	6684	0.080 ± 0.004	···	0.115 ± 0.019
0814+425	0.258?	4.92	92 Oct 6	6120	0.012 ± 0.002	···	···
0820+225	0.951	4.20	92 Oct 29	3728	0.016 ± 0.002	···	···
0828+493	0.548	3.94	92 Oct 3	4821	0.013 ± 0.002	···	···
0851+202	0.306	2.75	91 Apr 16	3202	0.251 ± 0.009	···	···
			91 Nov 10	6785	0.561 ± 0.009	···	
0954+658	0.367	4.28	91 Apr 17	6772	0.048 ± 0.003	···	0.044 ± 0.012
1144-379	1.048	8.67	93 Jul 7	7747	0.108 ± 0.004	···	···
1147+245	···	2.03	93 May 27	10942	0.016 ± 0.002	···	···
1308+326	0.997	1.08	91 Jun 8	7824	0.081 ± 0.004	···	0.060 ± 0.012
1514-241	0.049	8.80	93 Aug 17	2915	< 0.008 ^{e}	···	0.053 ± 0.013
1519-273	···	8.90	93 Aug 17	2552	0.100 ± 0.007	···	0.032 ± 0.010
1538+149	0.605	3.23	93 Jan 28	7215	0.034 ± 0.002	···	0.083 ± 0.025
1652+398	0.033	1.73	91 Feb 25	7281	5.850 ± 0.028	···	4.666 ± 0.108
1749+096	0.320	9.61	91 Mar 17	3963	0.065 ± 0.005	···	···
			92 Mar 28	4944	0.063 ± 0.004	···	
1749+701	0.770	4.01	92 Nov 9	3702	0.085 ± 0.005	1	0.083 ± 0.013
1803+784	0.684	4.02	92 Jul-Dec	5602	0.102 ± 0.005	1	0.062 ± 0.013
1823+568	0.664	4.20	92 Jun 19	5900	0.133 ± 0.005	···	0.105 ± 0.013
2005-489	0.071	4.60	92 Apr 27	9787	3.017 ± 0.018	···	2.610 ± 0.093
			92 Oct-Nov	11462	1.656 ± 0.012	···	
2007+777	0.342	8.90	91 Dec 11	4116	0.032 ± 0.003	1	0.034 ± 0.009
2131-021	0.557?	4.24	93 Nov 2	6746	0.016 ± 0.002	···	···
2200+420	0.069	20.15	92 Dec 22	2067	0.159 ± 0.009	···	0.089 ± 0.015
2240-260	0.774	1.46	93 Nov 9	3356	0.049 ± 0.005	···	···
2254+074	0.190	5.39	93 Nov-Dec	1753	0.028 ± 0.005	···	···

Notes to Table 2.1: (a) References to previously published data; (b) Courtesy of NASA; (c) Ref. [1]; (d) Wagner et al. (1993); (e) 3σ upper limit.

References: [1] = Brunner et al. (1994); [2] = Treves et al. (1993); [3] = Cappi et al. (1994).

2.3 The Rosat PSPC

The Rosat scientific payload consists of a large X-ray telescope (XRT), operative in the range 6 – 100 Å, and a coaligned smaller Wide Field Camera (60 – 300 Å). The XRT comprises the mirror assembly (XMA), two position sensitive proportional counters (PSPC), and a high resolution imager (HRI). For the full description of the XRT and WFC characteristics we refer to Trümper (1984), while here we will focus mainly on the PSPC. The "Rosat PSPC Calibration Guide" (October 93 draft) was also used.

a) General characteristics of the PSPC

Two multiwire proportional counters (PSPC-B and PSPC-C) were mounted in the focal plane of the XRT, together with two spare ones (PSPC-A and PSPC-D), which were mainly used for the ground-calibrations. PSPC-C, which was primarily designed for the mission, was accidentally destroyed on Jan 1991. The PSPC-B detector was used thereafter. The gas counter is a mixture of different gases, principally argon (Table 2.2). An X-ray photon penetrates into the detector passing through a thin entrance window, and is photo-electrically absorbed by the counter gas, producing a photo-electron. This primary electron ionizes the gas atoms forming a secondary electron cloud, whose number of electrons is approximately proportional to the energy deposited by the incident photon. Other processes, like, for example, the Auger effect, can contribute to the cloud, which drifts to the anode and produces a charge signal (with an induced signal at the cathode).

The amplitude of the signal on the cathode grids is used to determine

Table 2.2: Rosat PSPC Characteristics

Field of view	2° (diameter)
Spatial Resolution	300 μm ($\sim$ 25 arcsec) at 0.93 keV
Entrance window	1 μm thick, polypropylene
Coating window	Carbon 50 μg cm^{-2} Lexan 40 μg cm^{-2}
Support grid transmission	$\sim$ 72% (average value)
Gas mixture	65% Argon 15% Methane 20% Xenon
Energy Resolution	$\frac{\Delta E}{E} = 0.43(\frac{E}{0.93})^{-0.5}$ FWHM

the position of an event in the PSPC. When the signal has a small pulse-height amplitude the position of the event is incorrectly determined. The effect is particularly relevant for very soft photons (energies $\lesssim$ 0.15 keV), which appear scattered in the image producing a blur around the source. It is known as the "ghost image" problem.

The entrance window of the PSPC is a thin foil of polypropylene coated with carbon (50 μg cm^{-2}) and lexan (40 μg cm^{-2}), in order to decrease the UV transmission. The window structure support consists of a rigid circle (28 mm diameter) with 8 equispaced radial struts. Below this rib structure there are two mesh systems; a coarse mesh of 100 μm tungsten wires spaced every 2 mm, and a fine mesh of 25 μm wires with 0.4 mm spacing. Both rib and meshes are completely opaque to X-rays. The net average transmission of the window is $\sim$ 72%.

This transmission rate can, however, be significantly decreased depending on how much of the area of the X-ray beam from a celestial pointlike source is occulted by the mesh wires. The probability that a pointlike source is hidden underneath the meshes is greatest near the center of the field of view, while for large off-axis angles only vignetting effects are relevant. To prevent the shadowing, the spacecraft is slowly (± 3 arcmin every 400 s) moved back and forth along a direction diagonal to the mesh grids ("wobble").

The PSPC gain describes the amplification of the primary electrons, that is, the relationship between the energy of the incident photon and the produced pulse-height. It is a function of the cathode/anode potential difference and on the gas density. However, there are spatial and temporal variations of the gain. Among the latter, there has been a drop of 30% of the gain on Oct 14th 1991, and small, not yet well quantified fluctuations within the orbits. It has been discovered that for sources of high signal to noise the PSPC gain saturates (there is a fall-off in the signal amplification). This "rate-gain" effect affected the data of Mrk 421, which was used to create the 93jan12 matrix (see below).

The principal characteristics of the PSPC are recapitulated in Table 2.2. It is worth noting that the spatial and the energy resolutions of the PSPC, 25 arcsec and 43% FWHM at 1 keV, respectively, represent two of the major improvements of this instrument with respect to the *Einstein* Imaging Proportional Counter, the previous mission sensitive in a soft energy range (0.3 – 3.5 keV).

b) The PSPC Spectral Response

(The following is a summary from "The Rosat PSPC Calibration Guide", by T.J. Turner and I.M. George, Oct 93 draft)

The detector response matrix contains all the current knowledge of the instrument, namely, the characteristics of the entrance window and of the counter gas, the details of the effective areas of the mirror, and the resolution properties. Its exact calibration is of crucial importance for a proper interpretation and modelling of the spectra, but one of the principal difficulties is that there is no a source with an exactly known spectrum in 0.1 – 2.0 keV. The calibration of the matrix was performed using the spectra of SNR N132D and of a few other brigth sources.

Two spectral responses are currently available for the analysis of the Rosat data, the 92mar11 and 93jan12 matrices. The main problem concerning the 92mar11 matrix is its poor calibration around the Carbon edge, which appeared in terms of large residuals between 0.3 – 0.4 keV, with a maximum deficit of 4.5% at 0.4 keV. Other systematic features were a sharp rise of the data above 2 keV, and a deficit of photons below 0.2 keV. The Jan 93 matrix was created by combining the Mar 92 one with the spectrum of an ideally featureless source, Mrk 421. Simultaneous measurements of Rosat and Ginga showed that the 0.2 – 10 keV spectrum of this object is well fitted by a broken power law model. This model was used to fit the Rosat spectrum alone and to derive the factor "Model/Data", which was used to create the Jan 93 matrix. Every element of the new matrix was created by multiplying the elements of the Mar 92 matrix by "Model/Data".

It was later discovered that the data of Mrk 421 were affected by the rate-gain effect, which is still not yet calibrated. However, the 93jan12 matrix is thought to be the best for data taken in "low-gain" mode (after 14 Oct 1991), while for "high-gain" mode (before Oct 1991) data the 92mar11 matrix is recommended.

An independent problem is given by the temporal gain variations (see above), which can create spurious spectral features. An example will be discussed later for the bright source 2005–489 (Chapter 3). In order not to overestimate narrow spectral features, it is recommended to add a systematic 2% error in quadrature to the data, in particular for the higher signal-to-noise spectra.

2.4 Analysis of the Rosat Data

The PSPC Rosat images were analyzed within the IRAF package using PROS v.2.3. The source counts, spectrum, and light curve were extracted in a circle centered on the target. The radius of the circle was chosen so as to include a large ($\gtrsim 90\%$) fraction of the point spread function at 1 keV. For faint sources, with 100 counts or less, this yielded a radius of $\sim$ 1.5 arcmin, while for the brightest sources, radii up to $\sim$ 3.5 arcmin were obtained. These are large enough to collect all the soft photons and avoid the "ghost-image" problem (see above). The background was in general evaluated in an annulus around the source, with and inner radius 2.0 – 4.0 arcmin, depending on the source region size, and outer radius 10–15 arcmin. Other sources falling into the background region were excised.

Before extracting the final products, the background light curves were carefully examined to check for flares or anomalous trends. In all these cases, the data were time-filtered excluding the intervals of variable background. The strongest variations generally occured at the beginning of the Good Time Intervals (GTIs), where the instrument is turned on to observe the designated target. Because one single observation can consist of several GTIs, in a number of sources up to a few hundreds of seconds were excluded from the analysis.

Figure 2.2 shows, as an example, the field of 2005–489 (April observation). The blur of the source is due to the "ghost" effects. The same image in detector coordinates is shown in Figure 2.3, where the elongation of the source measures the extent of the wobble of the instrument.

2.4.1 TIMING ANALYSIS

We searched for time variability of each source applying the standard methods of the Kolmogorov-Smirnov (KS) and the χ^2 tests. Both compare the observed data points, or (for the KS test), the cumulated distribution function, to a constant and calculates the deviation of the data from it. The maximum deviation can be compared to tabulated values, which are related to different levels of significance for a given number of datapoints, to decide whether significant variability is present. A practical difference between the two methods is that, contrary to the χ^2 test, the KS does not require to rebin the data, and is thus in principle more sensitive to single, shorter flares.

To avoid the effects of the wobble, which can introduce spurious variability, for the χ^2 test the light curves were rebinned in bins longer than the wobble period, > 400 s. No variability was detected with both tests in the light curves accumulated on the entire exposure and on the single GTIs.

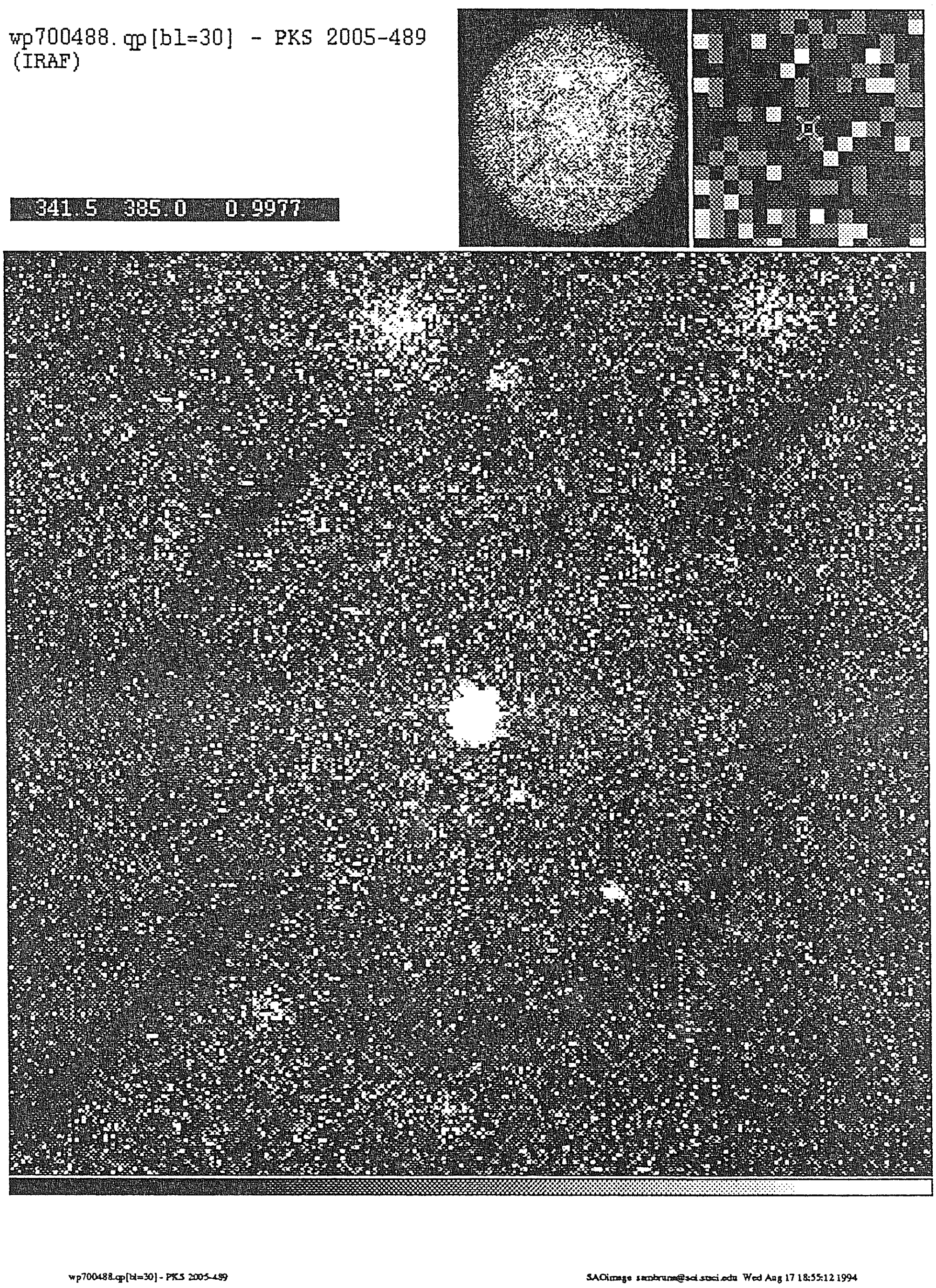

Figure 2.2: The Rosat PSPC image of the bright RBL 2005–489. The support structure of the entrance window is clearly visible. The diameter of the central part of the window is ~ 2°. The source appears blurred because of the "ghost-image" problem (see text). Two sources are present ~ 13 and 32 arcmin away from the target (to the bottom right), whose closest known optical counterparts are two stars of spectral type F8V and K0III, respectively.

The only object for which significant ($> 99\%$) variability was found is 0716+714. As previously reported (Cappi et al. 1994), the Rosat light curve of this object decreases by a factor 7 in two days. A flare is also present, with an increase of the intensity of $\sim 70\%$ in less than ~ 3 hrs. 0716+714 is also known for its rapid radio variability (Quirrenbach et al. 1989).

2.4.2 SPECTRAL ANALYSIS

Source spectra were extracted on the full 256 channel range for all the sources with a signal at $\gtrsim 6\sigma$ in Table 2.1 (27 sources), and rebinned into 34 bins following the SASS (Standard Analysis Processing System) automatic binning scheme. Bins below 3 and bin 34 were discarded from the analysis, because the spectral response is poorly known at these energies. In order to accommodate the requirement of Gaussian errors on the spectral parameters, for the fainter sources the bins in the range 4-33 were further rebinned in such a way that at least 10 photons were present in each new bin. In the case of the bright objects 0716+714, 1652+398, and 2005–489, because of the high number of counts, we rebinned the 256 channel spectrum by hand getting a higher number of bins. We verified that the same results were obtained as in the case of the automatic rebinning.

In all cases, the spectral fitting was performed in the energy range 0.15 – 2.0 keV. Different response matrices were used depending on the date of acquisition of the data (see Section 2.3). For data taken in "high-gain" mode (before 14 Oct 1991), the 92mar11 matrix was used, while the 93jan12 response was adopted for data taken in "low-gain".

The spectra were converted into PHA format using PROSCON v.2.3.

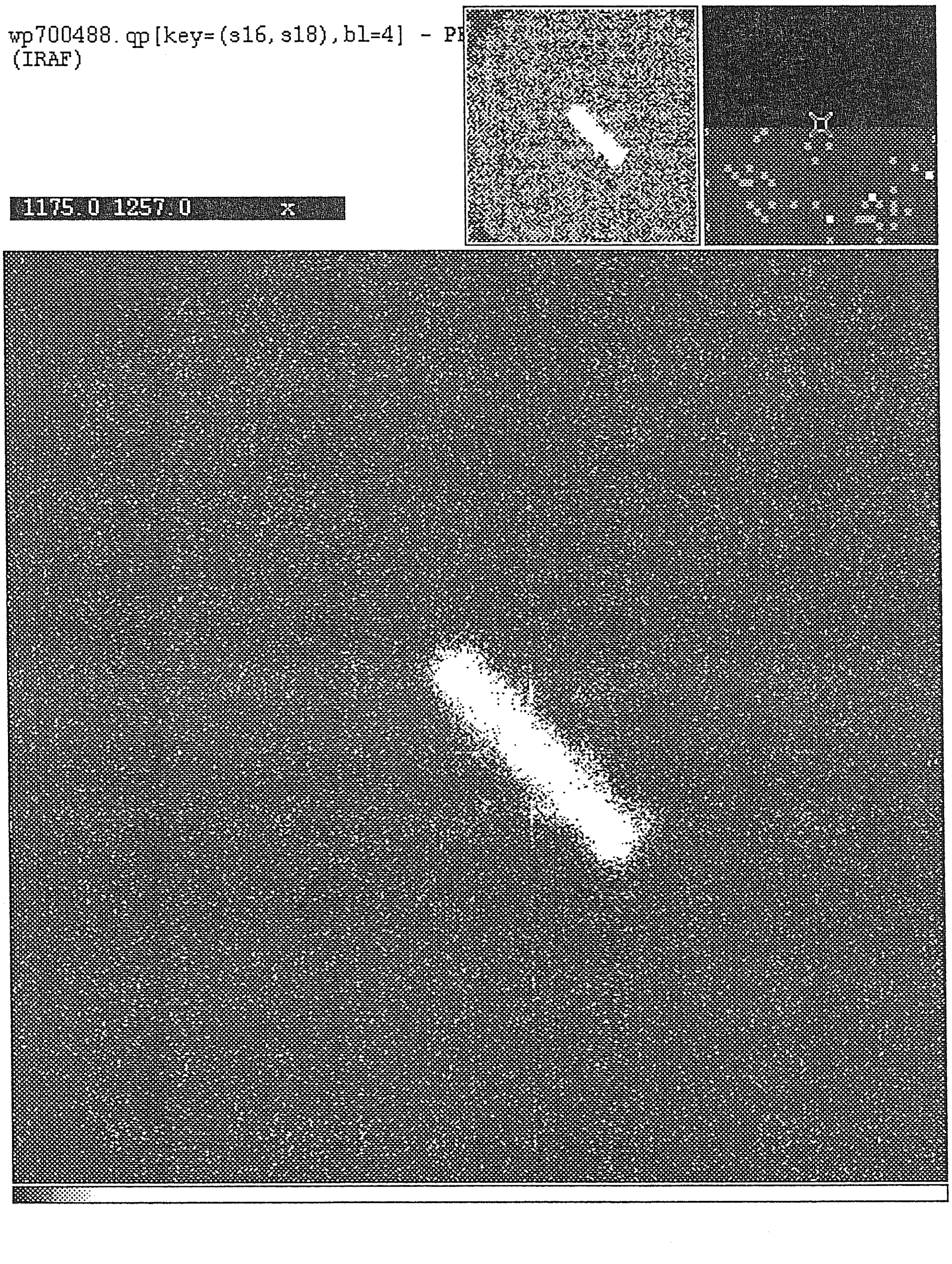

Figure 2.3: The same as in Figure 2.2, but in detector coordinates. The elongated structure of the source is due to the wobble of the satellite, a movement along one axis in order to prevent occultation of point-like sources under the wire mesh (which is just visible in this image).

The spectral fitting was performed within XSPEC (Shafer et al. 1990). A series of spectral models were folded with the instrumental responses and compared to the data, determining the spectral parameters with the common χ^2 minimization technique. The errors on the parameters were determined by adding tabulated quantities to the minimum χ^2 (Lampton et al. 1978), corresponding to given confidence levels. Errors quoted here represent the 90% confidence level.

As a first, simple approximation the data were fitted with a single power law model (model a), modified at the low energies by absorption by cold gas in the Galaxy:

$$\frac{\mathrm{dN}}{\mathrm{dE}} = \mathrm{N} \times \exp(-\mathrm{N_H}\sigma(\mathrm{E})) \times \mathrm{E}^{-\Gamma}, \tag{2.1}$$

where N is the normalization, N_H the absorbing column density of neutral hydrogen (in cm^{-2}), with other elements fixed at solar abundances, and Γ the photon spectral index. The cross section $\sigma(\mathrm{E})$, which includes the opacities of elements with normal abundances, is from Morrison & McCammon (1983). Two kinds of fits were performed with the power law model, one with N_H fixed at the Galactic value (model a1), and one with N_H allowed to vary (model a2).

In a few cases evidence was derived for a more complex spectrum, with a possible second spectral component emerging below or above a given energy. A broken power law model (model b), of the form

$$\frac{dN}{dE} = N \times \begin{cases} exp(-N_H\sigma(E)) \times E^{-\Gamma_1} & \text{if E} < \mathrm{E_0} \\ exp(-N_H\sigma(E)) \times E_0^{\Gamma_2-\Gamma_1} \times E^{-\Gamma_2} & \text{if E} > \mathrm{E_0}, \end{cases} \tag{2.2}$$

was used in these cases, where Γ_1 and Γ_2 are the photon indices below and above the break energy $\mathrm{E_0}$, respectively.

A single power law with the inclusion of an absorption edge at a given energy E_L was also used. The edge is modelled in the following way:

$$\frac{dN}{dE} = \begin{cases} 1 & \text{if } E < E_L \\ exp(-\tau_L(\frac{E}{E_L})^{-3}) & \text{if } E > E_L, \end{cases} \tag{2.3}$$

where τ_L is the absorption depth. This model was combined to the single absorbed power law to give model c.

The χ^2 probability, P_{χ^2}, was used to determine the acceptance confidence of a spectral fit. The statistical significance of the more complex models was determined from the reduction in χ^2 using the F-test (Bevington 1969), assuming for significance the standard threshold at $P_F = 95\%$.

CHAPTER III

Spectral Fitting of the Rosat Data

3.1 Fits to the Rosat spectra

3.1.1 SINGLE POWER LAW

For the objects with more than 100 photons in Table 2.1, the Rosat spectra were fitted with a single power law model with N_H fixed to the Galactic value (model a1) and free (model a2). For 0814+425, 0820+225, 0828+493, and 2254+074, for which less than 100 counts were detected, the absorption was kept fixed at the Galactic value. The results of the fitting procedure are reported in Table 3.1, where the photon index Γ and the reduced χ^2 per degrees of freedom (χ^2_r/dofs) for model a1 are listed in columns 2 and 3. Columns 5, 6, and 7 give the fitted N_H and Γ, and χ^2_r/dofs for model a2. The acceptance probabilities for the two models, P_{χ^2}, are reported in columns 4 and 8. The flux densities at 1 keV (from model a1) are reported in column 9. The errors quoted in the Table are at 90% confidence level for two interesting parameters ($\Delta\chi^2 = 4.6$).

From the χ^2 values reported in the Table it is apparent that the single power law (both models a1 and a2) gives, in general, an acceptable description of the Rosat spectra of the 1 Jy RBLs. The error contours for Γ and N_H are illustrated in Figure 3.1, where 68%, 90%, and 99% confidence levels are reported. The vertical lines mark the value of the Galactic column density in each source, and the associated uncertainty. This is in general $\pm 1 \times 10^{20}$ cm^{-2} for the Stark et al. (1992) measurements (Table 2.1), while the values from Elvis et al. (1987) are more accurate ($\pm 0.1 \times 10^{20}$ cm^{-2}).

Two remarkable cases are the bright sources 1652+398 and 2005-489. The fits with a single power law (model a1) to the Rosat spectra of these two sources are clearly unacceptable ($P_{\chi^2} < 10^{-9}$). The residuals of model a1 in individual sigma (i.e., Data-Model/Measurement Error) are shown in Figures 3.2a for 1652+398 and 3.3a-b for 2005–489.

In the residuals of 1652+398 a systematic deficit of photons below $\sim$ 0.25 keV is present, with a significance of $\sim 4\sigma$. The fit with free absorption is acceptable, yielding a value of N_H higher than the Galactic one (Figure 3.1a-x), and a slope steeper than when the absorption is fixed (Table 3.1). This indicates a possible downward curvature of the spectrum.

In 2005-489, the fitted absorption is lower than the Galactic N_H in the case of the Oct-Nov observation, while for the high state of April the evidence is marginal (Figure 3.1t). In both states, the slope obtained with free N_H is flatter than that obtained with N_H fixed to the Galactic value (Table 3.1), which is *per se* related to an excess of soft photons. However, a significant (4σ) photon deficit centered at 0.45 keV, which seems broader in the case of the November observation, is present in the residuals of 2005–489 (Figure 3.3a-b). We show below (Section 3.2) that this feature is likely to be related to the PSPC gain changes.

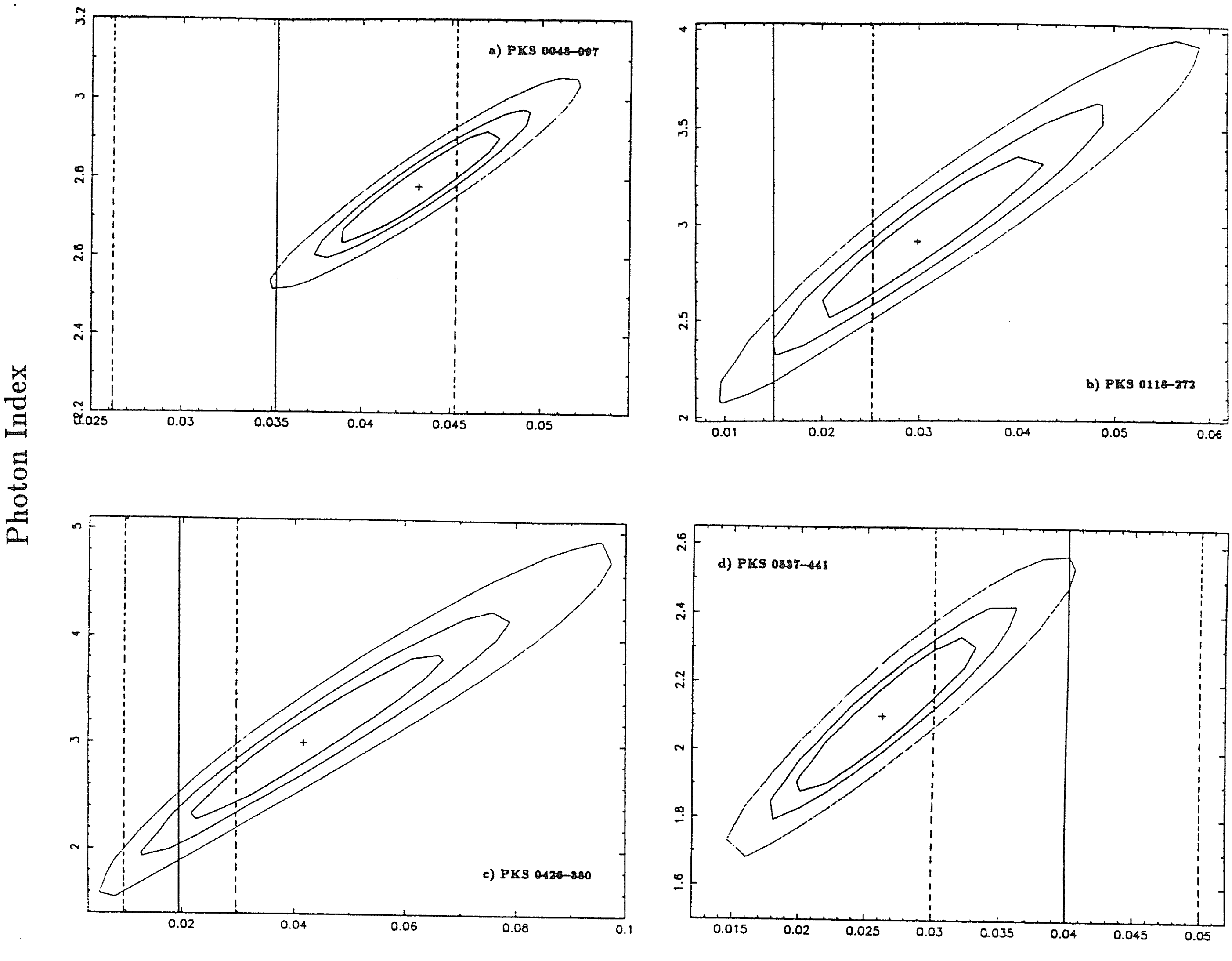

Figure 3.1: (a-x) The χ^2 confidence contours for each power law fit to the Rosat spectra of the RBLs. The abscissa is the absorption column density in 10^{22} cm^{-2}, the ordinate is the photon index. The best fit is marked with a cross; 68%, 90%, and 99% confidence levels are plotted. The vertical lines mark the values of the Galactic absorption (solid line) and its confidence range (dashed lines). The uncertainty is $\pm 1 \times 10^{20}$ cm^{-2} for the measurements from Stark et al. (1992) and $\pm 0.1 \times 10^{20}$ cm^{-2} for those from Elvis et al. (1987).

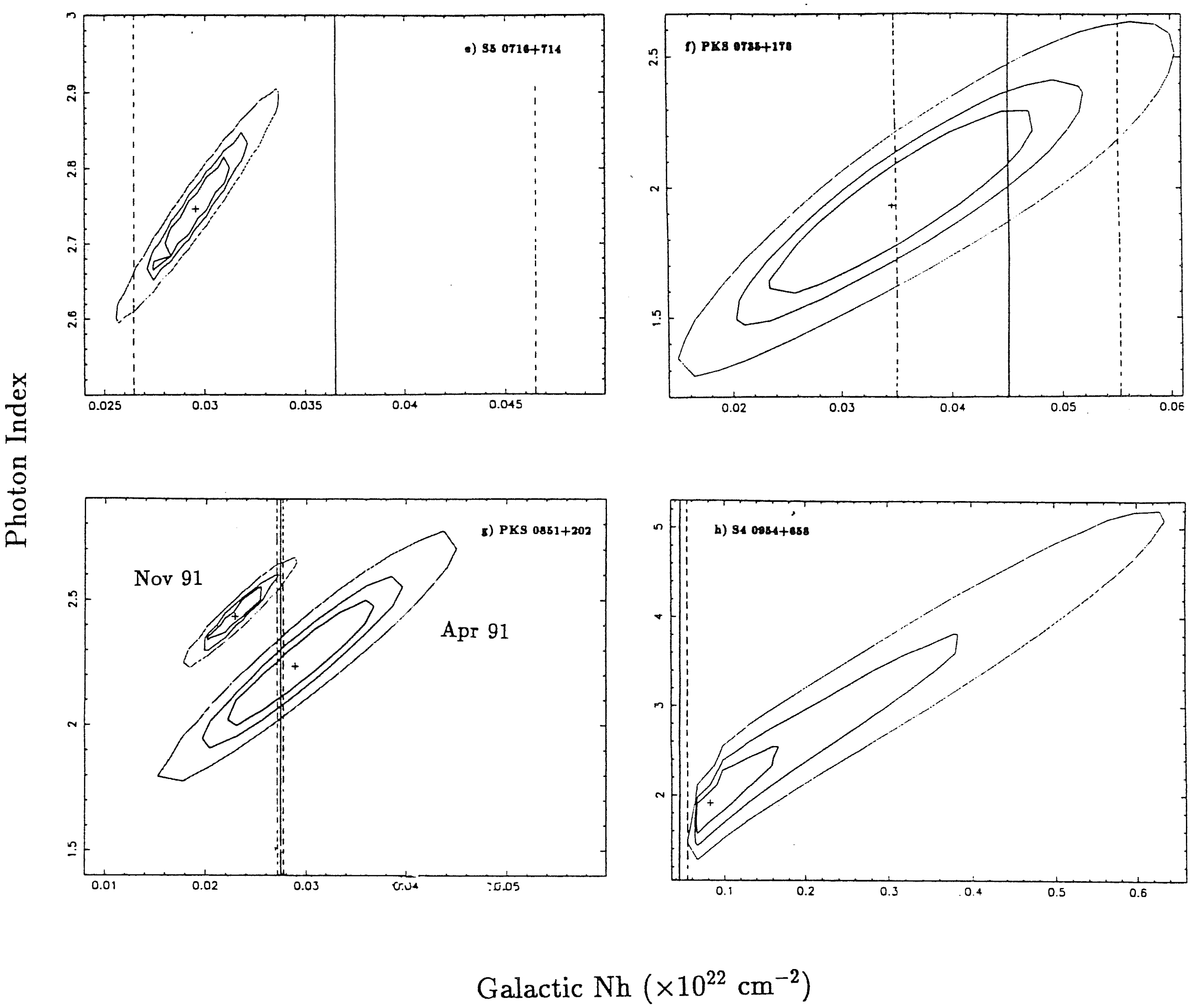
e) S5 0716+714
f) PKS 0735+178
g) PKS 0851+202
h) S4 0954+658
Nov 91
Apr 91
Photon Index
Galactic Nh (×10^22 cm^-2)
2.6
2.7
2.8
2.9
3
0.025
0.03
0.035
0.04
0.045
1.5
2
2.5
0.02
0.03
0.04
0.05
0.06
1.5
2
2.5
0.01
0.02
0.03
0.04
0.05
2
3
4
5
0.1
0.2
0.3
0.4
0.5
0.6

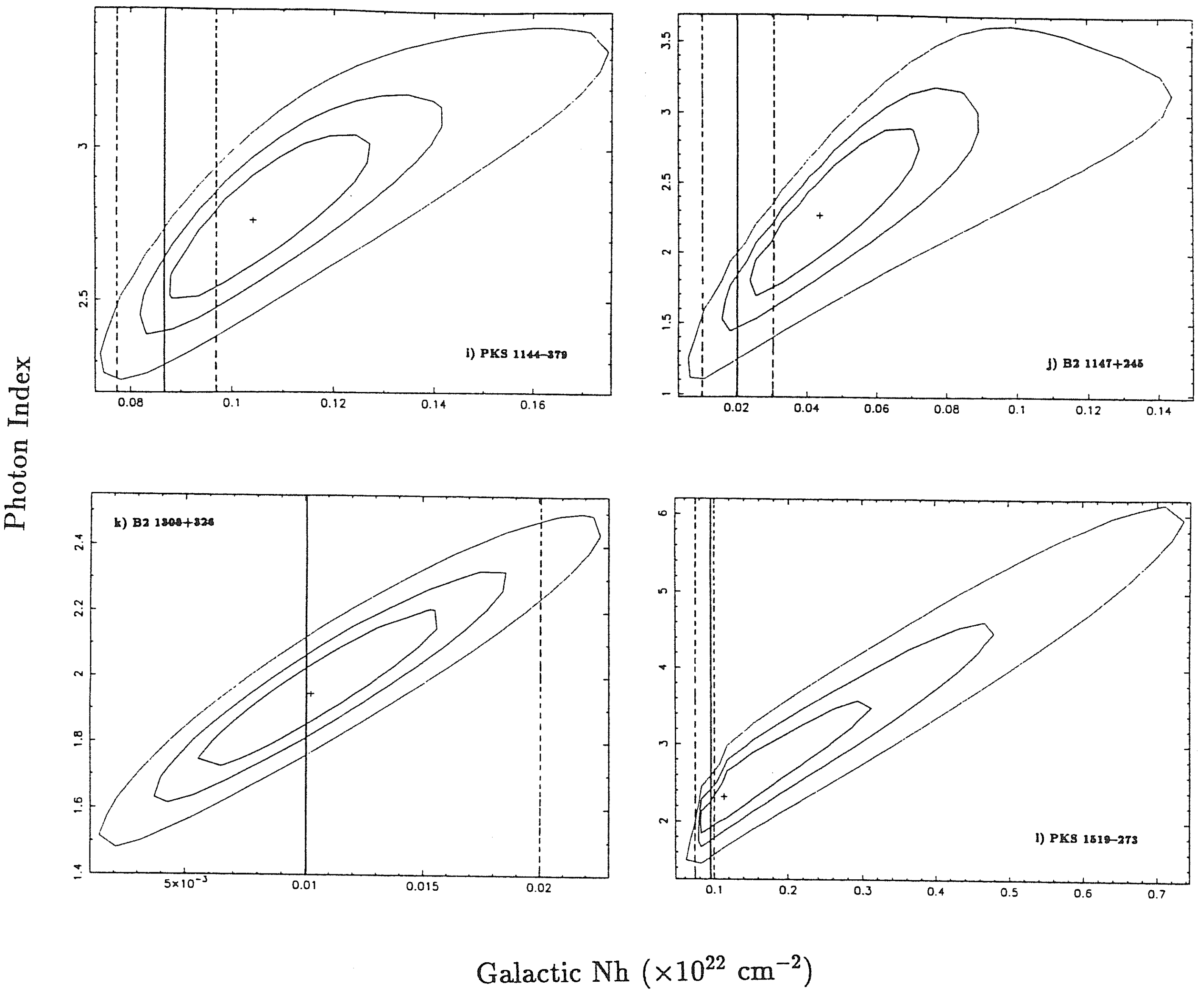
Photon Index
i) PKS 1144−379
2.5
3
0.08
0.1
0.12
0.14
0.16
j) B2 1147+245
1
1.5
2
2.5
3
3.5
0.02
0.04
0.06
0.08
0.1
0.12
0.14
k) B2 1308+326
1.4
1.6
1.8
2
2.2
2.4
5×10⁻³
0.01
0.015
0.02
l) PKS 1519−273
2
3
4
5
6
0.1
0.2
0.3
0.4
0.5
0.6
0.7
Galactic Nh (×10²² cm⁻²)

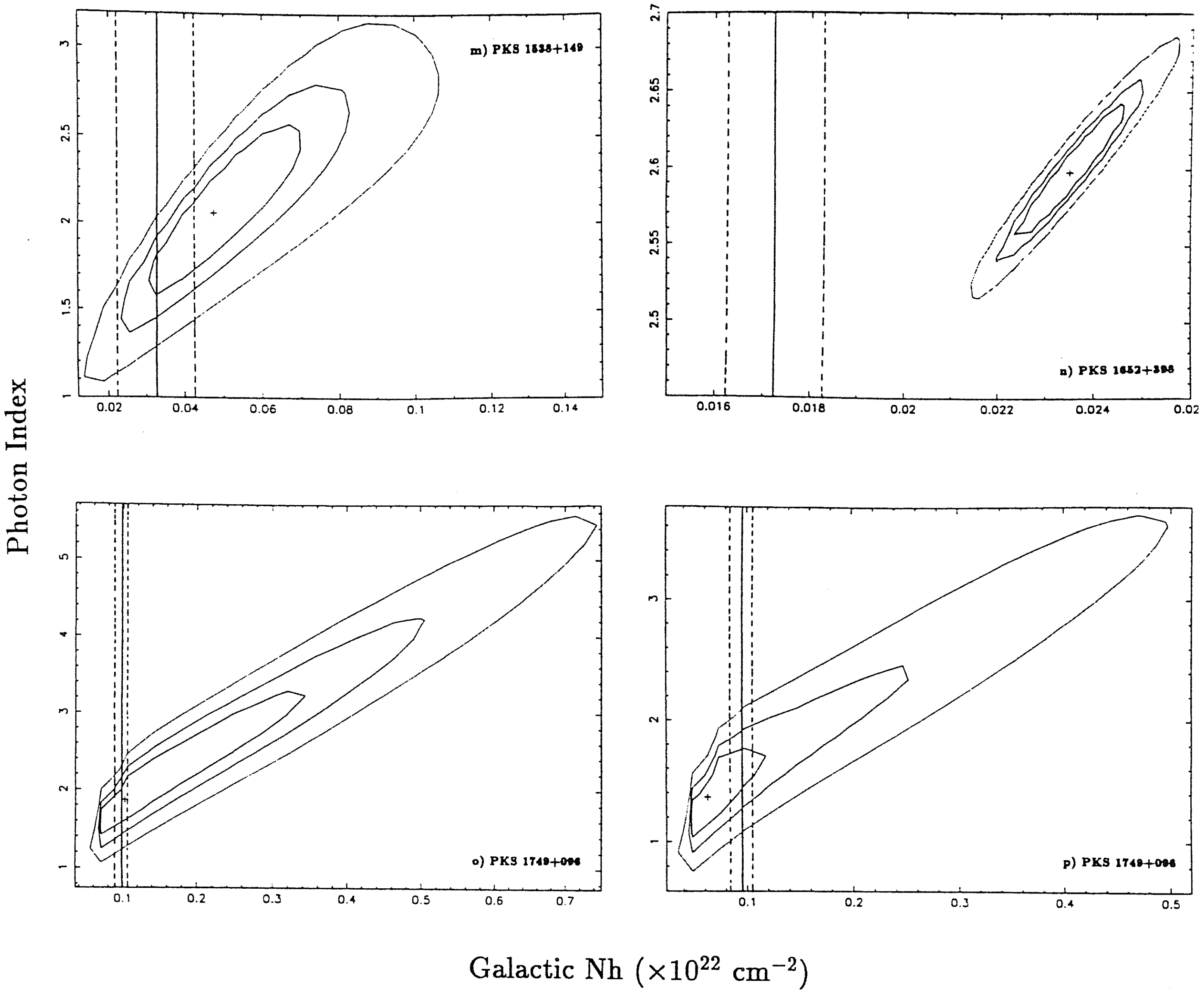
Photon Index
m) PKS 1538+149
1
1.5
2
2.5
3
0.02
0.04
0.06
0.08
0.1
0.12
0.14
n) PKS 1652+398
2.5
2.55
2.6
2.65
2.7
0.016
0.018
0.02
0.022
0.024
0.02
o) PKS 1749+096
1
2
3
4
5
0.1
0.2
0.3
0.4
0.5
0.6
0.7
p) PKS 1749+096
1
2
3
0.1
0.2
0.3
0.4
0.5
Galactic Nh ($\times 10^{22}$ cm^{-2})

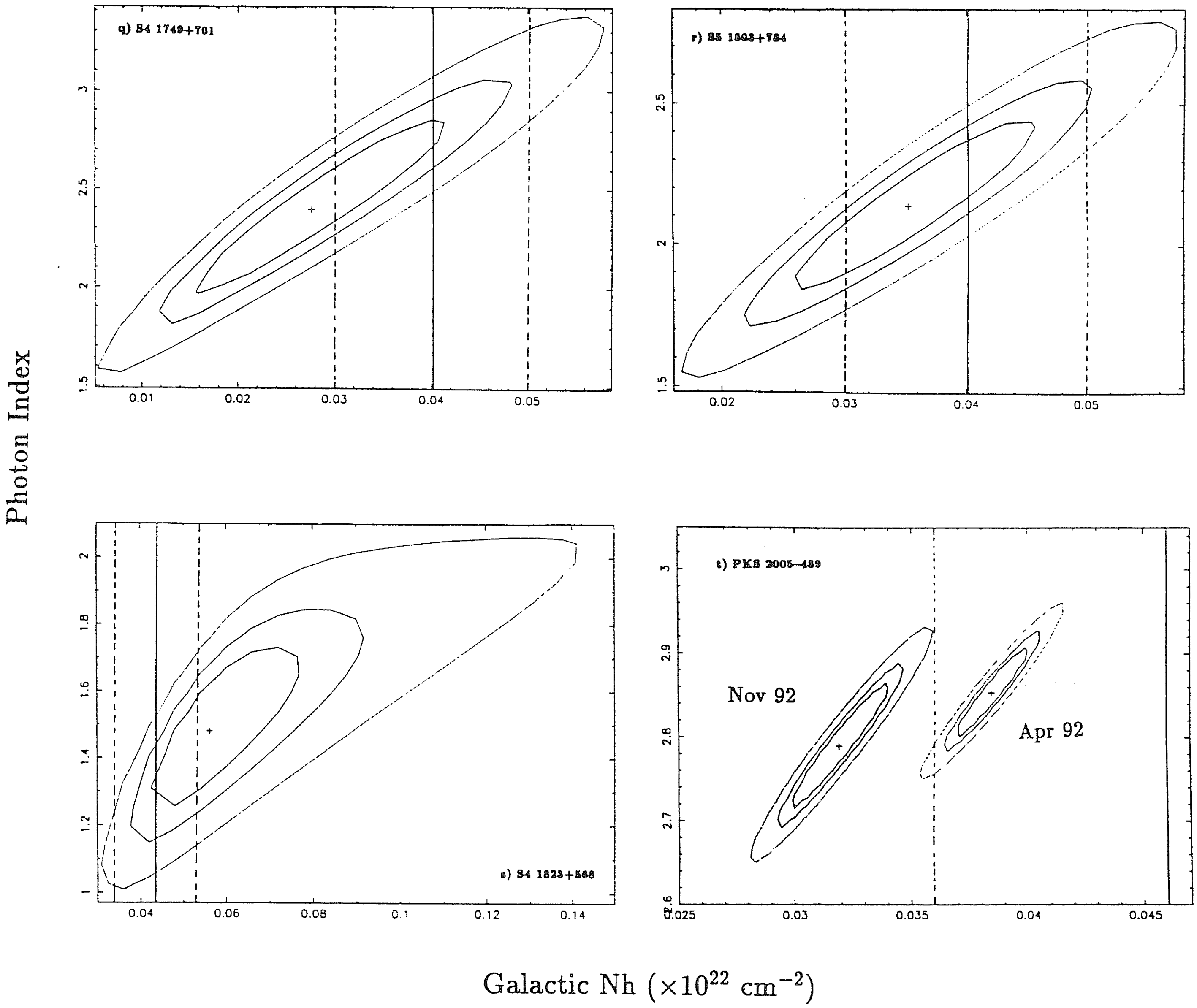
q) S4 1749+701
r) S5 1803+784
s) S4 1823+568
t) PKS 2005−489
Nov 92
Apr 92
Photon Index
Galactic Nh ($\times 10^{22}$ cm^{-2})
1.5
2
2.5
3
0.01
0.02
0.03
0.04
0.05
1
1.2
1.4
1.6
1.8
0.06
0.08
0.1
0.12
0.14
2.6
2.7
2.8
2.9
0.025
0.035
0.045

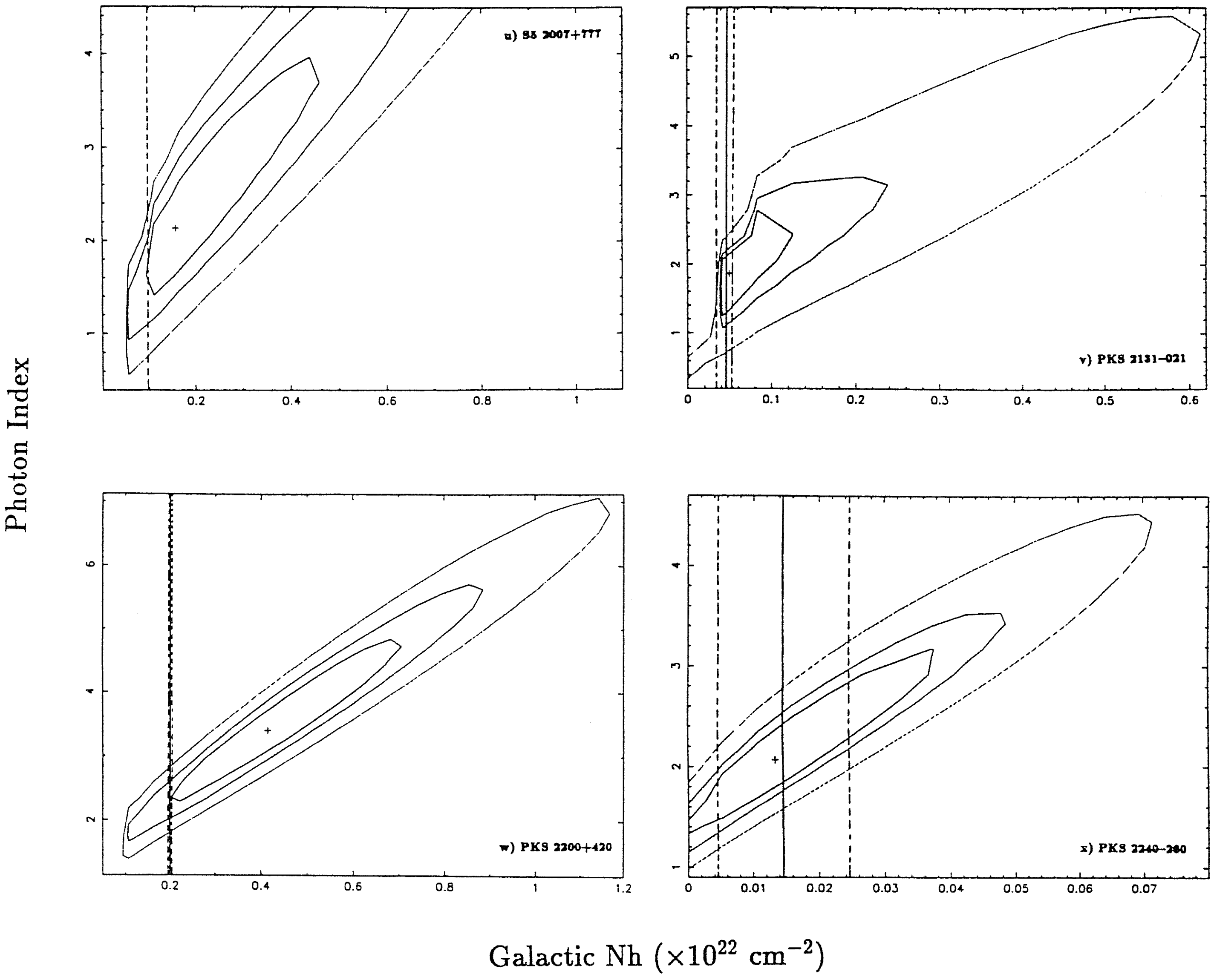
Photon Index
u) S5 2007+777
v) PKS 2131-021
w) PKS 2200+420
x) PKS 2240-260
Galactic Nh ($\times 10^{22}$ cm^{-2})
1
2
3
4
5
6
0
0.01
0.02
0.03
0.04
0.05
0.06
0.07
0.1
0.2
0.3
0.4
0.5
0.6
0.8
1
1.2

From the contour plots in Figure 3.1, marginal evidence for a column density "lower" than Galactic is present also in the spectrum of 0716+714. In this case too, the slope from the fit with model a2 is flatter than that from model a1. This indicates a possible soft-excess.

For the remaining objects the fits with model a2 yield column densities consistent with the Galactic values and slopes in good agreement with those derived with model a1. We thus conclude that, with a few exceptions, the single power law with N_H fixed to the Galactic value is a good description of the Rosat spectra of the 1 Jy RBLs.

Table 3.1: 1 Jy RBLs
Fits to the Rosat spectra with the single power law

	N_H fixed (Gal. value)			N_H free				
Object (1)	Γ (2)	χ^2_r/d.o.f. (3)	P_{χ^2} (%) (4)	N_H [a] (5)	Γ (6)	χ^2_r/d.o.f. (7)	P_{χ^2} (%) (8)	Flux_{1keV} [b] (9)
0048-097	2.53 ± 0.06	0.86/26	66.9	$4.32^{+0.63}_{-1.61}$	2.78 ± 0.20	0.56/25	96	0.84 ± 0.05
0118-272	$2.36^{+0.18}_{-0.16}$	0.77/17	73	$2.98^{+1.99}_{-1.56}$	$2.91^{+0.72}_{-0.62}$	0.58/16	90.1	0.19 ± 0.03
0426-380	2.20 ± 0.27	1.70/12	6.0	$4.16^{+3.85}_{-2.96}$	$3.00^{+1.31}_{-1.12}$	1.64/11	8.0	0.08 ± 0.02
0537-441	2.53 ± 0.16	2.05/25	0.15	$2.61^{+0.34}_{-0.88}$	$2.10^{+0.34}_{-0.32}$	1.78/24	1.08	0.75 ± 0.08
0716+714	2.97 ± 0.03	1.30/35	11.02	$2.95^{+0.31}_{-0.29}$	2.75 ± 0.11	0.74/34	86.4	1.20 ± 0.04
0735+178	$2.20^{+0.23}_{-0.25}$	1.44/24	7.5	$3.45^{+1.76}_{-1.99}$	$1.93^{+0.49}_{-0.47}$	1.42/23	8.72	0.22 ± 0.03
0814+425	$-1.22^{+1.01}_{-1.41}$	5.34/5	0.007	...	...	...	...	$0.04^{+0.01}_{-0.00}$
0820+225	$2.17^{+0.49}_{-0.71}$	1.22/4	30	...	...	...	...	0.050 ± 0.02
0828+493	$2.09^{+0.76}_{-0.97}$	0.97/3	40.6	...	...	...	...	$0.04^{+0.03}_{-0.02}$
0851+202 [c]	2.15 ± 0.12	1.58/24	3.5	$2.94^{+1.16}_{-1.00}$	$2.21^{+0.38}_{-0.35}$	1.64/23	2.73	0.96 ± 0.05
[d]	2.60 ± 0.06	1.05/27	39.3	$2.28^{+0.46}_{-0.42}$	2.44 ± 0.17	0.90/26	61	0.58 ± 0.06
0954+658	$1.34^{+0.24}_{-0.27}$	0.98/15	47.3	$8.21^{+31.40}_{-3.59}$	$1.91^{+1.93}_{-0.57}$	0.63/14	84.2	0.23 ± 0.02
1144-379	$2.52^{+0.18}_{-0.19}$	1.33/24	12.9	$10.40^{+3.79}_{-2.27}$	$2.76^{+0.42}_{-0.38}$	1.29/23	16	0.41 ± 0.03
1147+245	$1.67^{+0.29}_{-0.35}$	0.77/13	69.3	$4.33^{+4.62}_{-2.98}$	$2.26^{+0.94}_{-0.85}$	0.62/12	82.7	0.05 ± 0.009
1308+326	1.97 ± 0.13	0.99/24	47.5	$1.02^{+0.85}_{-0.67}$	$1.95^{+0.38}_{-0.35}$	1.03/23	42.11	0.14 ± 0.02

Table 3.1: *(continued)*

	N_H fixed (Gal. value)			N_H free				
Object (1)	Γ (2)	χ^2_r/d.o.f. (3)	P_{χ^2} (%) (4)	N_H [a] (5)	Γ (6)	χ^2_r/d.o.f. (7)	P_{χ^2} (%) (8)	Flux_{1keV} [b] (9)
1519-273	$2.08^{+0.37}_{-0.42}$	0.86/14	60.3	$11.32^{+37.49}_{-5.12}$	$2.33^{+2.34}_{-0.74}$	0.88/13	57.4	0.43 ± 0.06
1538+149	$1.68^{+0.27}_{-0.30}$	0.98/16	47.6	$4.75^{+3.74}_{-2.60}$	$2.05^{+0.76}_{-0.71}$	0.96/15	49.5	0.10 ± 0.02
1652+398	2.36 ± 0.01	3.43/33	$< 10^{-9}$	2.35 ± 0.16	2.60 ± 0.06	1.24/34	16	8.43 ± 0.13
1749+096 [e]	$1.82^{+0.39}_{-0.42}$	0.68/17	82.6	$10.31^{+40.64}_{-5.27}$	$1.87^{+2.40}_{-0.68}$	0.72/16	77.6	0.34 ± 0.04
[f]	1.61 ± 0.40	0.46/18	97.4	$6.27^{+20.09}_{-2.97}$	$1.37^{+1.13}_{-0.51}$	0.41/17	98.4	0.30 ± 0.04
1749+701	$2.78^{+0.23}_{-0.23}$	0.76/19	75.7	$2.76^{+2.09}_{-1.68}$	$2.40^{+0.68}_{-0.62}$	0.71/18	80.4	0.16 ± 0.03
1803+784	$2.28^{+0.16}_{-0.18}$	1.20/25	22.4	$3.52^{+1.54}_{-0.45}$	$2.14^{+0.46}_{-0.45}$	1.23/24	20.11	0.26 ± 0.03
1823+568	$1.28^{+0.17}_{-0.19}$	1.09/22	34.8	$5.62^{+3.56}_{-1.93}$	$1.48^{+0.37}_{-0.34}$	1.04/21	40.8	0.47 ± 0.04
2005-489 [g]	3.09 ± 0.03	3.77/35	$< 10^{-9}$	3.84 ± 0.23	2.85 ± 0.08	2.40/34	0.001	5.00 ± 0.10
[h]	3.26 ± 0.03	4.26/35	$< 10^{-9}$	$3.18^{+0.29}_{-0.27}$	2.79 ± 0.10	1.40/34	6.08	2.67 ± 0.08
2007+777	$1.63^{+0.55}_{-0.65}$	0.55/10	85.5	$16.52^{+53.95}_{-0.10}$	$2.19^{+3.12}_{-1.32}$	0.53/9	85.4	0.15 ± 0.03
2131-021	$1.73^{+0.48}_{-0.68}$	0.93/7	48.2	$4.94^{+19.06}_{-0.10}$	$1.86^{+1.43}_{-1.11}$	1.07/6	37.8	0.05 ± 0.01
2200+420	$2.32^{+0.40}_{-0.41}$	0.97/16	48.7	$42.00^{+47.00}_{-34.00}$	$3.10^{+2.67}_{-1.55}$	0.92/15	54.1	0.89 ± 0.11
2240-260	$2.18^{+0.34}_{-0.41}$	0.37/11	96.8	1.31 (< 5.78)	$2.07^{+1.89}_{-0.99}$	0.4/10	94.7	0.07 ± 0.03
2254+074	$2.58^{+1.03}_{-1.90}$	0.36/2	69.8	…	…	…	…	0.09 ± 0.07

Notes to Table 3.1: a=Absorbing column density, in 10^{20} cm^{-2}; b=Monochromatic flux density, in μJy; c=Observation of 16 Apr 91; d=Observation of 10 Nov 91; e=Observation of 17 Mar 91; f=Observation of 28 Mar 92; g=Observation of 27 Apr 92; h=Observation of Oct-Nov 92.

3.1.2 OBJECTS WITH REPEATED OBSERVATIONS

Previous studies of BL Lacs showed that spectral variability in X-rays is a characteristic of these objects (Urry et al. 1986; Treves et al. 1989; Giommi et al. 1990; Sambruna et al. 1994a). The observed trend is a flattening of the spectrum in the brighter state.

Three objects of the sample (0851+202, 1749+096, and 2005-489) were observed twice by Rosat in pointed mode. Only 0851+202 and 2005-489 were found in two different intensity states, while 1749+096 did not change in X-ray brightness. No variations of the slopes can be detected in 0851+202, as is apparent comparing the corresponding contour plots (Figures 3.1g). In the contour plots of 2005-489 a variable absorption is rather seen. However, as it will be clear from the discussion below, this change is likely to be an effect of the instrumental gain shifts.

A peculiar behavior is shown by 0716+714, whose long exposure allowed a detailed study of the light curve (Cappi et al. 1994). The previous authors found a highly variable emission, with a dimming of a factor ~ 7 in two days, accompanied by spectral variations. When the source is in the brighter state, the spectrum is well described by a single power law model. A flatter component emerges in the spectrum when the intensity decreases. Its extrapolation to the γ-ray energies is in good agreement with the slope of the spectrum measured by EGRET (Kurfess 1994).

Three sources of the present sample (1652+398, 1749+701, and 2005–489) were also detected during the RASS with a statistics high enough to allow a spectral analysis (Brinkmann & Siebert 1994). 1652+398 was brighter in the survey than in the pointed observation by a factor ≈ 2.6; no spectral variability is inferred comparing the slope in Table 3.1 with that reported by Brinkmann & Siebert (2.27 ± 0.05, for fixed N_H). 1749+701 was detected in a brightness state comparable to that studied here, with a similar spectrum. The RASS observation of 2005–489 corresponds to a state intermediate between the two pointed observations, with a steeper slope than either observations ($\Gamma = 3.62 \pm 0.10$).

In summary, although the flux can change considerably, no spectral variability has been detected for the repeatedly observed objects.

3.1.3 MORE COMPLEX FITS

a) Broken power law model

As discussed above, the Rosat spectra of the 1 Jy RBLs are well described by a single power law with Galactic absorption (model a1), except in a few cases, where evidence for more complex spectra is found.

The results obtained for 1652+398 indicate a flattening of the spectrum at the low energies (convexity). On the contrary, for 0716+714 and 2005–489, a softer component (concave spectrum) is suggested.

For these objects we performed fits with a broken power law model (model b; see Chapter 2). In all cases a significant improvement with respect to the single power law (model a1) was obtained with model b. The spectral parameters are reported in Table 3.2. Comments on the single objects are given below.

b) The Oxygen Edge

Table 3.2: Broken Power Law Fits

Object	Broken Power Law ^{a}				P_{χ^2}	P_F^b
	Γ_1	Γ_2	E(keV)	χ^2_r/d.o.f.		
0716+714	$3.20^{+1.16}_{-0.09}$	$2.74^{+0.13}_{-0.57}$	$0.500^{+0.640}_{-0.220}$	0.70/33	0.92	> 0.999
1652+398	$2.00^{+0.01}_{-0.60}$	$2.60^{+0.15}_{-0.08}$	$0.427^{+0.367}_{-0.121}$	1.10/33	0.31	> 0.999
2005-489 ^{c}	$6.03^{+3.97}_{-1.06}$	$2.93^{+0.07}_{-0.06}$	$0.260^{+0.018}_{-0.012}$	1.73/33	0.006	> 0.999
^{d}	$8.20^{+1.80}_{-2.65}$	2.98 ± 0.09	$0.255^{+0.039}_{-0.010}$	1.06/33	0.38	> 0.999

Notes to Table 3.2:

a = N_H fixed to the Galactic value
b = F-test performed with respect to a single power law + Galactic N_H
c = April 92 observation
d = November 92 observation

There is some evidence that in the X-ray spectra of some bright BL Lacs an absorption edge at an observed energy of ~ 0.6 keV is present. The first evidence came from the Objective Grating Spectrometer spectrum of PKS 2155-304, where a large (~ 100 eV) absorption edge at ~ 650 eV was observed (Canizares & Kruper 1984). This was interpreted as a Lyman-α Oxygen VIII resonance absorption trough at a rest frame energy of 654 eV. An edge around ~ 0.5 keV was also observed in the BBXRT and ASCA spectra of this object (Madejski et al. 1994; Tashiro et al. 1994), and postulated in the spectra of other BL Lacs observed with lower sensitivity instruments (Urry et al. 1986; Madejski et al. 1991). Besides the edge at 0.5 keV, two other absorption features at 0.7 and 0.9 keV were observed in the ASCA data of PKS 0548–322 (Tashiro et al. 1994).

The poor resolution of the PSPC, and the residual systematic uncertainties in the response matrices do not allow the study of discrete absorption in the Rosat data. However, assuming that the Oxygen edge at 0.654 keV is an ubiquitous feature for the whole class (e.g., Madejski et al. 1991), we can derive upper limits for its strength from the Rosat spectra, by fitting the data with a single power law + edge with fixed energy (for the objects with a determination of the redshift; Table 2.1).

Table 3.3 reports the results of these fits. The data were fitted with an absorbed power law + edge model, fixing N_H to the Galactic value and the energy of the edge to 0.654/(1+z) keV. The errors quoted in Table 3.3 for the optical depth are at 90% confidence for 2 interesting parameters. It can be seen that in most cases the fitted τ is small ($\lesssim$ 1.0). In one case (1308+326) it is significantly large (> 1.0); however, the χ^2 is not significantly improved with respect to the fit with the single power law model.

c) Comments on single objects

- **0716+714:** The fit with a broken power law model to the Rosat spectrum of 0716+714 is significantly improved with respect to the single power law model, yielding a concave continuum with a flattening of $\Delta\Gamma \sim 0.5$ above 0.5 keV (Table 3.2). The fitted slopes are consistent with the values given by Cappi et al. (1994).
- **1652+398:** The broken power law model yields a fit significantly improved with respect to the fit with the single power law model ($P_F > 99.9\%$). A convex spectrum, with a steepening of $\Delta\Gamma \sim 0.6$ above 0.43 keV is indicated. The residuals of the broken power law model are shown in Figure 3.2b. This model was also preferred to represent the 0.1 – 10 keV EXOSAT spectrum of 1652+398

Table 3.3: **Absorption Edge Information** [a]

Source	z	Energy (keV)	Optical Depth	Notes
0118–272	0.557	0.420	0.0 (< 0.76)	b
0426–380	1.030	0.322	0.0 (< 2.63)	b
0537–441	0.896	0.345	$1.89^{+1.68}_{-1.36}$	...
0716+714	0.300	0.503	$0.38^{+0.19}_{-0.18}$	b
0735+178	0.424	0.459	$0.50^{+1.20}_{-0.01}$	b
0851+202	0.306	0.500	0.0 (< 0.45)	c
...	...	...	$0.33^{+0.33}_{-0.29}$	d
0954+658	0.367	0.478	0.0 (< 0.70)	...
1144–379	1.048	0.319	0.0 (< 1.68)	...
1308+326	0.997	0.327	$2.09^{+3.31}_{-0.02}$	...
1538+149	0.605	0.407	$0.01^{+2.28}_{-0.008}$	...
1652+398	0.033	0.633	0.0 (< 0.02)	...
1749+096	0.320	0.496	$1.04^{+1.36}_{-0.01}$	e
1749+701	0.770	0.369	$1.07^{+2.52}_{-0.01}$	...
1803+784	0.684	0.388	$0.30^{+1.34}_{-0.01}$	...
1823+568	0.664	0.393	$0.17^{+1.27}_{-0.10}$	...
2005–489	0.071	0.611	0.04 (< 0.16)	f
...	...	...	0.32 ± 0.17	g
2007+777	0.342	0.487	0.0 (< 2.67)	...
2200+420	0.069	0.612	$0.86^{+1.39}_{-0.01}$	...
2240–260	0.774	0.369	$0.30^{+8.10}_{-0.01}$	...

Notes to Table 3.3:

- a: From fits with a power law + Galactic N_H + Edge model. The edge energy is fixed at a rest energy 0.654 keV. Errors on the optical depth are at 90% confidence
- b: The lower limit for the redshift is used
- c: April observation
- d: November observation
- e: Because of similar intensity, the Mar 91 and Mar 92 spectra were fitted together
- f: April observation
- g: Oct-Nov observation

(Sambruna et al. 1994a,b), yielding a convex spectrum with a steepening of 0.3 – 0.5 above 3 keV. Previous studies of this object with the *Einstein* data (Urry et al. 1986; Madejski et al. 1991) were consistent with the presence of the Oxygen absorption edge at $\sim$ 0.6 keV. In our pointed observation there is no evidence for this or other absorption features. A fit with a fixed edge energy (Table 3.3) yields an upper limit of 0.02 for the optical depth. Marginal evidence for such a feature (2σ significance), centered at $\sim$ 0.4 keV, was obtained from the RASS spectrum by Fink et al. (1991).

- **2005–489:** The broken power law model is highly preferred to the single power law model in both observations (Table 3.3). A concave spectrum is indicated. However, the break is found at $\sim$ 0.26 keV in both epochs, with a very steep low-energy photon index Γ_1 ($\sim$ 8.0). This "soft excess" seems strongly related to the presence of the prominent dip centered at 0.45 keV, the steep Γ_1 being determined by the three low-energy points in excess to the model in Figure 3.3. We show below that this dip is probably spurious, and that it may well be produced by gain changes. The only previous measurements of the X-ray continuum of 2005–489, obtained with the EXOSAT satellite in 0.1 – 10 keV, were consistent with the presence of low energy absorption, with τ around 3.0 (Sambruna et al. 1994a,b), although this instrument has no resolution below 1 keV. In the Rosat spectra, upper limits on τ of only 0.16 and 0.5 are derived for the Oxygen feature (Table 3.3).

3.2 The PSPC Gain Shifts: The Case of 2005–489

As mentioned above, a large dip centered at 0.45 keV is present in both Rosat spectra of the bright object 2005–489 (Figure 3.3). The strength of this

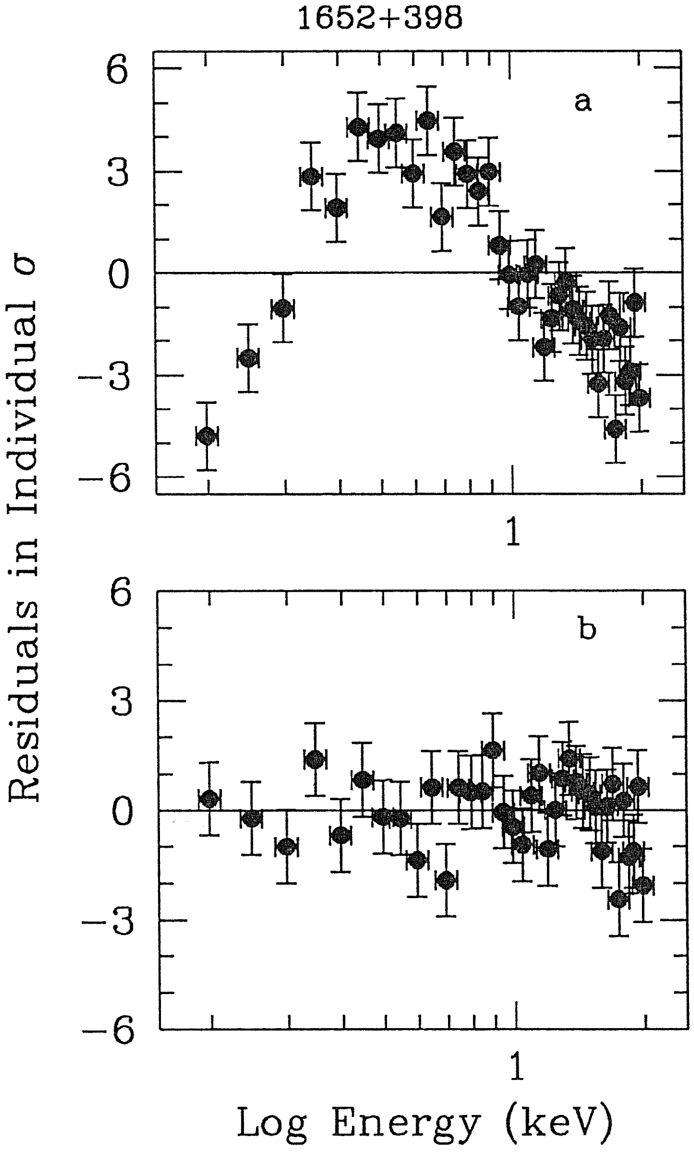

Figure 3.2: Residuals of the bright source 1652+398. *Panel a*: Residuals of the single power law + galactic absorption fit. A large deficit of counts, significant at $\sim 5\sigma$, is present below 0.5 keV. *Panel b*: Residuals from the fit with a broken power law model with Galactic absorption. The fit with the latter model is highly improved with respect to the fit with the single power law, and yields a convex spectrum.

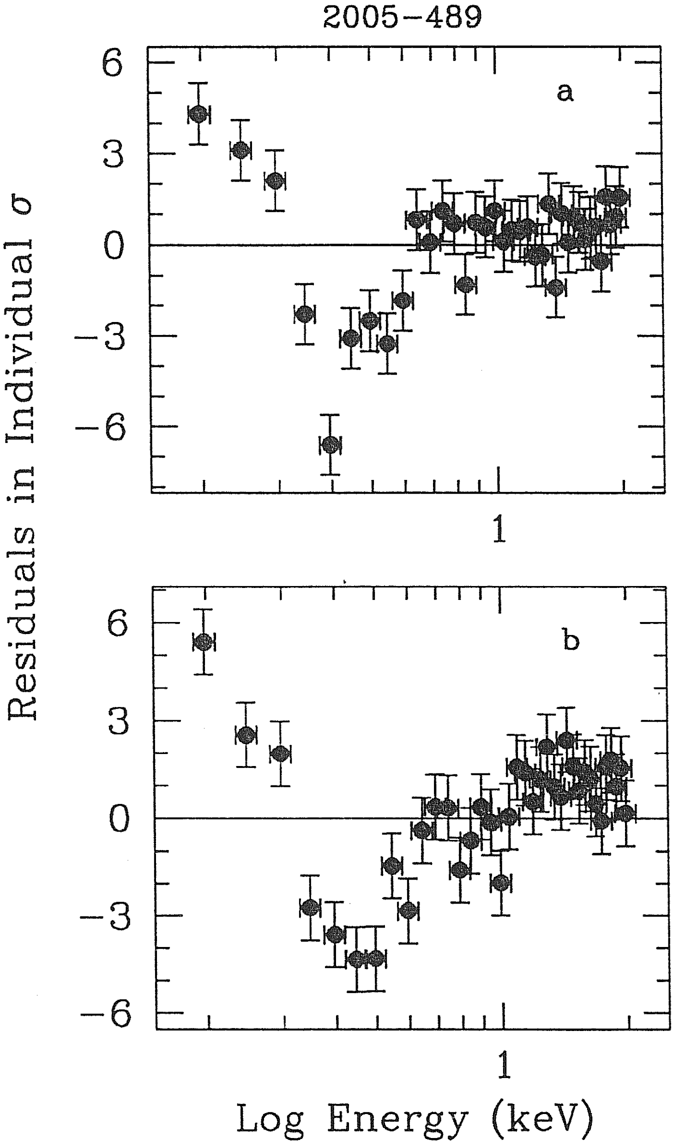

Figure 3.3: Residuals of the bright source 2005–489. *Panel a*: Residuals of the fit with the single power law + Galactic absorption model for the Apr 92 observation. *Panel b*: The same as panel (a) but for the Nov 92 observation. In both cases, a broad absorption feature at 0.4 – 0.5 keV is present, with a fitted optical depth $\tau \sim 2.0$ and 3.0, respectively.

"feature" seems higher than any known systematic uncertainty, being around $\sim 4\sigma$ in both cases. Fitting with a power law + edge, an optical depth τ of 2.0 – 3.0 is obtained in both cases (Table 3.4a); however, the edge energy is found at the Carbon edge energy, $\sim$ 0.27 keV, an element which constitute the entrance window of the detector.

It is known that the PSPC suffered gain variations, which are still under examination. A response matrix, properly taking into account these variations, is not yet available. The effect of the shifts is to assign systematically different channels to the incoming photons, with the net result that the whole spectrum is shifted forward or backward in the detector sensitivity range. This is expected to lead to the presence of localized zero or low-counts channels, which can show up as spurious "features".

Although we can not yet quantify the exact amount of the shift during the observations of 2005–489, we can mimic its effects in the observed spectrum. We can do this by artificially "shifting" the 256 channel spectra in the IRAF TABLE format. In practice it is sufficient to add one or more zero channels to the top (shift forward) or the bottom (shift backward) of the TABLE file.

We used this procedure on the observed spectra to check whether the shifts can modify the energy and the profile of an existing feature, and whether they can create one. In the following we will refer to tests performed for the Nov 92 observation; similar conclusions are drawn for the April 92 spectrum. We analyzed the spectra obtained by "shifting" the original spectrum forward by 1 to 6 channels, and backward by 1 to 4 channels. The resulting shifted spectra were rebinned and analyzed in the same way as the observed spectra.

We found that when the spectrum is shifted backward the feature becomes more and more prominent, with a larger and larger τ. When it is shifted

Table 3.4: 2005–489. Power Law + Edge Fits

	Parameters [a]			
	Γ	E_L (keV)	τ	χ^2_r/d.o.f.
a. Rosat Observations				
Apr 92	$3.21^{+0.12}_{-0.04}$	$0.271^{+0.004}_{-0.007}$	$2.040^{+0.891}_{-0.522}$	1.21/33
Nov 92	$3.36^{+0.12}_{-0.03}$	$0.273^{+0.05}_{-0.008}$	$3.00^{+1.04}_{-0.792}$	1.30/33
b. Shifted Spectrum (Nov 92)				
Forw. 2 ch.	3.20 ± 0.05	$0.469^{+0.051}_{-0.107}$	$0.672^{+0.438}_{-0.196}$	1.67/33
Forw. 6 ch.	3.02 ± 0.05	$0.594^{+0.032}_{-0.035}$	$0.852^{+0.212}_{-0.203}$	23.6/33
Backw. 2 ch.	$3.66^{+0.13}_{-0.10}$	0.252 ± 0.006	$4.907^{+1.470}_{-1.097}$	1.78/33
c. Simulated Spectrum (Nov 92)				
Forw. 2 ch.	3.15 ± 0.05	0.68 (> 0.35)	0.14 (< 0.33)	3.82/33
Forw. 6 ch.	2.93 ± 0.04	$0.723^{+0.079}_{-0.073}$	$0.342^{+0.186}_{-0.180}$	38/33
Backw. 2 ch.	3.50 ± 0.12	0.252 ± 0.008	$1.554^{+0.690}_{-0.593}$	1.30/33
Backw. 4 ch.	3.80 ± 0.13	$0.238^{+0.007}_{-0.004}$	$3.330^{+0.950}_{-0.793}$	2.34/33

Notes to Table 3.4: a = N_H fixed to the Galactic value forward, however, the feature is less prominent ($\tau \sim 0.5 - 1.0$), but still the addition of the edge significantly improves the fits. As an example, Figure 3.4a-b illustrates the residuals of the fit with the single power law model (model a1) obtained in the cases of the maximum shift forward (6 channels; panel [a]) and for a shift back of 2 channels (panel [b]). In Table 3.4b the fits with the power law + edge to these spectra are reported.

These tests show that, again, the shifts can significantly modify the profile of an observed feature, but still do not demonstrate whether it can be created *ex novo* in an intrinsically featureless spectrum. For this purpose, a single power law spectrum with no absorption features was simulated using the FAKEIT command within XSPEC, using the same exposure and statistics as for the Nov 92 spectrum (Table 2.1), and using as input the single power law + Galactic absorption model. The residuals of the fit to this spectrum with the single power law are reported in Figure 3.5a, and are obviously featureless. The "shifting" exercise was repeated on this artificial spectrum, using the same procedure as above.

When the spectrum is shifted forward, a feature appears in the residuals at an increasing energy between 0.6 – 0.7 keV, but the optical depth is lower than that observed in the "true" spectrum. Specifically, the optical depth is consistent with zero for a shift of 2 – 3 channels, and becomes maximum ($\sim$ 0.4) in the spectrum shifted the most (6 channels). The residuals of the latter spectrum are shown in Figure 3.5b; the edge created at $\sim$ 0.6 keV is clearly visible.

Shifting the simulated spectrum backward creates an edge at decreasing energies in the small range 0.27 – 0.24 keV, and of increasing optical depth (1.0 - 4.0). The latter parameter reaches the value observed in the "true" spectrum

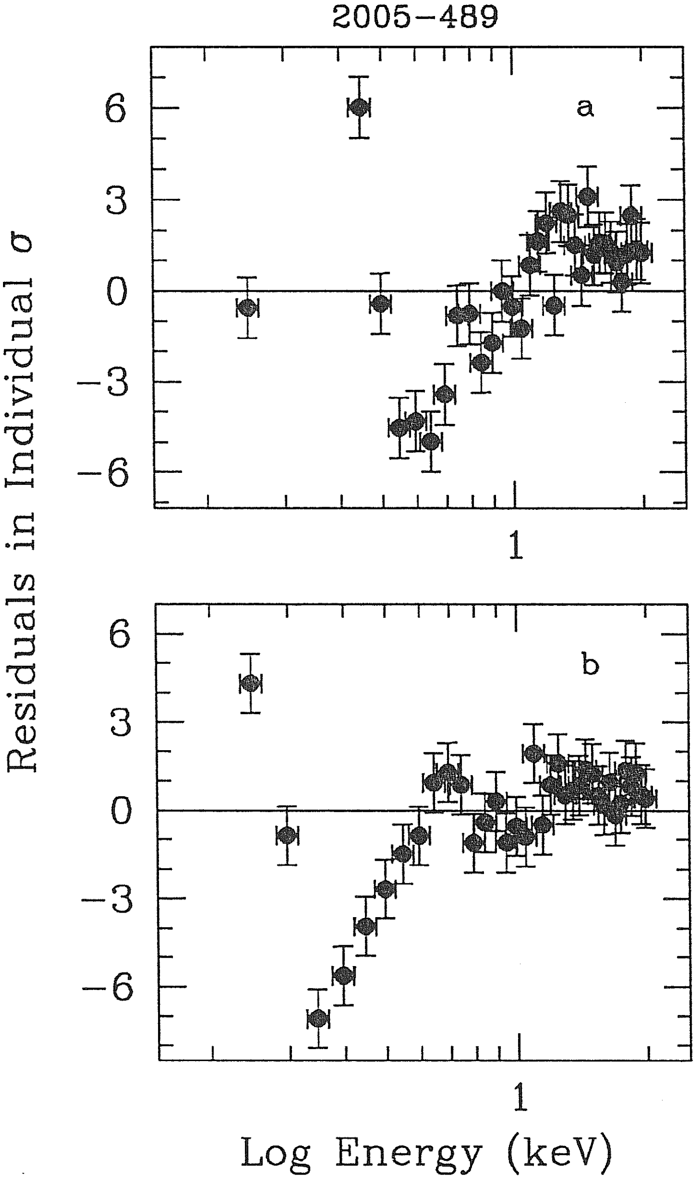

Figure 3.4: Residuals of the single power law + Galactic absorption fit to the shifted spectrum of 2005–489 (Nov observation). The shifts, which mimic the effects of the PSPC gain variations, can change the energy considerably and the depth of the feature in Figure 3.3b. *Panel a*: Residuals for the maximum shift forward (6 channels). The feature is at E ~ 0.6 keV and has an optical depth $\tau \sim 0.85$. *Panel b*: Residuals for a shift backward of 2 channels. In this case, E~ 0.25 keV and $\tau \sim 5.0$.

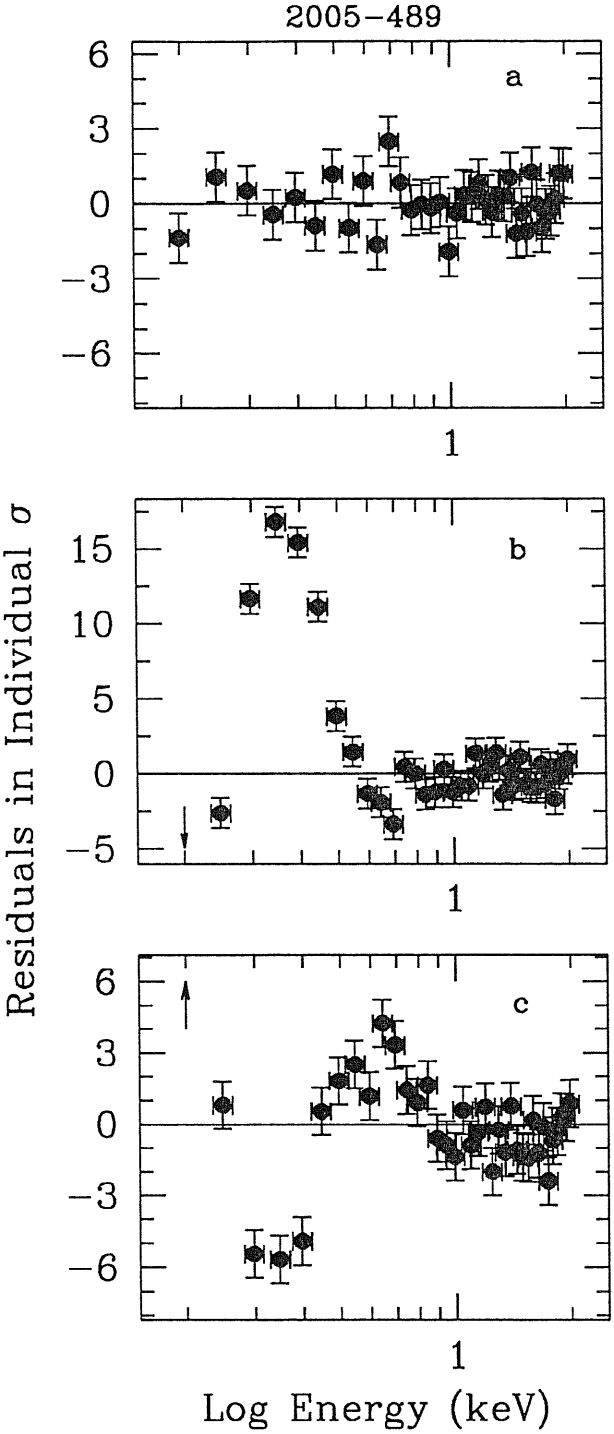

Figure 3.5: Residuals of the single power law + Galactic absorption fit to the simulated and shifted spectrum of 2005–489. The shifts can create a feature with large optical depth τ. *Panel a:* Residuals for the simulated spectrum. No features are present. *Panel b:* Simulated, shifted forward spectrum (6 channels). The energy is at $\sim$ 0.7 keV, $\tau \sim 0.34$. *Panel c:* Simulated, shifted backward spectrum (4 channels), where the feature is at $\sim$ 0.24 keV and $\tau \sim 3.3$. The arrows mark data out of range.

(Table 3.4a) for a backward shift of 4 channels. These residuals are shown in Figure 3.5c, while the fits for the shifts are summarized in Table 3.4c.

In conclusion, the artificial "shifts" described above show that an absorption feature with a large ($\sim 2-3$) optical depth can be produced in an intrinsically featureless spectrum by the gain shifts. In addition, if there is an intrinsic feature its profile *and energy* can both be modified by the shifts.

CHAPTER IV

Average X-ray Properties of Blazars

In this Chapter we study the distribution of the Rosat slopes for RBLs and compare it with those of XBLs and FSRQs observed with Rosat. A re-analysis of the IPC data for the three classes is also performed, and the derived spectra are compared to the Rosat ones. We look for correlations of the Rosat spectral indices and fluxes with the redshift and the parameters of the radio morphology.

4.1 Average Rosat Spectrum of RBLs

4.1.1 DISTRIBUTION OF THE SPECTRAL INDICES

In the following we study the distribution of the Rosat spectral indices of the 1 Jy RBLs. For each spectrum we assume the slope determined with the fit with a single power law with fixed (Galactic) absorption, because no significant excess absorption has been found from the fits with free N_H. In addition, the slopes from the fits with N_H fixed at the Galactic value are considerably more accurate then those from the fits with free N_H, allowing us to determine with higher precision the average photon index for the class.

In order to give a consistent analysis, the slopes from model a1 were considered everywhere, also in the (few) cases where indication for more complex models were derived (0716+714, 1652+398, 2005–489). Average photon indices and the rms dispersions are used for the sources with two observations (0851+202, 1749+096, and 2005-489). The weak source 0814+425, which has a very poorly determined photon index (Table 3.1), is not considered here. Spectral parameters for 1807+698 and 0454+844 were taken from Fink et al. (1991) and Brunner et al. (1994), respectively.

The distribution of the photon indices for 28 objects is shown in Figure 4.1a. A simple mean yields $\langle\Gamma\rangle = 2.20$ with standard deviation 0.46. A weighted average gives 2.72 ± 0.01, which is clearly dominated by the three objects with higher statistics (0716+714, 1652+398, 2005-489). If the latter sources are excluded, the distribution for 25 objects has a simple average 2.12 and standard deviation 0.41, with weighted average 2.33 ± 0.03.

4.1.2 INHOMOGENEITY OF THE DISTRIBUTION

The homogeneity of the distribution, that is, whether it is consistent with a single photon index value, is studied by examining the distribution of the photon index residuals. The residual for the *i-th* object is defined as

$$\frac{\Gamma_i - \langle\Gamma\rangle}{\sigma_i}, \tag{4.1}$$

where Γ_i is the measured photon index, σ_i its uncertainty, and $\langle\Gamma\rangle$ the average photon index for the whole group. The residuals thus represent the distance in individual sigma of each measured photon index from the total average value. If the sample is homogeneous, that is, all the measured values are consistent within the errors with a single average, the residual distribution should behave like a Gaussian. More precisely we expect the residuals to be distributed like a

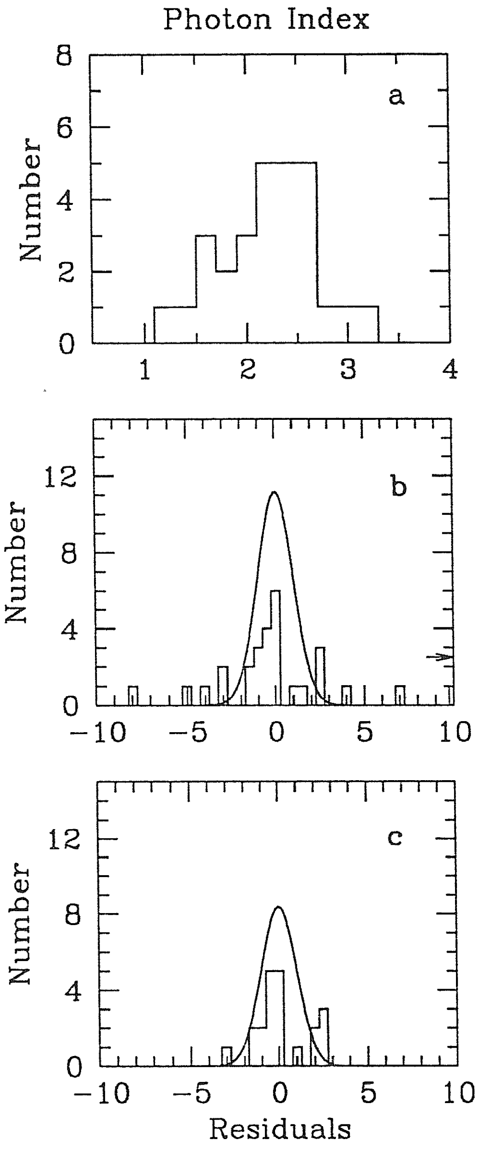

Figure 4.1: Analysis of the Rosat spectral index distribution for RBLs. *Panel a:* Distribution of the spectral slopes for the 28 RBLs. The (weighted) mean is 2.33 ± 0.03. *Panel b:* Distribution of the residuals of the previous mean. One residual, indicated by the arrow, is offscale at 20. The solid line is the Gaussian expected for a homogeneous population, normalized to N=28. The observed distribution has a significant (at $\gtrsim |3\sigma|$) intrinsic spread. *Panel c:* The distribution after removing the 7 spectra with residuals at $\gtrsim |3\sigma|$ in panel b.

Gaussian of center 0 and $\sigma = 1$.

The calculation of the residuals requires the 1σ errors for the single measured photon indices, which are derived from the 68% confidence errors (Figure 3.1a-x). The distribution of the observed residuals from $\langle\Gamma\rangle = 2.33$ is plotted in Figure 4.1b. Clearly, the observed residual distribution is not consistent with the expected Gaussian (solid line); some residuals are present at $\gtrsim |3\sigma|$. As a measure of the deviation from the Gaussian we define χ^2_T = the sum of the square of the residuals; for the residuals in Figure 4.1b, χ^2_T=677.87, with a corresponding $P_{\chi^2} < 10^{-9}$ for 27 degrees of freedom.

The residuals at $\gtrsim +3\sigma$ correspond to the spectra of 0048–097, 0716+714, and 2005–489, which have slopes in the range 2.4 – 3.0 ("steep tail"). The objects corresponding to the residuals at $\lesssim$ -3σ are 0954+658, 1308+326, 1538+149, and 1823+568, which have flat spectra, with a mean at $\langle\Gamma\rangle = 1.66 \pm 0.07$ ("flat tail"). If these seven sources are excluded, the remaining objects are distributed around an average photon index of 2.34 ± 0.04, and the distribution of the residuals behaves in better agreement with the expected Gaussian (Figure 4.1c). The χ^2_T drops to 36, lower albeit still rather poor ($P_{\chi^2} \sim 1.5\%$, for 19 degrees of freedom).

A more sophisticated method to examine whether there is an intrinsic spread is the maximum likelihood test. This method (e.g., Maccacaro et al 1988; Worrall & Wilkes 1990) assumes that the intrinsic distribution of the spectral indices is Gaussian with center Γ_p and dispersion σ_p. The following quantity (likelihood) is calculated:

$$L = \prod_{i=1}^{n} \frac{1}{\sqrt{2\pi(\sigma_i^2 + \sigma_p^2)}} \exp^{-\frac{(\Gamma_i - \Gamma_p)^2}{2(\sigma_i^2 + \sigma_p^2)}}, \tag{4.2}$$

where n is the number of measurements.

By minimizing the likelihood or, equivalent, by maximizing the quantity $S = -2 \times \ln L$, one derives the best-fit values of Γ_p, σ_p and their uncertainties at a given confidence.

In practice one has to use the 1σ measurement errors. Inspection of Figure 3.1 shows that not in every case are the 68% confidence contours perfectly Gaussian, as a result of the poor statistics. In these cases we use as the error the average of the 68% uncertainties.

The 90% confidence contour (ΔS=4.6) for Γ_p, σ_p is shown in Figure 4.2 for the whole group of RBLs (solid line), while in dotted line is the 90% contour for the restricted group obtained by removing the steep and flat tail of the distribution in Figure 4.1b. The dispersion is reduced from $0.44^{+0.21}_{-0.12}$ to $0.22^{+0.16}_{-0.14}$, although it is still not consistent with zero, while the average value of the photon index is substantially unchanged between the solid and dotted curve ($\langle\Gamma\rangle \sim 2.2$). The maximum likelihood results are reported in Table 4.1a, together with the mean values derived from the simple and weighted average.

The inhomogeneity of the distribution will be reconsidered in Chapters 5 and 6 with reference to the multifrequency spectra of Blazars. Here, we wish to remark that the objects of the steep and flat tails have properties that set them apart from the other RBLs. For example, the steep source 2005–489 is often classified as an XBL because of its X-ray brightness, and shows an X-ray spectral shape and variability in 0.1 – 10 keV similar to other XBLs (Sambruna et al. 1994a,b). On the other hand, the sources in the flat tail have properties more consistent with those of quasar-like Blazars. A broad optical emission line (EW ~ 35 Å) has been detected from 1308+326, as have weak lines from all the other objects (Stickel et al. 1993). Three sources (0954+658, 1308+326, and 1823+568) have a radio morphology consistent with an FRII galaxy (Koll-

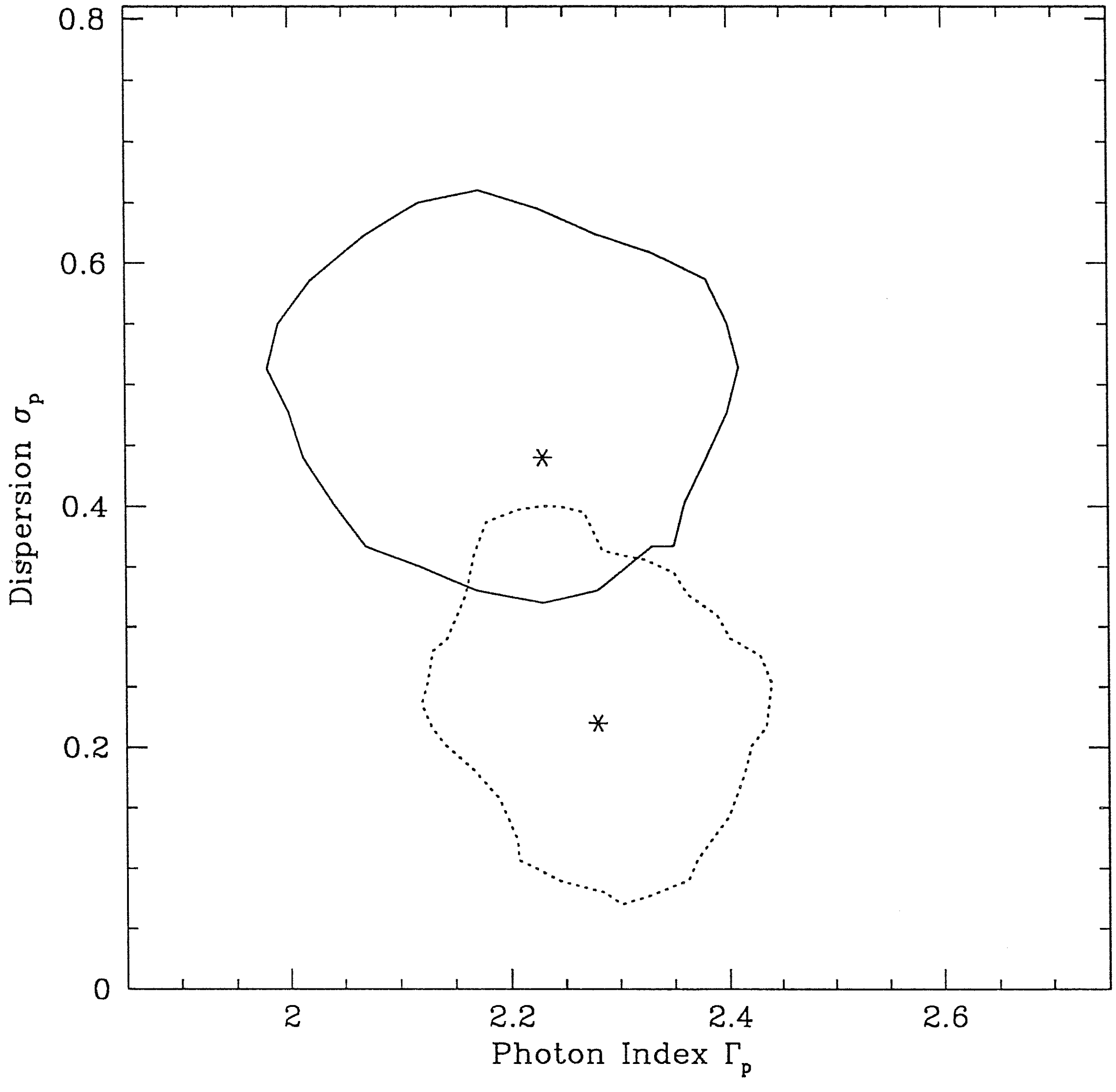

Figure 4.2: Maximum likelihood analysis. Confidence contours at 90% and best-fit values (stars) are reported. Solid line: contour for the whole sample of 28 objects. Dotted line: contour after removing the spectra with slopes different from the mean at $\gtrsim |3\sigma|$. The dispersion decreases, while the range spanned by the photon index is almost unchanged in the two cases.

gaard et al. 1992) and very fast superluminal speeds (Gabuzda & Sitko 1994). 0954+658 shows the highest known polarization in radio, with the polarization angle oriented at large angles from the jet axis, contrary to other RBLs of the 1 Jy sample for which these angles are nearly zero (Gabuzda et al. 1992).

The spread of the distribution of the X-ray slopes may thus reflect some intrinsic inhomogeneity of the sample, as if the radio selection picks objects with "intermediate" properties between XBLs and FSRQs. While these Intermediate Blazars (Kollgaard 1994) are clearly interesting cases *per se*, they seem to indicate the presence of "connecting objects" inside the whole Blazar class.

4.2 Different Blazar Classes Observed with Rosat

As discussed in Chapter 2, Rosat observed in pointed mode the complete XBL sample of the *Einstein* Extended Medium Sensitivity Survey. The data were analyzed by Perlman et al. (1994). Spectral analysis was performed for 21 sources using a single power law + absorption model. For a direct comparison with RBLs, in the following we will use only the results of the fits with a single power law + Galactic absorption.

The distributions of the spectral indices are shown in Figure 4.3, top panel for RBLs and central panel for XBLs. The EMSS objects are represented with the solid line, while the shaded area in the central panel represents the LASS XBLs from Brinkmann & Siebert (1994). The photon index distribution for RBLs and EMSS XBLs are not different, the Kolmogorov-Smirnov (KS) test giving a probability P_{KS} that the two distributions are drawn from the same parent population of $\sim 94\%$. The means are 2.20 ± 0.46 for RBLs and 2.23 ± 0.40 for EMSS XBLs, and a Student's t-test yields a probability that the two means are different of only 4% (for variances not significantly different, $\sim$ 50%).

The LASS XBLs have a distribution of slopes consistent with the EMSS XBLs. If the distribution of RBLs is compared to the joint EMSS + LASS group, the KS test gives a probability $P_{KS} \sim 99\%$ that the two distributions are drawn from the same parent one (Table 4.2).

As described in Chapter 2, Rosat spectral measurements are also available for a sample of 8 (Brunner et al. 1994) + 5 FSRQs. Fits to the Rosat spectra with the single power law model for the last 5 objects, whose data were retrieved from the archive, are reported in Appendix 1. The distribution of the spectral indices is shown in the bottom panel of Figure 4.3, with the objects of Brunner et al. (complete sample) represented as the solid histogram and the remaining sources represented by the shaded area. A simple average of the spectral indices yields 1.67 ± 0.54 for the whole group of 13 objects, with the five objects not in the complete sample being clustered at steeper slopes. The distribution for FSRQs spans a range of flatter photon indices than that of RBLs and XBLs, with a probability to be drawn by the same parent distribution of $\sim$ 2% in both cases (Table 4.2). The mean for FSRQs is different with high significance ($\sim$ 99%) from that of RBLs and XBLs.

A comparison of the intrinsic distributions for the three classes is shown in Figure 4.4, where the 90% confidence contours for Γ_p, σ_p are reported. This Figure confirms that while RBLs and XBLs have similar energy distributions in 0.1 – 2.0 keV, both classes are steeper than FSRQs. The average photon indices are summarized in Table 4.1a.

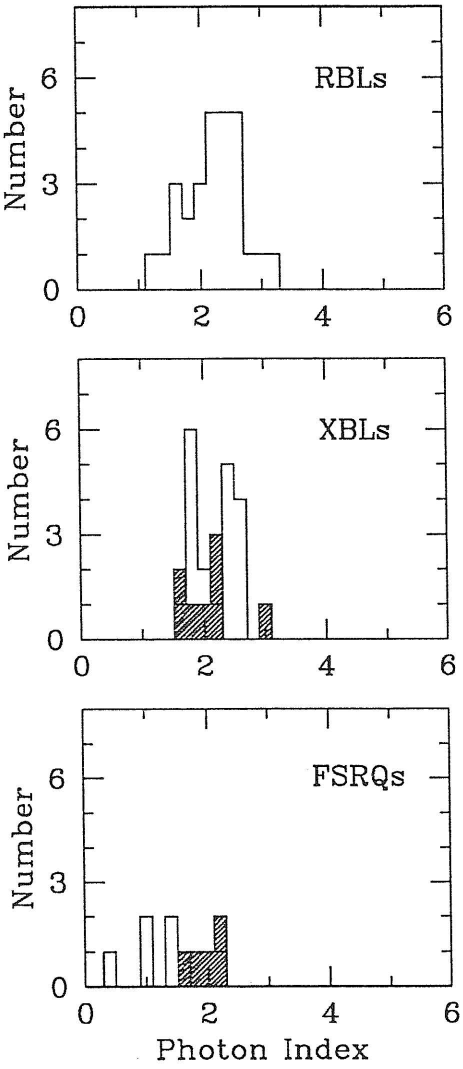

Figure 4.3: The Rosat spectral index distributions for RBLs (top panel) is compared to those of other Blazar classes observed with Rosat. *Central panel*: The distribution for XBLs is reported. Besides the complete EMSS XBL sample (from Perlman et al. 1994; solid histogram), the subsample of the LASS XBLs from Brinkmann & Siebert (1994) is given (shaded area). *Bottom panel:* Distribution for FSRQs, with the complete sample of Brunner et al. (1994) in solid line and 5 objects from the Pearson & Readhead (1988) sample (shaded area). No differences are present between RBLs and XBLs; both are steeper than FSRQs.

Table 4.1: Average Photon Indices

		N	Simple	Weighted	Max. Lik.	
					Γ_P	σ_P
			a: Rosat			
RBLs		28	2.20±0.46	2.72±0.02	$2.23^{+0.17}_{-0.25}$	$0.44^{+0.21}_{-0.12}$
		25 [a]	2.12±0.41	2.33±0.03	…	…
XBLs	EMSS	21	2.24±0.40	2.22±0.02	$2.21^{+0.17}_{-0.23}$	$0.38^{+0.15}_{-0.12}$
	LASS	9	2.14±0.40	2.22±0.01	$2.17^{+0.28}_{-0.21}$	$0.28^{+0.37}_{-0.09}$
FSRQs		13	1.67± 0.54	1.84±0.03	$1.75^{+0.30}_{-0.40}$	$0.37^{+0.33}_{-0.19}$
			b: IPC			
RBLs		11	1.59±0.29	1.84±0.06	$1.71^{+0.24}_{-0.31}$	$0.18^{+0.32}_{-0.18}$
XBLs	LASS	4	2.27±0.55	1.88±0.03	…	…
FSRQs		4	1.14±0.59	1.55±0.09	…	…

Notes to Table 4.1: a= Without the 3 sources with higher statistics.

Table 4.2: Rosat Distributions KS Results

	N	RBLs	XBLs [a]	FSRQs
RBLS	28	…	0.989	0.024
XBLS [a]	30	…	…	0.022
FSRQs	13	…	…	…

Notes to Table 4.1: a= Joint EMSS + LASS groups.

4.3 Comparison with Previous Measurements

Eleven RBLs in the Rosat sample were previously observed with the *Einstein* IPC instrument in the range 0.3 – 3.5 keV. These data were analyzed by Worrall & Wilkes (1990) together with those of other Blazars. However, only the results of the fits performed with free N_H were published. The derived spectral indices are affected by very large errors, mostly due to the low sensitivity of the IPC experiment. In order to perform a uniform comparison with the Rosat slopes, the IPC data of the 11 objects in common between the IPC and Rosat samples were re-analyzed assuming a single power law + fixed (Galactic) N_H. The results are reported in Table 4.3a, where the photon indices and the flux densities at 1 keV from the fits with a single power law and Galactic N_H are listed. The errors are 90% errors; for the slopes, we wrote apart the 68% errors for future reference. For the objects observed more than once by both satellites, average values of the slopes and of the flux densities will be used in the following.

Figure 4.5 (top panel) compares the distribution of the spectral indices from Rosat (solid line) to those obtained from the IPC experiment (shaded area). The distribution of the IPC slopes is clearly spanning a range of flatter values than the Rosat one, with a (simple) mean 1.59 ± 0.29, while for the Rosat distribution the mean is 2.26 ± 0.43. The two mean values are different at 99.9 86%) and the probability that the two distributions are drawn from the same parent population is only 0.06%. We can conclude that the IPC spectra of RBLs are significantly flatter than their Rosat counterparts.

The above result is confirmed by a maximum likelihood analysis (Figure 4.6). Again, the confidence contour for the IPC encloses a region of flatter slopes than for Rosat. Moreover, the dispersion in this case is consistent with zero,

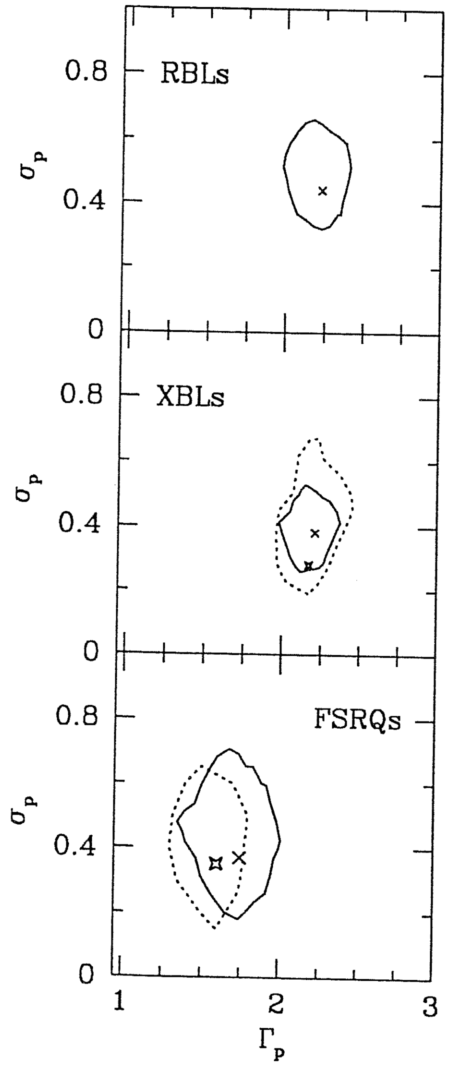

Figure 4.4: Contours at 90% confidence and best-fit values from the maximum likelihood test for the Rosat slope distributions of Blazar classes. The RBL contour (top panel) is compared to XBLs (middle panel) and FSRQs (bottom panel). *Central panel:* Dotted line + star = LASS XBLs, solid line + cross = EMSS XBLs. *Bottom panel:* dotted line + star = the 8 FSRQs of Brunner et al. (1994), solid line + cross = the whole group of 13 FSRQs. RBLs and XBLs span the same range of photon indices, both steeper than FSRQs.

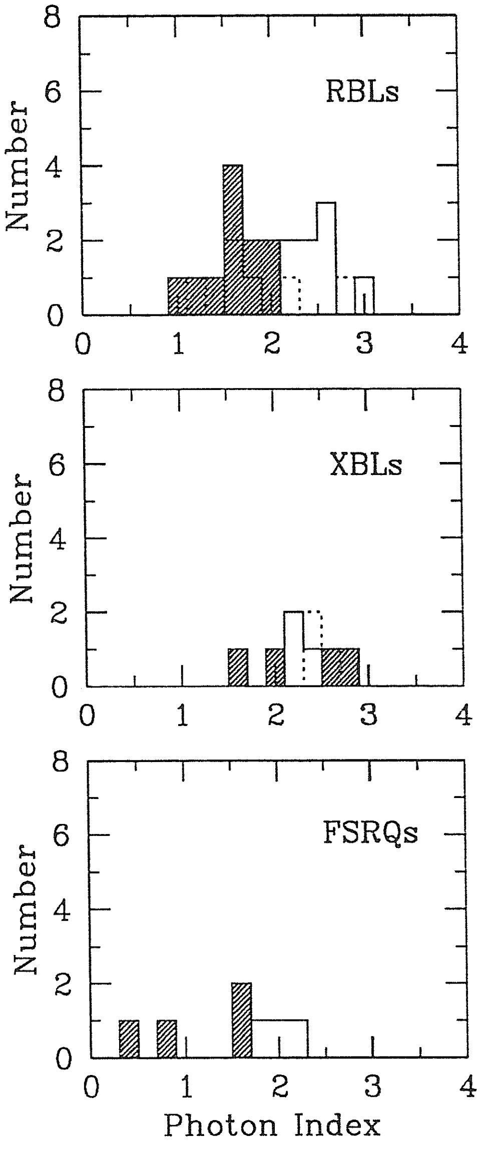

Figure 4.5: Comparison of the Rosat (solid histograms) and the IPC (shaded area) spectral index distributions for 11 RBLs (top), 4 LASS XBLs (middle), and 4 FSRQs (bottom) observed by both satellites. The IPC spectra of RBLs are flatter than the Rosat ones (top). For both XBLs and FSRQs, the IPC and Rosat spectra do not differ.

indicating that the IPC distribution is consistent with a single value of the mean slope.

The flatness of the IPC slopes can not be entirely due to an effect of variability. If the flux densities obtained with Rosat and IPC are compared (Figure 4.7), long-term variability is apparent. However, this does not follow a specific trend, that is, the sources were not caught all in the same bright/faint mode by the same satellite. For example, three sources (1652+398, 2200+420, and 1538+149) were observed by Rosat in a fainter state than with the IPC, while in the case of 0716+714 and 0537-441 the Rosat data were obtained in a brighter mode. For the remaining four cases, the Rosat and IPC fluxes do not differ.

In the case of XBLs, only 4 of the LASS objects were previously observed by the IPC. Among FSRQs, only 4 objects were observed with statistics high enough to allow the analysis of the spectra. The results of the fits with a single power law + Galactic absorption are reported in Table 4.3b-c. The observed distributions of the IPC slopes are compared to the Rosat values in Figure 4.5. Contrary to RBLs, no differences are present between the distributions obtained with the two satellites for XBLs and FSRQs, with average slopes $\Gamma \sim 2.3$ for XBLs and ~ 1.1 for FSRQs (Table 4.1b). We stress, however, that the IPC samples of XBLs and FSRQs consist of a very limited number of objects in both cases.

It has been suggested that the flatter slopes of AGNs measured with the IPC with respect to those measured with Rosat could be attributed to a different calibration of the spectral responses of the two satellites, although on the basis of a few objects (Fiore et al. 1994). In our case, although based on a limited statistics, the fact that the IPC distributions for XBLs and FSRQs

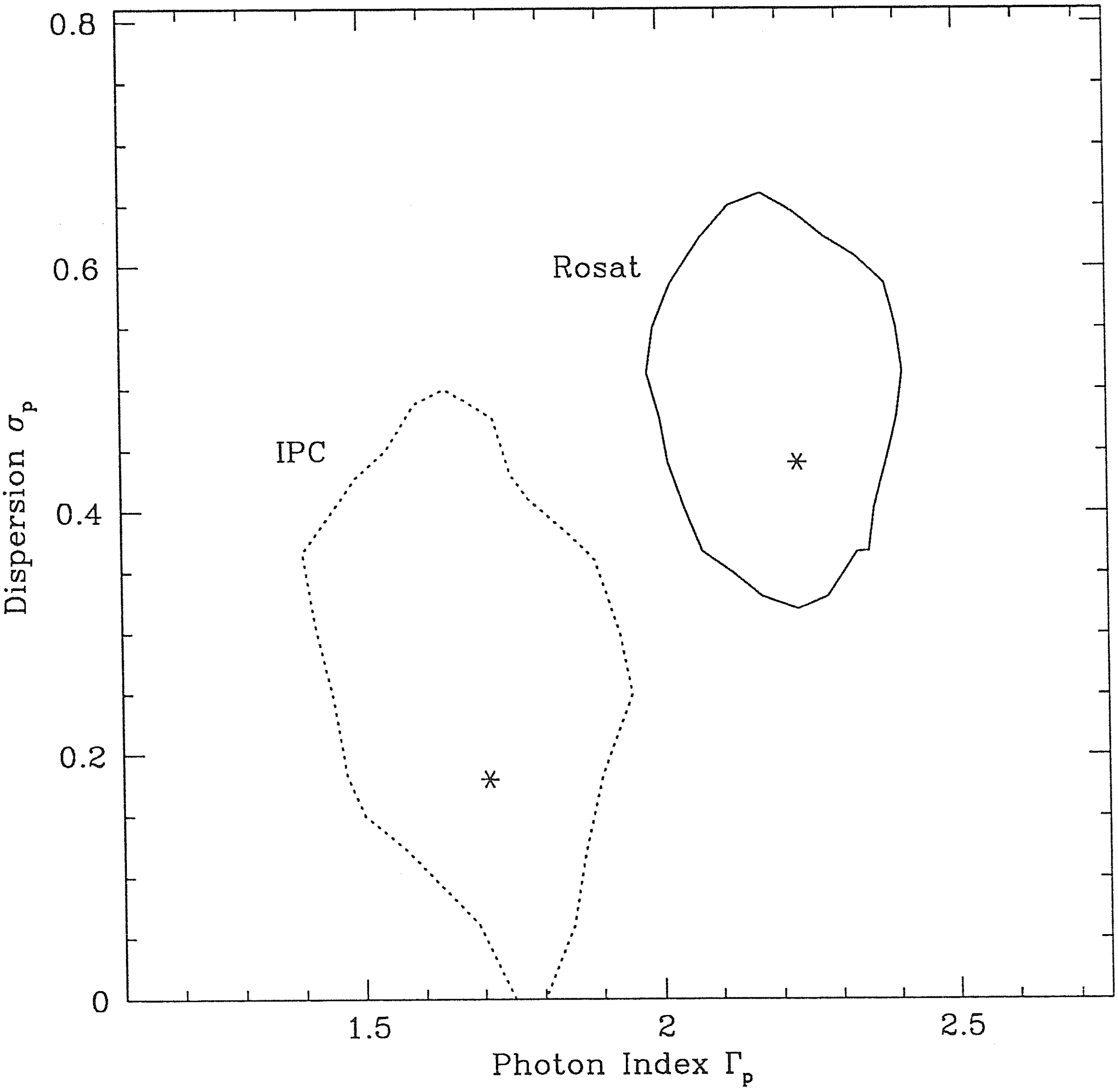

Figure 4.6: Contours (90% confidence) and best-fit values from the maximum likelihood analysis of the Rosat (solid line) and IPC (dotted line) slope distributions of 11 RBLs observed by both satellites. The IPC intrinsic distribution spans a range of flatter indices than the Rosat one, and is consistent with a unique value of the photon index.

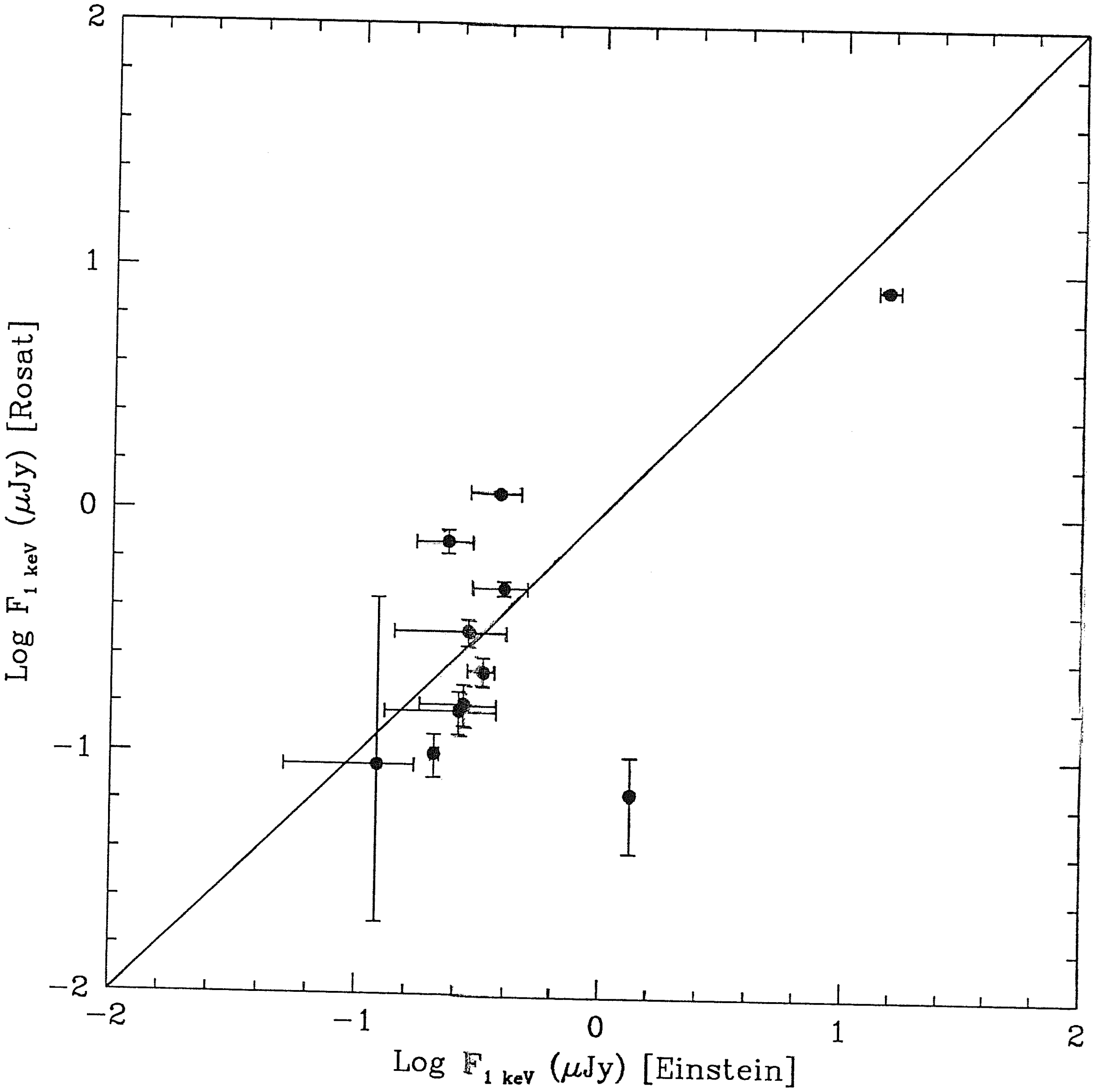

Figure 4.7: Long-term time variability of RBLs. The Rosat flux densities at 1 keV are plotted against the IPC ones. Four objects were observed by Rosat in a fainter state than with the IPC, while two objects were brighter at the time of the Rosat observations.

do not differ from those obtained with Rosat do not support this suggestion. Clearly, a comparison involving a larger number of objects is necessary in order to further discuss this point.

Data at higher energies (up to ~ 10 keV) were obtained for a relatively large number of Blazars with the Exosat satellite (Sambruna et al. 1994a,b). Only three RBLs of the Rosat/IPC group have Exosat spectra above 2 keV (1652+398, 0537–441, 1807+698). Their slopes span a rather wide range (dotted line in Figure 4.5). The distributions of the Exosat slopes for XBLs are consistent with the Rosat and IPC ones (Figure 4.5).

Among FSRQs, only for 1928+738 Exosat spectra are available, all obtained in an intensity state similar to the Rosat one (Brunner et al. 1994). The photon indices derived are in the range 1.6 – 2.5, and are consistent with the value derived from Rosat (1.80 ± 0.08).

Final Remarks:

We have found that the Rosat distributions of RBLs and XBLs in the range 0.1 – 2.0 keV do not differ, both being centered on steep values of the photon index ($\Gamma \sim 2.2$). Both are steeper than the distribution for FSRQs ($\Gamma \sim 1.6$). While the average IPC spectra of XBLs and FSRQs are not different from the Rosat ones, in the case of RBLs the slope distribution obtained with the IPC is flatter than with Rosat, with $\Gamma \sim 1.6$. This flat component is possibly associated to a Compton component emerging above ~2 keV in the X-ray spectra of RBLs.

Table 4.3: ***Einstein*** **IPC Observations of Blazars**
a) RBLs

Object	ID #	Date	Single Power Law ^{a}			
			Γ: 90% err.	68% err.	χ_r^2/d.o.f.	Flux$_{1keV}$ (μJy)
0537-441	7499	7 Apr 80	$1.71^{+0.81}_{-0.96}$	(+0.62,–0.71)	0.87/8	$0.19^{+0.05}_{-0.06}$
	7501	27 Sep 80	$1.46^{+0.61}_{-0.71}$	(+0.47,–0.53)	0.91/7	$0.27^{+0.07}_{-0.09}$
0716+714	5120	19 Oct 79	$1.53^{+0.54}_{-0.60}$	(+0.41,–0.45)	1.34/7	0.37 ± 0.09
0735+178	5695	31 Mar 80	$1.82^{+0.18}_{-0.20}$	(+0.14,–0.15)	0.66/8	0.29 ± 0.02
	7496	9 Oct 80	$2.16^{+0.55}_{-0.59}$	(+0.42,–0.44)	0.67/6	$0.37^{+0.08}_{-0.07}$
	7497	26 Mar 81	$2.00^{+0.63}_{-0.68}$	(+0.48,–0.51)	0.64/6	$0.31^{+0.06}_{-0.08}$
1538+149	3073	14 Aug 79	$1.48^{+0.95}_{-1.29}$	(+0.74,–0.92)	0.67/5	$0.20^{+0.07}_{-0.10}$
	7728	7 Aug 80	$1.83^{+0.64}_{-0.74}$	(+0.49,–0.55)	0.86/6	0.21 ± 0.05
1652+398	2001	30 Jul 79	1.96 ± 0.07	$\pm$ 0.06	0.48/9	15.54 ± 0.73
	5210	19 Jan 80	2.02 ± 0.05	$\pm$ 0.05	0.53/8	$13.28^{+0.46}_{-0.40}$
	5211	15 Aug 80	1.86 ± 0.06	$\pm$ 0.05	1.07/8	$16.34^{+0.60}_{-0.53}$
1749+096	3899	25 Sep 79	$1.05^{+1.17}_{-1.45}$	(+0.95,–1.05)	0.31/4	$0.28^{+0.12}_{-0.14}$
1803+784	5121	30 Oct 79	$1.80^{+0.90}_{-1.21}$	(+0.72,–0.88)	0.43/7	0.27 ± 0.09
1807+698	5689	31 Mar 80	1.88 ± 0.22	$\pm$ 0.17	1.4/7	$0.46^{+0.04}_{-0.03}$
	9420	13 Dec 80	$1.33^{+0.73}_{-0.87}$	(+0.57,–0.64)	0.60/7	$0.32^{+0.10}_{-0.13}$
2007+777	5122	29 Oct 79	$1.75^{+1.12}_{-1.24}$	(+0.85,–0.91)	0.50/6	$0.26^{+0.10}_{-0.13}$
2200+420	5693	8 Jun 80	$1.20^{+0.30}_{-0.31}$	(+0.23,–0.24)	1.6/8	1.34 ± 0.02
2254+074	7729	20 Jun 80	$1.37^{+1.19}_{-1.54}$	(+0.91,–1.1)	0.33/7	$0.12^{+0.05}_{-0.07}$

Table 4.3: *continued*
b) XBLs

Object	ID #	Date	Single Power Law ^{a}			
			Γ: 90% err.	68% err.	χ^2_r/d.o.f.	Flux_{1keV} (μJy)
0548-322	3069	28 Feb 79	1.58 ± 0.08	± 0.06	1.71/7	9.56 ± 0.33
	2707	10 Oct 79	1.60 ± 0.09	± 0.07	1.75/8	$10.10^{+0.40}_{-0.46}$
	7726	3 Mar 80	1.68 ± 0.10	± 0.08	1.47/7	8.97 ± 0.40
1101+384	5207	20 Nov 79	$3.22^{+0.21}_{-0.17}$	(+0.16,–0.13)	1.1/6	$3.91^{+0.63}_{-0.65}$
	5208	12 May 80	2.38 ± 0.05	± 0.05	1.6/7	$20.92^{+0.66}_{-0.73}$
1133+704	4601	13 Nov 79	2.00 ± 0.08	(+0.06,–0.04)	0.98/9	$8.97^{+0.33}_{-0.40}$
	9157	28 Dec 80	2.05 ± 0.09	± 0.07	0.12/5	$4.56^{+0.19}_{-0.18}$
2155-304	5201	5 Nov 79	2.48 ± 0.05	(+0.04,–0.03)	1.78/9	$18.40^{+0.53}_{-0.46}$
	5202	15 May 80	2.84 ± 0.06	± 0.05	0.74/7	6.97 ± 0.33
c) FSRQs						
0212+735	7584	13 Mar 80	$1.20^{+0.81}_{-0.88}$	(+0.62,–0.66)	0.71/7	0.47 ± 0.21
	10235	16 Jan 81	$0.35^{+0.56}_{-0.63}$	(+0.43,–0.47)	1.88/6	$0.20^{+0.09}_{-0.08}$
1928+738 ^{b}	7589	5 Apr 80	0.50	(+0.35,–0.37)	0.90/8	0.65 ± 0.11
0923+392	554	19 Oct 79	1.64 ± 0.22	± 0.17	2.64/8	0.44 ± 0.04
1641+399	2060	27 Aug 79	$1.57^{+0.38}_{-0.43}$	± 0.23	0.46/8	0.64 ± 0.11
	2061	24 Jan 80	1.76 ± 0.34	± 0.25	0.62/8	0.64 ± 0.12
	5694	12 Feb 80	$1.60^{+0.23}_{-0.27}$	(+0.28,–0.30)	0.63/7	0.76 ± 0.09

Notes to Table 4.3: a=Fits with N_H fixed to the Galactic values; b=From Brunner et al. (1994; see text).

It is of crucial importance to verify the presence of a flatter component in the spectra of RBLs using data obtained in a harder range. This opportunity is now presented by the ASCA satellite, which operates in the range 0.5 – 10 keV and which has higher sensitivity with respect to the previous missions.

4.4 Correlations

In this Section we check for possible dependences of the shape of the X-ray spectrum on other interesting parameters, like the redshift, the 1 keV luminosity, and various radio quantities (extended and core luminosities, extended-to-core power ratio). All intrinsic properties are calculated assuming $H_0 = 50$ km s^{-1} Mpc^{-1} and $q_0 = 0.5$.

4.4.1 X-RAY SPECTRAL INDEX VERSUS REDSHIFT AND X-RAY LUMINOSITY

a) Redshift

A dependence of the X-ray photon index on the redshift is a clue of the shape of the spectrum at the higher energies. For example, the X-ray slopes of a sample of optically selected quasars observed with Rosat are found to be flatter with increasing redshifts (Brunner et al. 1994). This is interpreted as being due to a break in the mean X-ray quasar spectrum, occurring at ~ 1 keV in the rest-frame energy, which is gradually shifted into the Rosat sensitivity range. For radio-selected Blazars, we would expect to see a similar trend of flatter spectra for the more distant sources. In fact, the beaming model predicts the presence of a flat component at the higher energies, because of the emerging

Compton components in the outer parts of the jet which can be intercepted at small viewing angles (Ghisellini & Maraschi 1989). [1]

Figure 4.8 shows the plot of the photon index Γ versus the redshift for the Blazar samples. RBLs are plotted as filled circles; lower limits on the redshifts are indicated by arrows. No particular trends are visible for this class, the points being distributed like in a scatter plot. This conclusion does not change if XBLs are added (open circles). However, FSRQs (crosses), which add significantly to the high redshift end, introduce a trend of flatter slopes with increasing distances. With the non-parametric Spearman-Kendall test, the correlation probability P_{SK} for the whole Blazar group is $\sim 99.3\%$. This correlation is entirely due to FSRQs, because the probability for RBLs + XBLs is negligible ($\sim 30\%$) while for FSRQs alone is $\sim 99.6\%$.

---

[1] Note that a Compton component is expected to be present in the X-ray spectra of radio-selected Blazars also in the Giommi & Padovani model.

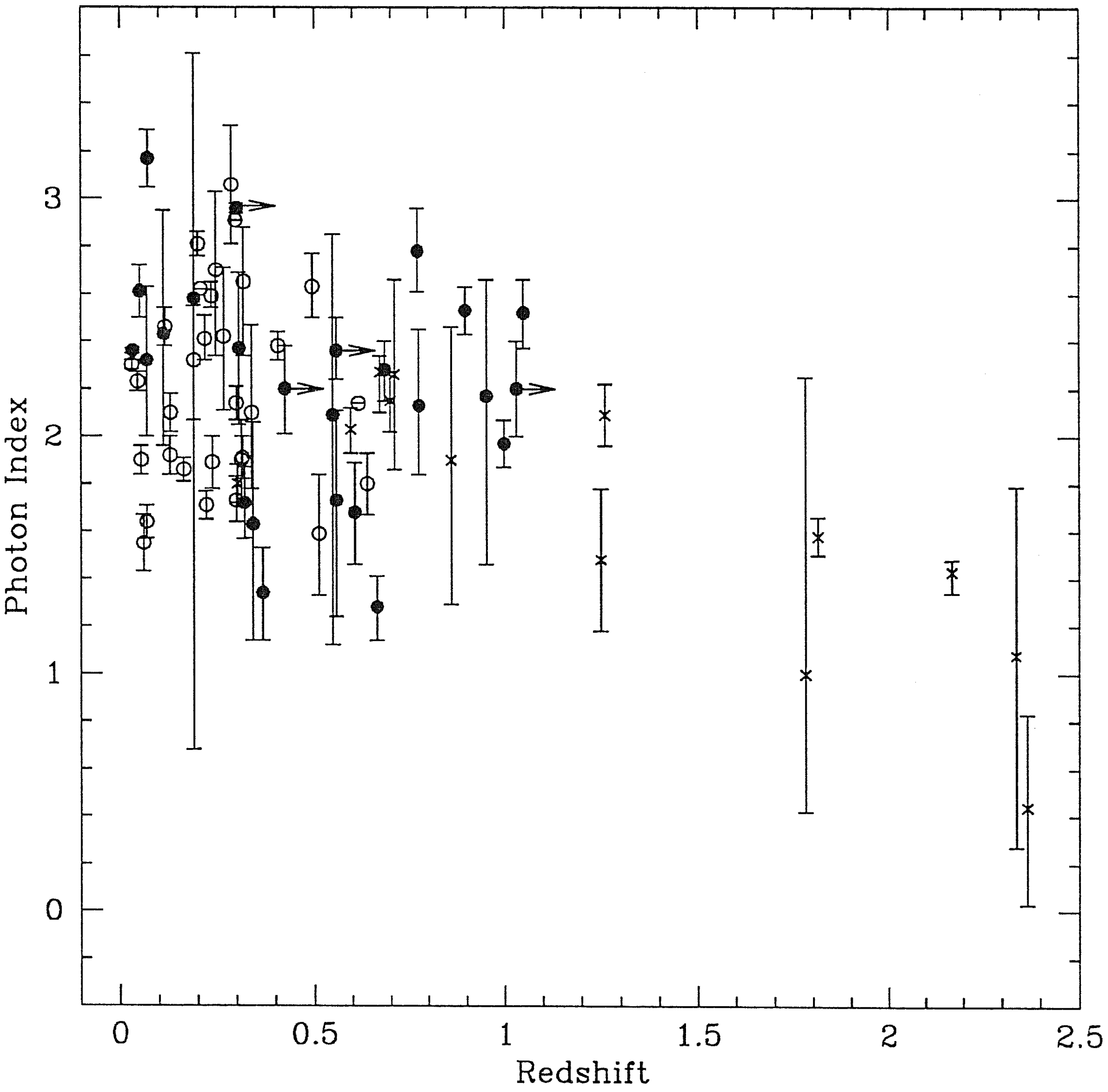

Figure 4.8: Plot of the Rosat photon index versus the redshift. Filled circles are RBLs, open circles are XBLs, crosses are FSRQs. Lower limits on the redshift are indicated by the arrows. A trend of flatter slopes with increasing distances, significant at 99%, is introduced by FSRQs. No correlation is present for the BL Lac class alone (RBLs + XBLs).

b) X-ray Luminosity

Figure 4.9 shows the plot of the X-ray photon index against the luminosity at 1 keV. Again, for RBLs alone no correlations are present ($P_{SK} \sim 77\%$). The luminosity spread is large: the majority of sources are clustered in the luminosity range $10^{26.5} - 10^{28}$ ergs s^{-1} keV^{-1}, two objects are very luminous, $\sim 10^{29}$ ergs s^{-1} keV^{-1} (0537–441 and 1144–379), and two others are at luminosities $\lesssim 10^{26.5}$ ergs s^{-1} keV^{-1} (1807+784 and 0454+844).

We add XBLs and FSRQs. The XBLs occupy a region in the plane photon index - luminosity which is substantially the same as RBLs; the 2-dimensional KS test (Peacock 1983; Fasano & Franceschini 1987) yields a probability $P_{2DKS} \sim 93.2\%$ that the two bi-dimensional samples are drawn from the same parent population. On the contrary, FSRQs are significantly flatter and brighter than the BL Lacs ($P_{2DKS} \sim 0.004\%$).

Apparently, there is a correlation of the slope and the luminosity for the three classes together, with $P_{SK} \sim 97.4\%$, with a trend of flatter slopes at higher luminosities. However, if the common dependence of the luminosity and slope on the redshift is removed with a partial correlation analysis (e.g., Padovani 1992b; see also next Chapter), the probability of correlation drops to a small value ($\sim 60\%$). We thus conclude that the X-ray spectral shape depends primarily on the redshift rather than the X-ray luminosity.

4.4.2 X-RAY VERSUS RADIO PARAMETERS

The beaming model predicts that in Blazars seen more closely to the jet axis the radio emission is more enhanced because of beaming. The situation is schematically represented in Figure 4.10, where the angular distribution of

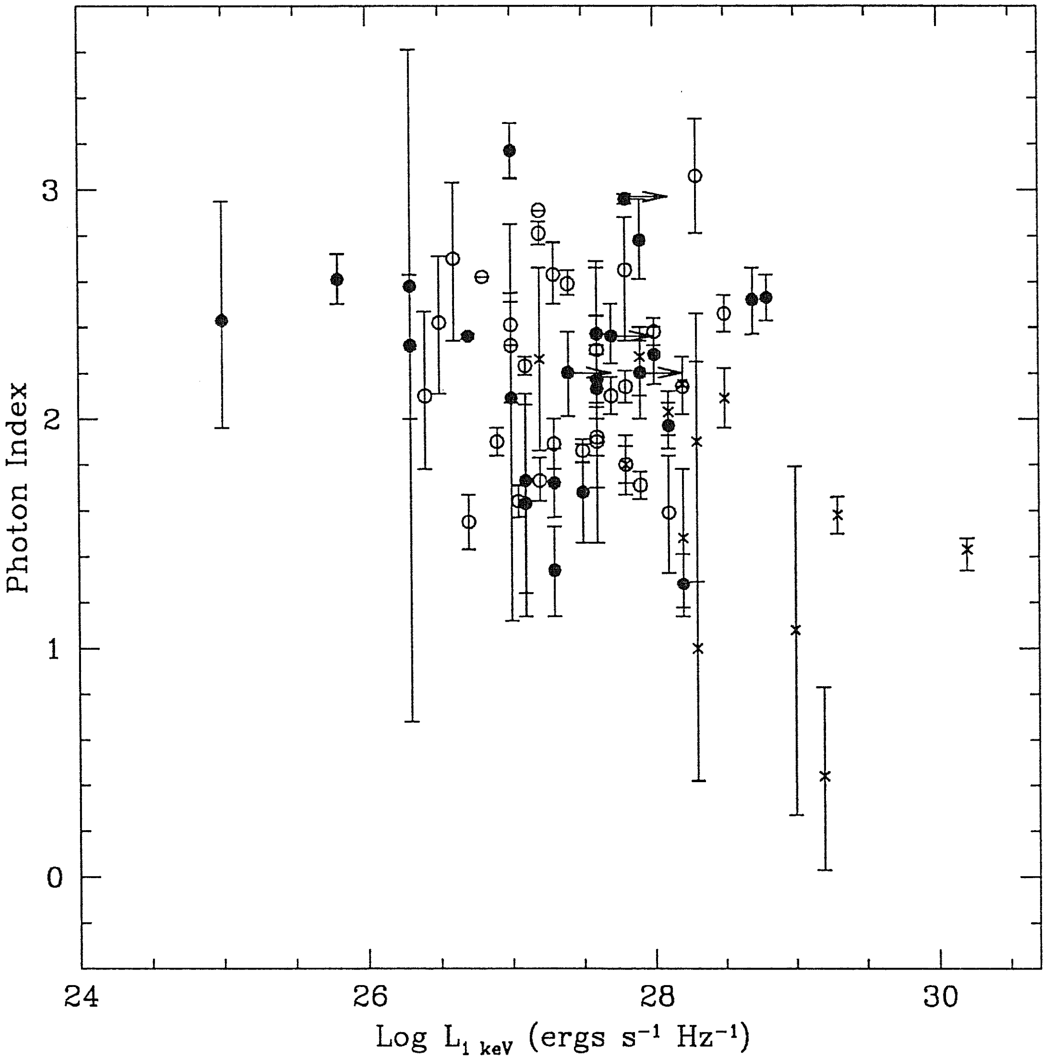

Figure 4.9: The Rosat slope is plotted versus the Rosat monochromatic luminosity. Symbols as in Figure 4.8. RBLs and XBLs span the same range of luminosities, and both are fainter than FSRQs. The apparent correlation of the slope with the luminosity for the whole Blazar sample is an effect introduced by the common dependence on the redshift.

the observed radiation is illustrated as a function of the Lorentz factor, Γ_B, of the emitting plasma. The case $\Gamma_B = 1$ represents the emission in X-rays (isotropic),[2] while the radio emission corresponds to relativistic motion ($\Gamma_B = 10$). RBLs and XBLs are separated by the critical angle ϑ_c. Within ϑ_c, a small variation of the viewing angle produces no variation of the synchrotron X-rays, and a large variation in the radio and in the associated Self Compton flux. For $\vartheta > \vartheta_c$, the variation in the viewing angle would yield little scatter of the X-ray flux and even smaller variations of the radio one.

The steepness of the Rosat spectra of RBLs and XBLs indicates a synchrotron origin of X-rays in the 0.1 – 2.0 keV range for both classes. Any observed correlation of the radio and X-ray flux would thus be due to intrinsic effects rather than to beaming.

In order to test the model we need to resolve the radio emission from the core (beamed) and from the extended lobes (isotropic). The only radio maps available for the EMSS XBLs were obtained with the Very Large Array at 1.5 GHz (Perlman & Stocke 1993). VLA data for the LASS XBLs were analyzed by Laurent-Muehleisen et al. (1993). Although radio-selected objects are largely studied in the radio with the higher spatial resolution of the VLBI, for consistency we will use VLA 1.5 GHz data also for RBLs and FSRQs. VLBI data for XBLs are under study (Kollgaard et al. 1994, in prep.).

VLA data for RBLs and FSRQs, collected from the literature, are summarized in Table 4.4, which lists the core and extended flux and power, and the ratio of the core to extended radio flux, R. This ratio was K-corrected assuming $\alpha_{ext} - \alpha_{core} = -0.7$. In the hypothesis that the core emission is the beamed fraction of the total radio emission, R turns out to be directly proportional to

---

[2] A more realistic value, $\Gamma_B \approx 3$, was derived by Padovani & Urry (1990) from the comparison of the X-ray luminosity functions of BL Lacs and their parent population (FRI).

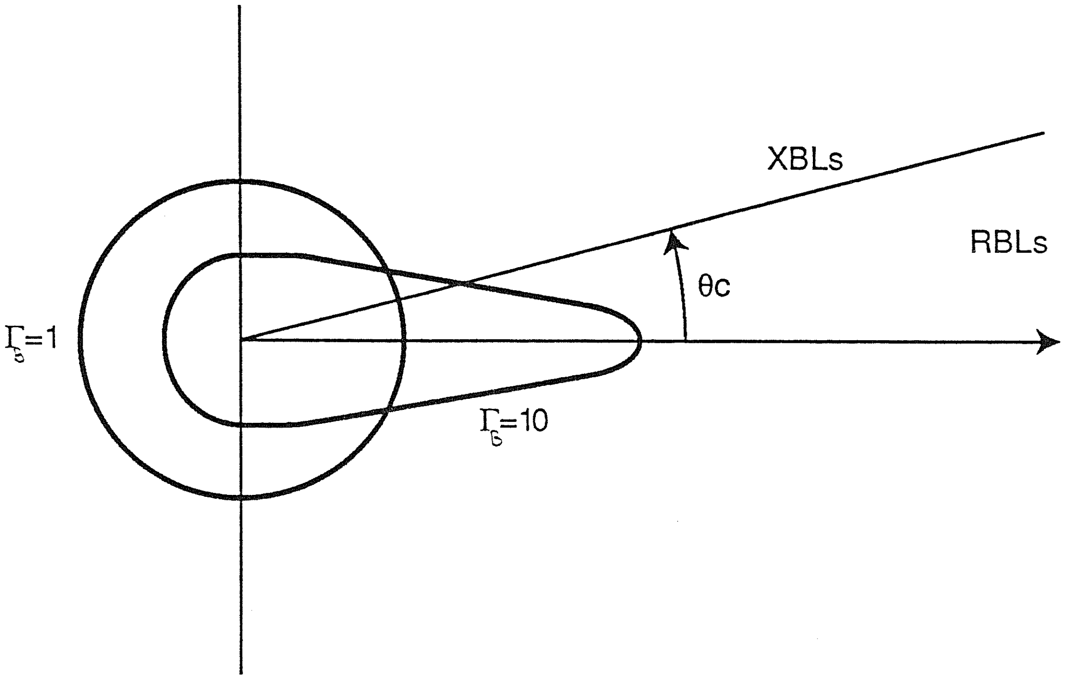

Figure 4.10: Schematic representation of the angular distribution of the radiation in the beaming model (adopted from Kollgaard 1994). The isotropic case (bulk Lorentz factor $\Gamma_{\rm B} = 1$) corresponds to synchrotron X-rays, while radio emission correspond to beamed radiation ($\Gamma_{\rm B} = 10$). Within ϑ_c, when the object appears as an RBL, large variations of the radio flux but no variation of X-rays are expected. For an XBLs ($\vartheta > \vartheta_c$), the change of viewing angle produces a little spread in X-rays and a even smaller one in the radio.

the beaming factor (e.g., Urry et al. 1991). Unfortunately, for FSRQs the value of R could be calculated for only a few cases.

The data in Table 4.4 and those for XBLs are not simultaneous to the Rosat observations and any change due to variability is expected to introduce scatter. VLBI data simultaneous to the Rosat ones for the 1 Jy RBL sample will be published by Kollgaard et al. (1994, in prep.).

Let us examine any possible dependence of the X-ray photon index from the radio parameters. Figure 4.11a-c show the plot of the X-ray photon index against the power of the radio core (panel a) and extended (panel b) components, and versus R (panel c). The only significant correlation found is in the case of the core powers (flatter Γ with higher P_{core}). However, once again the correlation is introduced by the more distant objects. No correlations or trend are present in the case of the power of the extended radio component, nor in the case of R (Figure 4.11b,c). We conclude, once again, that the Rosat data do not support the presence of a beamed component in the soft X-rays of BL Lacs.

An interesting property of Figure 4.11a is the continuity in core radio power from XBLs to FSRQs. It was previously noted (Laurent-Muehleisen et al. 1993; Perlman & Stocke 1993) that RBLs have higher core powers than XBLs, which was interpreted as support of RBLs being viewed at smaller angles than XBLs. Figure 4.11a shows that the RBLs population merge smoothly into XBLs at fainter radio powers and into FSRQs at the brighter end.

Figure 4.12 shows the plot of the X-ray flux densities at 1 keV against the flux densities of the core (a) and extended (b) radio components. The horizontal solid line marks the limiting radio threshold for the 1 Jy RBLs. The dotted vertical line at $F_x \approx 5\mu$Jy separates the fainter EMSS sample from the LASS XBLs.

Table 4.4: VLA Data (1.5 GHz)

Source	Core		Extended		R	Refs.
	F (mJy)	Log P (WHz)	F (mJy)	Log P (WHz)		
			RBLs			
0048–097	887	...	95	...	9.3	2
0118–272	780	26.9	39	25.6	14.7	5
0138–097	1220	30.0	...	...	...	6
0235+164	2052	27.7	21	25.7	61.4	2
0426–380	580	27.3	41	26.1	8.6	5
0454+844	630	25.5	...	...	...	3
0537–441	4450	28.0	45	26.0	63.2	5
0716+714	3150	>27.2	360	>26.3	9	1
0735+178	1810	27.1	92	25.8	15.4	2,4
0814+425	1460	26.6	18	24.7	69.1	5
0820+225	1600	27.6	...	...	...	6
0823+033	1320	27.1	...	...	...	6
0828+493	1030	27.0	...	...	...	6
0851+202	2040	26.9	5	24.2	338	2,3
0954+658	1360	26.8	21	25.0	52.0	3
1144–379	1610	27.7	...	...	...	6
1147+245	664	...	25	...	27	2
1308+326	1610	27.7	54	26.2	18.4	2,3
1418+546	1058	26.0	18	24.2	53.2	2
1514–241	2562	25.4	32	23.5	77.4	2
1519–273	2350	...	...	...	...	6
1538+149	1337	27.2	149	26.3	6.4	2,3
1652+398	1376	24.8	67	23.5	20.1	2,3
1749+096	774	26.5	...	...	...	2
1749+701	610	27.1	40	25.9	10.2	3
1803+784	1620	27.4	33	25.7	34.1	1,3
1807+698	1350	25.2	990	25.0	1.3	2
1823+568	1120	27.2	455	26.8	1.7	3
2005–489	1230	25.4	...	...	...	6
2007+777	983	26.6	30	25.1	26.7	1,3
2131–021	2120	27.3	51	25.7	30.5	5
2200+420	3310	25.8	40	23.9	79.0	2
2240–260	1030	27.3	...	...	...	6
2254+074	454	25.8	17	24.4	23.6	2
			FSRQs			
0016+731	1000	28.6	...	...	...	5
0133+476	1621.8	28.0	...	...	...	5
0153+744	1819.7	29.2	...	...	...	5
0212+735	2454	29.3	...	...	...	5
0615+820	865	27.5	...	...	...	5
0836+710	3743	29.4	96.8	27.8	17.2	7
0923+392	2681	26.9	615.3	26.3	3	7
1039+811	812.8	28.1	...	...	...	5
1150+812	1189	28.3	23.0	26.6	29.3	7
1633+382	2170	28.9	30.0	27.1	35.1	7
1641+399	6918.3	28.3	...	...	...	5
1928+738	2939	26.1	228.3	25.0	10.7	7

References: [1] Antonucci *et al.* 1986; [2] Antonucci & Ulvestad 1985; [3] Kollgaard *et al.* 1992; [4] O'Dea *et al.* 1988; [5] Perley 1982; [6] Padovani 1992; [7] Murphy *et al.* 1993.

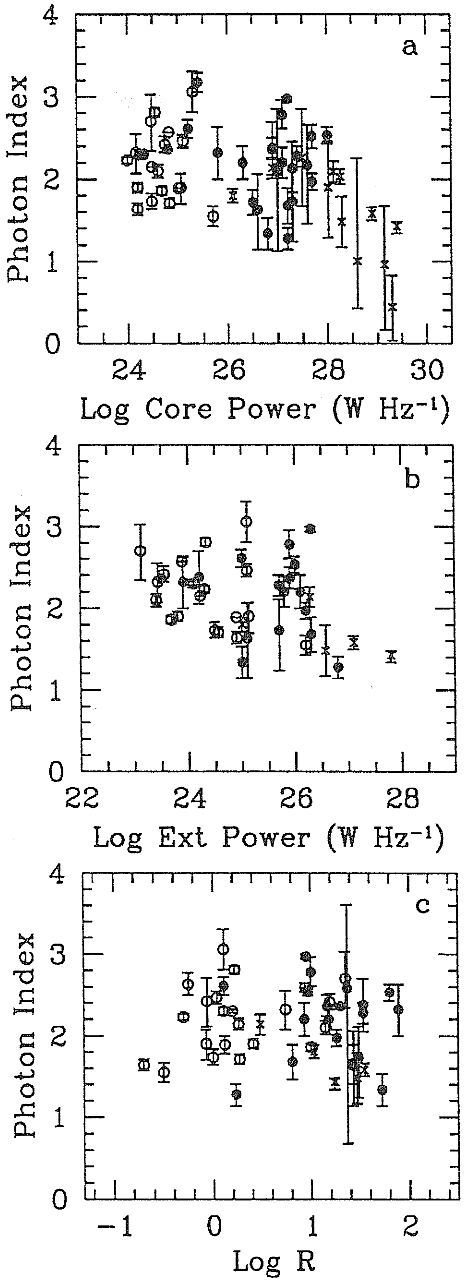

Figure 4.11: Rosat photon indices versus the radio core power (panel a), extended power (panel b), and the ratio of the core to extended flux, R, which is a beaming indicator (panel c). The radio data are from the VLA. Filled circles are RBLs, open circles are XBLs, crosses are FSRQs. The only correlation present is with the core power but it is introduced by the more distant objects. Note the continuous distribution of core radio power in panel (a).

The X-ray selected objects are ≈ 1.5 decades apart in F_{core} from the radio selected ones. The X-ray flux distribution is the same. In both cases the radio and the X-ray fluxes correlate, with a significance of $\sim 96\%$ for RBLs, 99.8% for FSRQs, and even stronger (99.99%) for XBLs (90% for EMSS, 79% for LASS). Note the radio-loud LASS object falling into the region of RBLs; this is 0521–365, a Blazar of uncertain classification, which has a visible radio jet (Macchetto et al. 1991), probably oriented at large ($\sim 30°$) viewing angles (Pian et al. 1994b). No correlations are present in the case of the extended radio flux (Figure 4.12b).

The most interesting aspect of Figure 4.12a is the fact that, both for radio-selected and X-ray selected BL Lacs, a correlation *is* present between the core radio and X-ray flux. Actually, it is stronger for XBLs than for RBLs (comparable if only the EMSS group is considered). This result clearly shows that the picture illustrated in Figure 4.10 is not entirely sufficient to account for the radio/X-ray emission of BL Lacs. We conclude that some intrinsic quantity, varying both in radio-selected and X-ray selected objects, should instead be leading the observed correlation of the radio and X-ray flux.

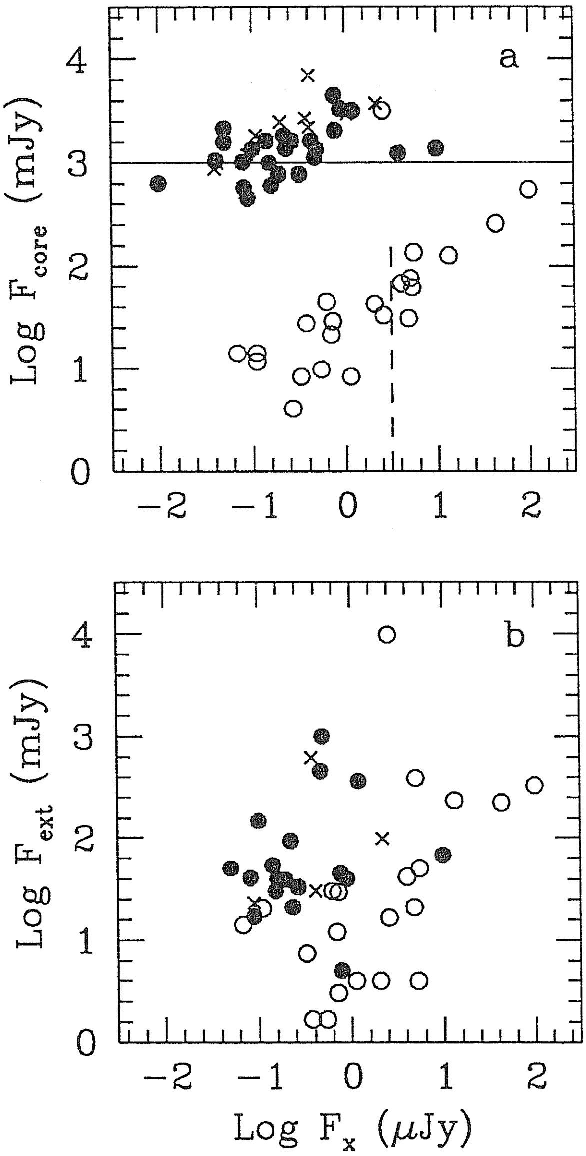

Figure 4.12: The Rosat flux density at 1 keV (abscissa) is compared to the VLA radio core (panel a) and extended (panel b) flux density. Filled circles are RBLs, open circles are XBLs, crosses are FSRQs. The horizontal line in panel (a) marks the limiting radio flux for the Stickel et al. (1991) sample and the vertical line separates the EMSS XBLs from the LASS XBLs. The open dot in the region of RBLs is 0521–365, a Blazar of uncertain classification. Contrary to what expected within the beaming model, the X-ray flux correlates with the radio core flux both for radio-selected and X-ray selected objects.

CHAPTER V

Implications of the Rosat Data for the Blazar Emission at Lower Frequencies

In this Chapter we examine the multifrequency distributions of RBLs, XBLs, and FSRQs, obtained using published data. We compare the two-band spectral index distributions for the three classes. Average radio to X-ray spectra for particular subgroups of RBLs are presented. A correlation analysis of the spectral parameters versus relevant quantities is performed, using independent methods. Besides the 1 Jy RBLs, only the complete, self-consistently defined samples of EMSS XBLs and the FSRQs sample from Brunner et al (1994) will be used.

5.1 Multifrequency Data for Blazars

One of the defining properties of Blazars is the large and rapid variability of the emission in all bands (e.g., Kollgaard 1994 and references therein). It is also known that the variability timescales depend on the frequency, roughly $\propto \nu^{-0.5}$ (e.g., Celotti, Maraschi, & Treves 1991). Therefore the first requirement for the study of the broad band energy distributions (BBEDs) of Blazars is the simultaneity of the measurements in different energy ranges. Because simultaneous multifrequency monitoring of relatively faint objects such as Blazars is difficult and expensive in terms of both telescope time and coordination between different groups, it is not surprising that intensive multifrequency campaigns with complete coverage of the electromagnetic spectrum were undertaken only for a few selected sources (e.g., Bregman et al. 1990; Kawai et al. 1991; Urry et al. 1993b; Maraschi et al. 1994b).

In the following we examine "mean" multifrequency spectra, obtained averaging all the fluxes available from the literature at a given frequency. This procedure provides a continuum representative of an intermediate brightness state, where the variability is taken into account by assigning the rms dispersion (or the excursion between the maximum and minimum flux) to each average flux as estimate of the error. This procedure clearly depends heavily on the number of observations published for each objects at each frequency, so that for well studied sources the rms is well determined and large, contrary to fainter or recently discovered sources, for which the rms is poorly sampled.

Several RBLs of the 1 Jy sample are well known sources, and a large body of observational material is available from the literature. Occasionally, simultaneous observations from the radio to the X-rays were acquired for the brightest objects (Bregman et al. 1990; Kawai et al. 1991), with the data at the X-ray frequencies obtained with the Exosat, IPC, and GINGA satellites. In order to characterize the average radio to X-ray spectrum, all the literature in the period 1900 – 1994 was searched for published fluxes at selected frequencies, based on the references provided by the electronic database NED.[1] For completeness, we performed this search for all the 34 sources of the sample, also including the objects for which Rosat data are not presently available. All the published systematic compilations of fluxes, as well as observations of single sources, were

---

[1] The NASA/IPC Extragalactic Database (NED), which is operated by the Jet Propulasion Laboratory, California Institute of Technology, under contract with the National Aeronautics and Space Administration.

carefully examined in order to have the maximum collection of information.

For each spectral range from radio to X-rays we selected one representative frequency, chosen with the criterion to have the maximum number of observations for the majority of the sources. This criterion yielded ν=5 GHz for the radio, $\nu = 1.36 \times 10^{14}$ Hz (K band) for the IR, $\nu = 5.45 \times 10^{14}$ Hz (V band) for the optical. Table 5.1a summarizes the radio, IR, and optical data, listing the average flux densities, the rms dispersions, the maximum and minimum flux, and the number of observations used. The largest variations of the flux are those in the optical band.[2]

Data at the higher energies are relatively less abundant (Table 5.1b). For the UV, the compilations of Edelson et al. (1992) and Pian & Treves (1993) are the basic references used. Fourteen RBLs have at least one observation in one of the two IUE cameras.

At X-ray frequencies, we selected all published flux densities at 1 keV. Although we are mainly interested in the Rosat measurements, we also collected the data provided by the previous missions. The main references are Della Ceca et al. (1990), Worrall & Wilkes (1990), Biermann et al. (1992), and Sambruna et al. (1994b).

Although firm detections in γ-rays are limited to only two objects of the RBL sample (0537–441 and 0716+714), while for 2005–489 there is a marginal detection, the flux densities or 2σ upper limits at 100 MeV, available from the GRO database, are also reported in Table 5.1b.

For the EMSS XBLs, radio and optical data are available from Wolter et al. (1994), who summarize measurements obtained in earlier publications (Morris et al. 1991; Stocke et al. 1991). In X-rays, the Rosat flux densities at

---

[2] A full compilation of individual flux measurements and corresponding references is available from the author.

Table 5.3: Average Composite Indices

	N	$\langle\alpha_{rx}\rangle \pm \sigma$	$\langle\alpha_{ro}\rangle \pm \sigma$	$\langle\alpha_{ox}\rangle \pm \sigma$	$\langle\alpha_{ox} - \alpha_x\rangle \pm \sigma$
A. Complete Samples					
FSRQs	8	0.87 ± 0.06	0.70 ± 0.13	1.44 ± 0.25	0.99 ± 0.56
RBLs	28	0.88 ± 0.08	0.63 ± 0.13	1.35 ± 0.18	0.15 ± 0.46
XBLs	21	0.58 ± 0.06	0.39 ± 0.07	0.94 ± 0.15	–0.31 ± 0.33
B. RBL Subgroups					
Quasar-like	8	0.91 ± 0.05	0.68 ± 0.10	1.35 ± 0.20	0.72 ± 0.15
RBL-like	18	0.88 ± 0.08	0.63 ± 0.13	1.37 ± 0.18	0.00 ± 0.21
XBL-like	2	0.74 ± 0.03	0.46 ± 0.05	1.26 ± 0.01	-0.83 ± 0.11

1 keV were used from Perlman et al. (1994). Brunner et al. (1994) studied the BBEDs of the 8 FSRQs of their complete sample, quoting the flux densities at 5 GHz and 1 keV, and the magnitudes in the *V* band. These values were used to compute the composite spectral indices for the FSRQs class.

In the next Section we derive the two-bands spectral indices of the three classes, using the data described above.

Table 5.1: Multifrequency Observations of RBLs
A. Radio, Infrared, and Optical Data

Source	Radio: $\nu = 5 \times 10^9$ Hz			IR: $\nu = 1.36 \times 10^{14}$ Hz			OPT: $\nu = 5.45 \times 10^{14}$ Hz		
	$\langle F_\nu \rangle \pm \sigma$	F_{max}, F_{min}	N	$\langle F_\nu \rangle \pm \sigma$	F_{max}, F_{min}	N	$\langle F_\nu \rangle \pm \sigma$	F_{max}, F_{min}	N
	(Jy)	(Jy)		(mJy)	(mJy)		(mJy)	(mJy)	
0048–097	1.109 ± 0.583	0.77, 1.98	4	6.962 ± 2.942	0.04, 13.97	25	2.365 ± 1.510	0.41, 6.08	32
0118–272	1.145 ± 0.106	1.07, 1.22	2	7.994 ± 1.518	6.41, 11.48	14	1.929 ± 0.360	1.35, 2.42	11
0138–097	1.735 ± 0.924	0.7, 2.66	4	3.248 ± 1.158	1.26, 5.13	11	0.631 ± 0.305	0.21, 1.12	15
0235+164	1.814 ± 0.542	0.7, 2.87	26	20.359 ± 19.142	2.48, 112.42	86	1.481 ± 1.286	0.12, 6.60	51
0426–380	1.17	···	1	···	···	···	0.965	···	1
0454+844	1.410 ± 0.144	1.25, 1.60	4	···	···	···	0.603 ± 0.417	0.24, 0.96	4
0537–441	3.920 ± 0.168	3.69, 4.00	4	10.117 ± 6.166	3.09, 29.03	18	3.536 ± 3.189	0.50, 12.02	30
0716+714	0.821 ± 0.163	0.64, 1.06	7	11.075 ± 8.883	3.04, 19.356	4	2.42	···	1
0735+718	2.134 ± 0.498	1.45, 3.65	29	19.131 ± 9.083	5.23, 48.18	71	3.951 ± 2.673	0.62, 15.0	228
0814+425	1.856 ± 0.682	1.15, 3.29	7	2.835 ± 0.332	2.60, 3.07	2	0.189 ± 0.038	0.15, 0.24	4
0820+225	1.630 ± 0.028	1.61, 1.65	2	0.345 ± 0.035	0.32, 0.37	2	0.061	···	1
0823+033	1.155 ± 0.224	0.989, 1.47	4	4.595 ± 2.319	1.39, 7.09	5	0.521 ± 0.254	0.24, 0.87	6
0828+493	1.378 ± 0.211	1.03, 1.57	5	1.235 ± 0.346	0.99, 1.48	2	0.165 ± 0.149	0.04, 0.38	4
0851+202	3.099 ± 0.724	2.14, 5.0	27	19.561 ± 20.793	5.09, 133.20	271	7.854 ± 8.716	0.42, 49.65	573
0954+658	0.957 ± 0.403	0.59, 1.54	9	···	···	···	0.557 ± 0.288	0.24, 0.80	4
1144–379	1.615 ± 0.955	0.94, 2.29	2	2.783 ± 1.648	0.88, 3.76	3	0.593 ± 0.453	0.27, 1.27	5
1147+245	0.826 ± 0.138	0.664, 1.0	4	7.830 ± 2.114	4.27, 11.99	20	1.487 ± 0.384	0.96, 1.91	6
1308+326	2.257 ± 0.391	1.43, 2.84	21	9.781 ± 8.416	0.63, 35.88	28	2.20 ± 1.527	0.09, 5.20	34
1418+546	1.242 ± 0.407	0.70, 1.76	6	13.198 ± 4.768	1.33, 25.05	27	2.752 ± 0.818	1.20, 6.08	66
1514–241	2.065 ± 0.382	1.53, 2.56	8	25.857 ± 4.052	19.54, 36.54	16	4.627 ± 1.210	1.70, 7.17	67
1519–273	2.175 ± 0.247	2.0, 2.35	2	1.19	···	1	0.276 ± 0.187	0.09, 0.47	3
1538+149	1.510 ± 0.409	1.14, 2.33	13	2.343 ± 0.489	1.70, 3.10	10	0.325 ± 0.126	0.17, 0.51	25
1652+398	1.268 ± 0.099	1.08, 1.42	16	54.305 ± 81.290	14.42, 472.96	55	14.107, 3.713	9.31, 26.54	91

Table 5.1.A: *(continued)*

Source	Radio: ν = 5 $\times 10^9$ Hz			IR: ν = 1.36 $\times 10^{14}$ Hz			OPT: ν = 5.45 $\times 10^{14}$ Hz		
	$\langle F_\nu \rangle \pm \sigma$ (Jy)	F_{max}, F_{min} (Jy)	N	$\langle F_\nu \rangle \pm \sigma$ (mJy)	F_{max}, F_{min} (mJy)	N	$\langle F_\nu \rangle \pm \sigma$ (mJy)	F_{max}, F_{min} (mJy)	N
1749+096	1.445 ± 0.360	0.74, 1.94	15	5.600 ± 2.437	1.58, 9.33	14	0.943 ± 0.356	0.14, 1.70	19
1749+701	1.667 ± 0.393	0.58, 1.81	12	...	...	...	0.834 ± 0.169	0.61, 0.96	4
1803+784	2.789 ± 0.297	2.30, 3.38	10	6.70	...	1	0.789 ± 0.221	0.61, 1.06	4
1807+698	1.685 ± 0.288	1.24, 2.20	13	26.791 ± 4.660	19.60, 35.50	9	7.430 ± 2.099	4.40, 13.18	31
1823+568	1.446 ± 0.210	1.25, 1.67	5	3.865 ± 0.148	3.76, 3.97	2	0.167	...	1
2005–489	1.210 ± 0.028	1.19, 1.23	2	29.253 ± 3.111	26.06, 33.11	12	8.577 ± 3.193	2.91, 11.75	6
2007+777	1.723 ± 0.413	1.00, 2.23	9	...	...	...	0.834 ± 0.169	0.61, 0.96	4
2131–021	2.010 ± 0.156	1.90, 2.12	2	0.71	...	1	0.125 ± 0.027	0.09, 0.15	3
2200+420	3.507 ± 1.962	1.07, 9.37	31	38.826 ± 17.934	3.39, 103.20	68	7.036 ± 4.400	0.46, 29.10	714
2240–260	1.030	...	1	1.958 ± 1.134	0.76, 3.39	6	0.335 ± 0.092	0.27, 0.40	2
2254+074	0.562 ± 0.273	0.33, 1.16	7	4.503 ± 1.937	3.37, 8.77	7	0.677 ± 0.287	0.23, 1.13	20

Table 5.1: Multifrequency Observations of RBLs
B. Ultraviolet, X-ray, and γ-ray Data

Source	UV LW: $\nu = 1.07 \times 10^{15}$ Hz			UV SW: $\nu = 2.14 \times 10^{15}$ Hz			X-rays: $\nu = 5.45 \times 10^{14}$ Hz			γ-rays: $\nu = 2.42 \times 10^{22}$ Hz
	$\langle F_\nu \rangle \pm \sigma$ [a] (mJy)	F_{max}, F_{min} (mJy)	N	$\langle F_\nu \rangle \pm \sigma$[a] (mJy)	F_{max}, F_{min} (mJy)	N	$\langle F_\nu \rangle \pm \sigma$ [a] (μJy)	F_{max}, F_{min} (μJy)	N	2σ u.l. (10^{-10} Jy)
0048−097	1.35	⋯	1	0.433 ± 0.266	0.62, 0.24	2	0.483 ± 0.391	0.06, 0.84	3	< 0.60
0118−272	0.622	⋯	1	⋯	⋯	⋯	0.113 ± 0.081	0.0001, 0.19	4	< 0.33
0138−097	⋯	⋯	⋯	⋯	⋯	⋯	1.5	⋯	1	< 0.66
0235+164	0.238	⋯	1	⋯	⋯	⋯	0.440 ± 0.716	0.038, 1.51	4	4.362 ± 1.680 [b]
0426−380	⋯	⋯	⋯	⋯	⋯	⋯	0.105 ± 0.035	0.08, 0.13	2	< 0.40
0454+844	⋯	⋯	⋯	⋯	⋯	⋯	0.207 ± 0.265	0.017, 0.51	3	< 0.40
0537−441	0.927 ± 0.161	0.74, 1.03	3	⋯	⋯	⋯	0.352 ± 0.231	0.12, 0.79	7	1.62 ± 0.707 [b]
0716+714	⋯	⋯	⋯	0.140	⋯	1	1.506 ± 1.791	0.22 4.58	5	1.897 ± 0.941 [c]
0735+718	1.716 ± 0.956	0.74, 3.16	7	0.402 ± 0.264	0.15, 0.88	6	0.278 ± 0.145	0.07, 0.65	18	⋯
0814+425	⋯	⋯	⋯	⋯	⋯	⋯	0.820 ± 1.103	0.04, 1.60	2	< 0.33
0820+225	⋯	⋯	⋯	⋯	⋯	⋯	0.05	⋯	1	< 1.38
0823+033	⋯	⋯	⋯	⋯	⋯	⋯	0.270	⋯	1	< 1.5
0828+493	⋯	⋯	⋯	⋯	⋯	⋯	1.420 ± 1.950	0.04, 2.80	2	< 0.46
0851+202	2.291 ± 1.519	0.44, 5.42	21	0.956 ± 0.646	0.19, 2.31	25	1.239 ± 0.935	0.27, 4.16	20	< 1.26
0954+658	⋯	⋯	⋯	⋯	⋯	⋯	0.203 ± 0.038	0.17, 0.23	2	< 0.33
1144−379	⋯	⋯	⋯	⋯	⋯	⋯	0.430	⋯	1	< 1.0
1147+245	⋯	⋯	⋯	⋯	⋯	⋯	0.081 ± 0.023	0.05, 0.10	4	< 0.33
1308+326	0.473 ± 0.033	0.44, 0.50	3	0.236	⋯	1	0.137 ± 0.053	0.08, 0.28	11	< 0.66
1418+546	1.003 ± 0.434	0.70, 1.31	2	0.229 ± 0.111	0.10, 0.31	3	0.164 ± 0.034	0.13, 0.21	4	< 0.40
1514−241	1.024 ± 0.574	0.62, 1.43	2	⋯	⋯	⋯	0.398 ± 0.193	0.15, 0.62	5	< 5.3
1519−273	⋯	⋯	⋯	⋯	⋯	⋯	0.286 ± 0.204	0.14, 0.43	2	< 0.46
1538+149	0.44	⋯	1	⋯	⋯	⋯	0.191 ± 0.081	0.10, 0.28	4	< 0.53
1652+398	2.450 ± 0.110	2.36, 2.62	6	1.264 ± 0.104	1.09, 1.39	11	33.177 ± 31.236	1.69, 98.63	25	< 0.66

Table 5.1.B: *(continued)*

Source	UV LW: $\nu = 1.07 \times 10^{15}$ Hz			UV SW: $\nu = 2.14 \times 10^{15}$ Hz			X-rays: $\nu = 5.45 \times 10^{14}$ Hz			γ-rays: $\nu = 2.42 \times 10^{22}$ Hz
	$\langle F_\nu \rangle \pm \sigma$ [(a)]	F_{max}, F_{min}	N	$\langle F_\nu \rangle \pm \sigma$ [(a)]	F_{max}, F_{min}	N	$\langle F_\nu \rangle \pm \sigma$ [(a)]	F_{max}, F_{min}	N	2σ u.l.
	(mJy)	(mJy)		(mJy)	(mJy)		(μJy)	(μJy)		(10^{-10} Jy)
1749+096	...	...	...	...	...	...	0.337 ± 0.035	0.30, 0.37	3	< 0.93
1749+701	...	...	...	...	...	...	0.162 ± 0.058	0.10, 0.22	3	< 1.06
1803+784	...	...	...	...	...	...	0.153 ± 0.066	0.08, 0.26	8	< 0.73
1807+698	1.223 ± 0.225	1.05, 1.78	9	0.467 ± 0.148	0.37, 0.84	9	0.891 ± 0.821	0.36, 2.57	7	< 1.65
1823+568	...	...	...	...	...	...	0.425 ± 0.064	0.38, 0.47	2	< 1.58
2005-489	5.125 ± 1.302	3.13, 7.44	13	2.223 ± 0.650	1.25, 3.18	13	10.550 ± 13.509	2.02, 39.00	8	1.2 [(d)]
2007+777	...	...	...	...	...	...	1.035 ± 1.757	0.14, 3.67	4	< 1.06
2131-021	...	...	...	...	...	...	0.070 ± 0.028	0.05, 0.09	2	< 0.53
2200+420	0.379 ± 0.186	0.235, 0.845	9	...	...	...	0.824 ± 0.414	0.34, 1.35	6	< 0.66
2240-260	...	...	...	...	...	...	0.08	...	1	< 0.93
2254+074	...	...	...	...	...	...	0.089 ± 0.008	0.08, 0.097	3	< 0.60

Notes to Table 5.1B: a: Only for N $\geq$ 4; **b:** N=2; **c:** N=4; **d:** Marginal detection.

5.2 Composite Spectral Indices

Two-band or composite spectral indices are calculated in the standard way defined by, e.g., Ledden & O'Dell (1985), Stocke et al. (1985), Ghisellini et al. (1986):

$$\alpha_{12} = -\frac{\log(\frac{F_1}{F_2})}{\log(\frac{\nu_1}{\nu_2})}, \tag{5.1}$$

where F_1, F_2 are the average fluxes at frequencies ν_1, ν_2, respectively.

We are interested in the radio to optical (α_{ro}), radio to X-ray (α_{rx}), and optical to X-ray (α_{ox}) indices. Because little or no information is available in the IR for the EMSS XBLs, we will not consider a composite spectral index relative to this band. The indices for the three classes are reported in Table 5.2a-c. For the indices calculated with respect to the X-ray band only the flux densities at 1 keV determined with Rosat were used. This choice is motivated by the fact that for a large fraction of the objects of all three classes the Rosat observation represents the best (higher sensitivity) or even the only measurement of the flux density at 1 keV so far obtained.

The distributions of α_{rx}, α_{ro}, and α_{ox} for the three classes are plotted in Figure 5.1 - 5.3, and the average indices for the three classes are given in Table 5.3a.

In all cases, RBLs have steeper distributions than XBLs, but with some overlap. The mean values for these two classes are different at $> 99.99\%$ confidence level in all cases, and the distributions are significantly different (Table 5.4). A higher overlap is present between RBLs and FSRQs, whose α_{rx}, α_{ro}, α_{ox} distributions are consistent with their being drawn from the same parent one at

Table 5.4: KS Test Results [a]

α_{rx}		RBLs	XBLs	FSRQs
	RBLs	···	4×10^{-10}	0.87
	XBLs	···	···	2×10^{-5}

α_{ro}		RBLs	XBLs	FSRQs
	RBLs	···	2×10^{-7}	0.67
	XBLs	···	···	2.2×10^{-5}

α_{ox}		RBLs	XBLs	FSRQs
	RBLs	···	1.6×10^{-8}	0.74
	XBLs	···	···	2×10^{-4}

$\alpha_{ox} - \alpha_x$		RBLs	XBLs	FSRQs
	RBLs	···	2×10^{-3}	6×10^{-3}
	XBLs	···	···	2×10^{-5}

Notes to Table 5.4:

a = Probability that the two distributions are drawn from the same parent one

~ 87%, 67%, and 74%, respectively. The distributions for XBLs and FSRQs are well separated ($P_{KS} < 0.02\%$, Table 5.4), with XBLs, in all cases having flatter values of the composite indices.

Because it measures the rise of the continuum from radio to optical, as a first approximation α_{ro} can be considered an indicator of the position of the spectral cutoff. The flatter values of α_{ro} for XBLs with respect to RBLs and FSRQs indicate that in this class the continuum emission reaches maximum powers at higher frequencies than in the latter two classes. In the α_{ro}, α_{ox} or color-color diagram (Figure 5.5), as known from previous studies (Ledden & O'Dell 1985; Stocke et al. 1985; Giommi et al. 1994), the XBL and RBL populations occupy distinctive regions of the diagram. However, note in Figure 5.5 that a few RBLs make a "bridge" toward the XBLs, suggesting a continuity of properties among the two classes.

Another useful parameter is the difference of α_{ox} and the Rosat slope, α_x. The $\alpha_{ox} - \alpha_x$ index describes the spectral connection between the X-ray spectrum and the continuum at the lower frequencies; a value of $\alpha_{ox} - \alpha_x$ near zero indicates that the X-ray spectrum lies on the extrapolation of the optical slope, negative (positive) values are related to convex (concave) optical-to-X-ray continua. The values of $\alpha_{ox} - \alpha_x$ are given in Table 5.2a for the single objects and in Table 5.3a for the classes; the distributions are plotted in Figure 5.4. A neat separation is present between the three classes, as indicated by the KS test probability (Table 5.4). XBLs and FSRQs ($P_{KS} \sim 2 \times 10^{-3}$, Table 5.4) assume negative and positive values of $\alpha_{ox} - \alpha_x$, respectively, while the distribution for RBLs appears intermediate, assuming both positive and negative values.

The continuity among the three classes is better shown in Figure 5.6, where α_{ro} is plotted against $\alpha_{ox} - \alpha_x$. XBLs, RBLs, and FSRQs form a continuous sequence, with the objects having a steeper radio-to-optical index having also flatter X-ray spectra (see below).

We conclude that the BBEDs of the three Blazar classes are typically different, but with a smooth change of the spectral parameters. XBLs have the bulk of the emission at higher frequencies than FSRQs and RBLs. Going from XBLs to FSRQs, the X-ray spectrum becomes progressively flatter.

5.3 Average BBEDs for RBLs

The distributions of the composite indices discussed above show that there is a significant spread in the continuum properties of the 1 Jy RBLs, with

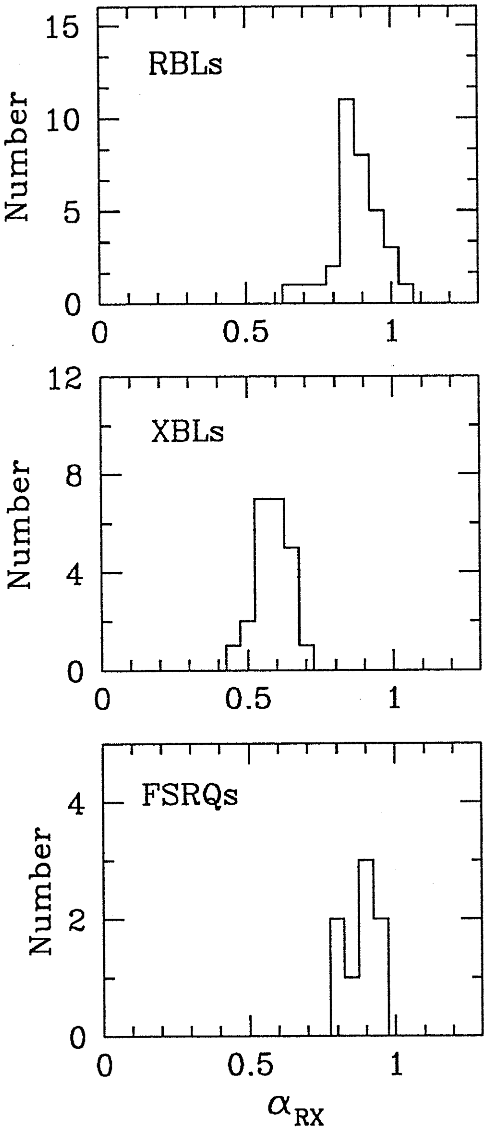

Figure 5.1: The distribution of the radio-to-X-ray spectral indices for the 1 Jy RBLs (top), the EMSS XBLs (middle), and the FSRQs of Brunner et al. (bottom). XBLs have flatter indices than RBLs and FSRQs. For RBLs versus FSRQs the KS test gives a probability of 87% that the two distributions are drawn from the same parent one.

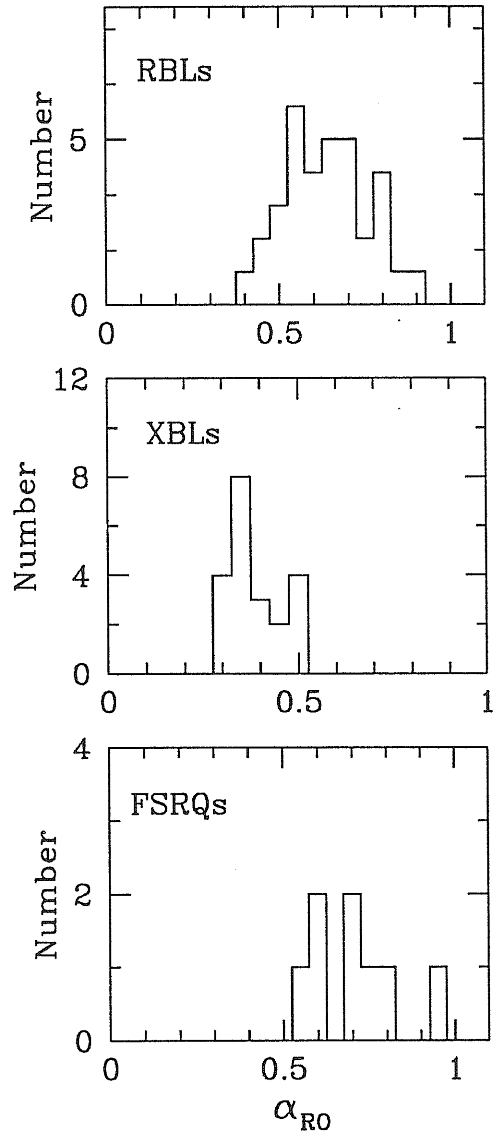

Figure 5.2: The distribution of the radio-to-optical spectral indices for RBLs (top), XBLs (middle), and FSRQs (bottom). XBLs have flatter indices than RBLs and FSRQs. For RBLs versus FSRQs the KS test gives a probability of 67% that the two distributions are drawn from the same parent one.

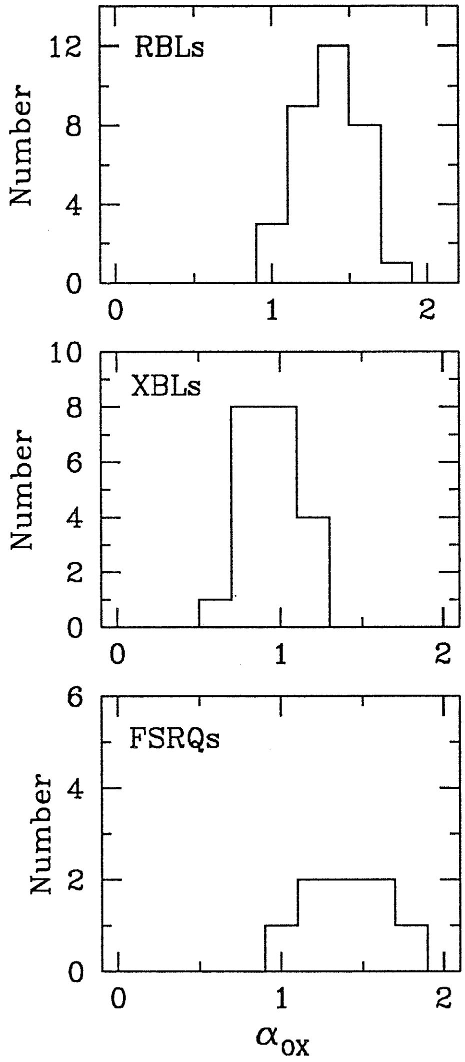

Figure 5.3: The distribution of the optical-to-X-ray spectral indices for RBLs (top), XBLs (middle), and FSRQs (bottom). XBLs have flatter indices than RBLs and FSRQs. For RBLs versus FSRQs the KS test gives a probability of 74% that the two distributions are drawn from the same parent one.

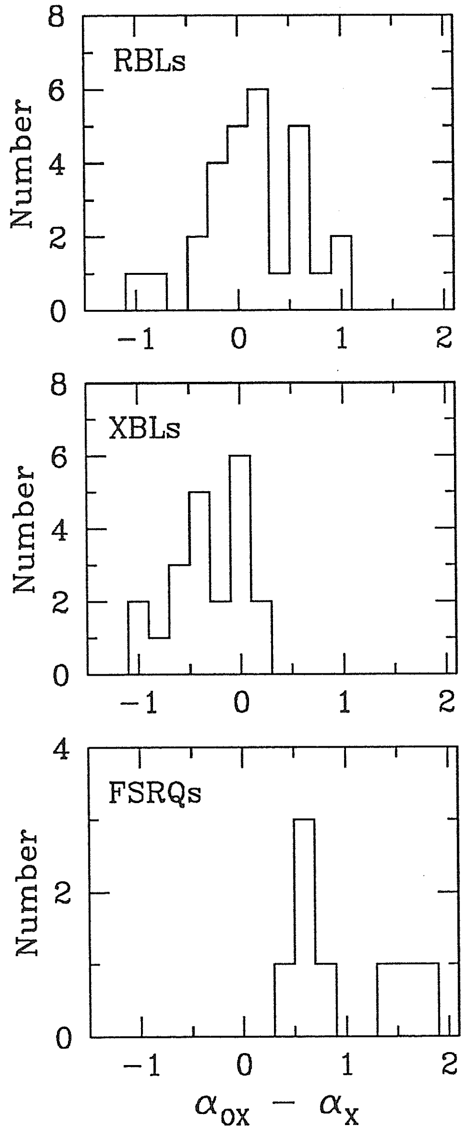

Figure 5.4: The distribution of the $\alpha_{ox} - \alpha_x$ spectral indices for RBLs (top), XBLs (middle), and FSRQs (bottom). XBLs assume negative values, indicating convex optical-to-X-ray continua. FSRQs have positive indices (concave optical-to-X-ray spectra). For RBLs both situations are present, with significant overlap with both XBLs and FSRQs.

some objects having broad band spectra close to those of FSRQs, and others more resembling the XBLs. This is particularly clear for the distributions of the $\alpha_{ox} - \alpha_x$ indices (Figure 5.4).

From Figure 5.4 we can define three subgroups of RBLs. The first, corresponding to $\alpha_{ox} - \alpha_x \gtrsim 0.5$ and including 8 objects, will be called "quasar-like"; a small group of 2 objects with $\alpha_{ox} - \alpha_x \lesssim -0.5$ will be the "XBL-like" group; and the remaining "RBL-like" group will consist of the sources with $\alpha_{ox} - \alpha_x$ between –0.5 and 0.5. The latter includes the majority of RBLs (18 objects).

Clearly the inhomogeneity in the $\alpha_{ox} - \alpha_x$ distribution reflects the inhomogeneity present in the Rosat slope distribution discussed in Chapter 4. It is thus not surprising that in the quasar-like and XBL-like subgroups we find several sources which formed the steep and flat tails in Figure 4.1b. Note that 1652+398, which is a well known X-ray–loud object, does not have a Rosat spectrum typical of the XBL-like subgroup; here this source falls among the RBL-like objects.

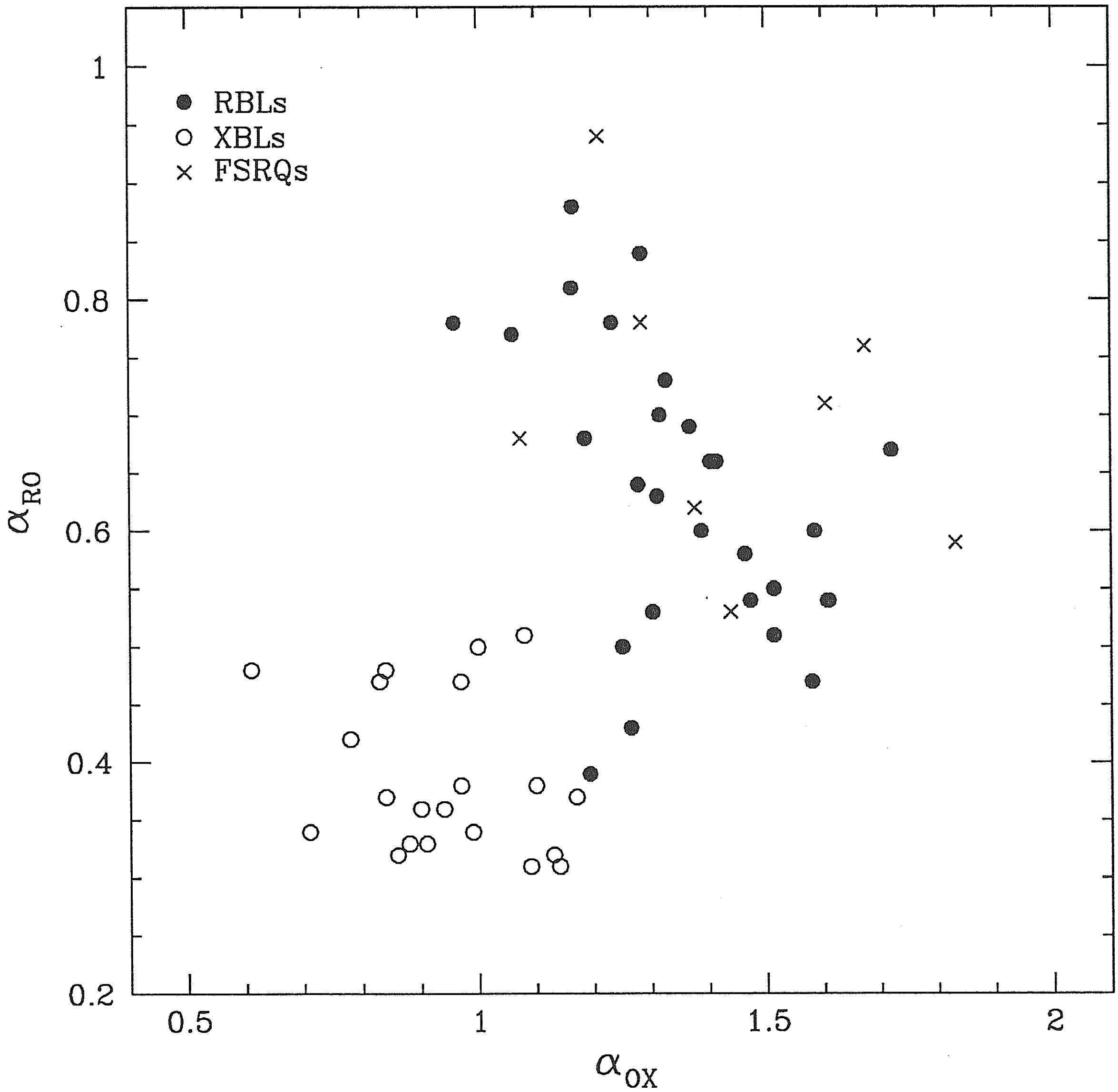

Figure 5.5: In the α_{ro}, α_{ox} diagram, radio-selected and X-ray selected Blazars occupy distinctive regions. Filled circles are RBLs and open ones are XBLs; crosses are FSRQs. A few RBLs form a "bridge" toward XBLs.

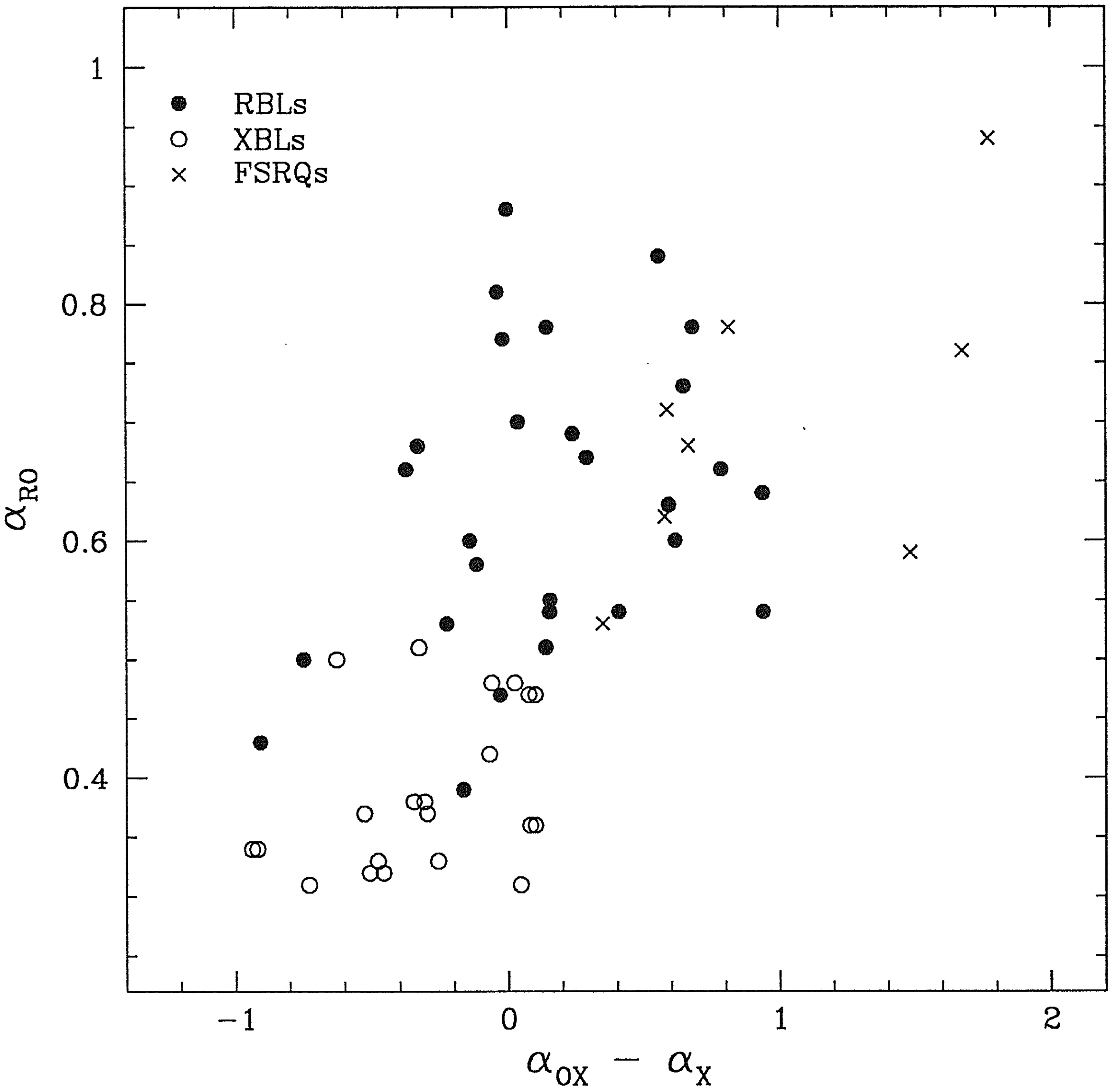

Figure 5.6: The radio-to-optical index is plotted versus the $\alpha_{ox} - \alpha_x$ one. Symbols as in Figure 5.5. XBLs, RBLs, and FSRQs occupy different regions but form a continuous distribution. Objects with a steeper value of α_{ro} have also flatter X-ray continua, with a highly significant trend (99.9%).

Table 5.2: **Composite Spectral Indices**

Source	α_{rx}	α_{ro}	α_{ox}	$\alpha_{ox} - \alpha_x$
A. RBLs				
0048–097	0.79	0.53	1.30	–0.23
0118–272	0.88	0.55	1.51	0.15
0426–380	0.93	0.81	1.16	–0.04
0454+844	1.03	0.67	1.72	0.29
0537–441	0.87	0.60	1.39	–0.14
0716+714	0.76	0.50	1.25	–0.75
0735+178	0.91	0.54	1.61	0.41
0814+425	0.99	0.79	1.39	...
0820+225	0.98	0.88	1.17	0.00
0828+493	0.94	0.78	1.23	0.14
0851+202	0.86	0.51	1.51	0.14
0954+658	0.86	0.51	1.28	0.94
1144–379	0.86	0.68	1.18	–0.33
1147+245	0.91	0.54	1.61	0.94
1308+326	0.94	0.60	1.58	0.61
1519–273	0.87	0.77	1.06	–0.02
1538+149	0.93	0.73	1.33	0.65
1652+398	0.66	0.39	1.19	–0.17
1749+096	0.87	0.63	1.31	0.59
1749+701	0.91	0.66	1.40	–0.37
1803+784	0.92	0.70	1.32	0.04
1807+698	0.85	0.47	1.58	–0.03
1823+568	0.84	0.78	0.96	0.68
2005–489	0.72	0.43	1.26	–0.91
2007+777	0.92	0.66	1.41	0.78
2131–021	0.98	0.84	1.28	0.55
2200+420	0.86	0.54	1.47	0.15
2240–260	0.93	0.69	1.37	0.24
2254+074	0.88	0.58	1.46	–0.12

Table 5.2: *(continued)*

Source	α_{rx}	α_{ro}	α_{ox}	$\alpha_{ox} - \alpha_x$
B. XBLs				
0122+090	0.59	0.31	1.15	0.05
0158+001	0.52	0.33	0.88	–0.26
0205+350	0.47	0.34	0.71	–0.94
0257+342	0.64	0.37	1.17	–0.53
0317+183	0.58	0.38	0.97	–0.35
0419+194	0.53	0.48	0.61	0.02
0607+710	0.71	0.51	1.08	–0.34
0922+745	0.54	0.36	0.90	0.10
0950+492	0.53	0.33	0.91	–0.48
1207+394	0.53	0.37	0.84	–0.30
1221+245	0.63	0.38	1.10	–0.31
1229+643	0.56	0.36	0.94	0.08
1402+041	0.58	0.31	1.09	–0.73
1407+595	0.67	0.50	1.00	–0.63
1443+634	0.59	0.47	0.83	0.10
1458+224	0.60	0.32	1.13	–0.46
1534+014	0.61	0.48	0.84	–0.06
1552+202	0.54	0.42	0.78	0.07
1757+703	0.51	0.32	0.87	–0.51
2143+070	0.64	0.47	0.97	0.07
C. FSRQs				
0016+731	0.93	0.76	1.67	1.67
0153+744	0.89	0.59	1.83	1.48
0212+735	0.90	0.94	1.21	1.77
0615+820	0.94	0.71	1.60	0.58
0836+710	0.78	0.68	1.07	0.66
1039+811	0.82	0.53	1.44	0.35
1150+812	0.89	0.78	1.28	0.81
1928+738	0.83	0.62	1.38	0.58

The composite indices of the three RBL subgroups are reported in Table 5.3b. Note the similarity of the composite indices of each subgroup and the "corresponding" complete sample in Table 5.3a.

We derived the average BBEDs representative of the whole sample and of each subgroup, in the following way. At each given fiducial frequency ν (see the previous Section), for the *i-th* object we take the average logarithmic flux, $\mathrm{f}_i^{\,\nu} = \langle log(\nu F_\nu)_i \rangle$. For each subgroup, we define the normalization factor $\mathrm{A}_x = \langle f_i^x \rangle_{group}$. Then, we take the average of the normalized individual fluxes, $\mathrm{F}^\nu_{group} = \langle \frac{f_i^\nu}{A_x} \rangle_{group}$, assigning the corresponding rms deviation as uncertainty.

The derived average BBED for the whole 1 Jy sample is shown in Figure 5.7a. The extremes of the error bars have been joined to show the range of the spectral variations. The total average Rosat slope, $\alpha_x = 1.20$, and the slopes corresponding to its standard deviation, $\pm$ 0.46 (1 σ), are shown. This average BBED splits into the average BBEDs of the quasar-like, RBL-like, and XBL-like subgroup (panels b, c, d).

The quasar-like and RBL-like objects have BBEDs peaking in the IR-Optical portions of the spectrum, while the steepness of the X-rays indicates that the 2 XBL-like sources peak at $\approx 10^{16}$ Hz. The transition from quasar-like to XBL-like objects also correspond to a progressive steepening of the X-ray spectrum, whose average slope goes from 0.63 ± 0.22 for quasar-like, to 1.36 ± 0.20 for RBL-like, to 2.11 ± 0.15 for XBL-like sources. A quantitative modelling of the continua for the three subgroups will be done in Chapter 6. Here we stress that the spread of the BBED shape of RBLs reflects, as discussed above, a continuity of spectral properties within the Blazar class.

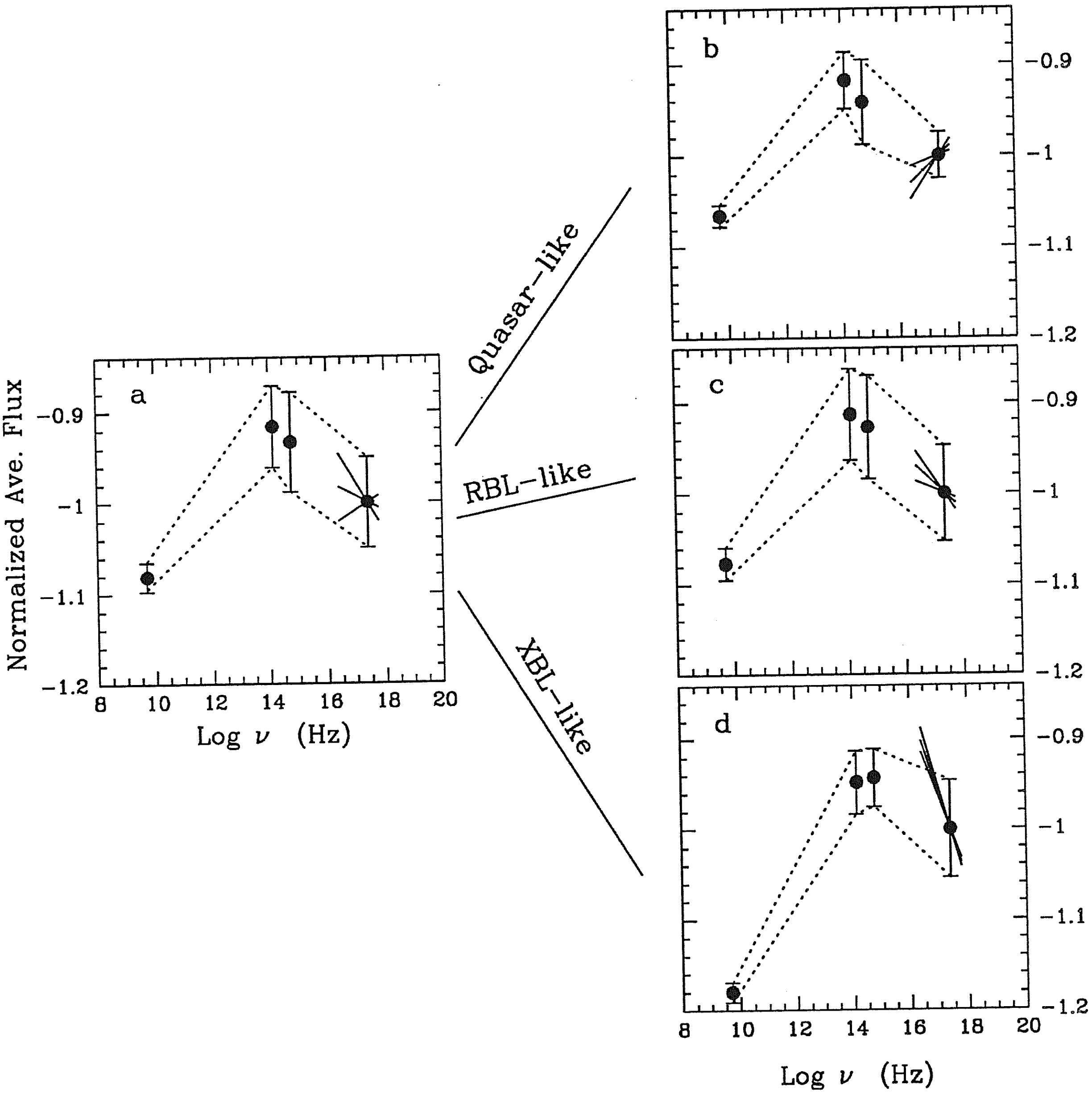

Figure 5.7: Average broad-band energy distributions for the whole RBL sample (panel a) and for the subgroups of quasar-like, RBL-like, and XBL-like objects (panels b, c, d). The spectra are normalized to the total average X-ray flux of the corresponding group. Quasar-like and RBL-like objects have spectra peaking at lower energies than the XBL-like group. The X-ray spectral slopes steepen going from the quasar-like to the XBL-like panel.

5.4 Multifrequency Continua of Blazars: Fundamental Parameters

A natural question is raised by the above results. Is there a fundamental parameter leading the spectral continuity observed within Blazars?

A first indication can be offered by considering that the three classes have different distributions in redshift and total luminosity, with FSRQs being at higher distance/luminosities than BL Lacs. Theoretical considerations also indicate the total luminosity as a primary parameter (Maraschi et al. 1994a), responsible in particular for positioning the spectral cutoff in the spectra. In this hypothesis we would expect to see a correlation between the spectral indices and the bolometric luminosity of the objects. This parameter will thus be considered. We will also consider the redshift, a primary correlation with this parameter meaning that cosmological effects may be important.

A proper way to calculate the bolometric luminosity would be by interpolating a second order polynomial to each multifrequency spectra (e.g., Landau et al. 1986). This procedure however requires a better data coverage for all the objects than a few fiducial fluxes, in order to constrain the free parameters of the parabola. While this work is in progress, it can be noted that, as the emission is dominated by the output at the peak frequency, a good first order approximation of the bolometric luminosity is given by the the peak luminosity, L_p, i.e., the luminosity measured at the peak frequency. For the RBLs, the values of L_p can be derived from Tables 5.1a-b, selecting the maximum value of the flux of a given source among those reported. In all cases, data in the IR or optical bands were selected. The same procedure applied to XBLs and FSRQs yielded luminosities in X-rays and IR, respectively.

The parameters to be compared for possible correlations are the three independent spectral indices, α_{ro}, α_{ox}, and α_x (or their combinations, α_{rx} and $\alpha_{ox} - \alpha_x$), L_p, and z. Our goal is to determine the primary correlation(s) among these variables. We used two independent statistical tests, the Principal Component Analysis (PCA) and the partial correlation analysis.

a) Principal Component Analysis

This method, which is largely applied in Astronomy (e.g., Whitmore 1984; Boroson & Green 1992), is intended for large samples and for homogeneous datasets. The description of the method and the numerical code used here is given by Murtagh & Heck (1987).

The basic idea of the PCA is the following. Suppose we have, in an N-dimensional space, a distribution of datapoints (a "cloud"), and to want to determine the principal directions along which this cloud is extended. If each axis represents a meaningful parameter of the system, the problem is equivalent to finding which parameter is more important in the description of the cloud. Through a rotation of the axes of the parameter space, the PCA finds the new directions from where the distance of the points is minimum (or, equivalently, their variance is maximum).

In practice, the PCA works on the matrix of the two-point correlation coefficients, finding its eigenvalues and eigenvectors. The first eigenvalue corresponds to the "best-fit" axis, i.e., it identifies the direction along which the cloud is more stretched. The associated eigenvalue is the total variance, i.e., the sum of the projections of the parameters on the best-fit axis; it gives a quantitative measure of the elongation of the cloud along it. The remaining eigenvectors and eigenvalues are associated to the second, third, etc. best directions. The components of the eigenvectors represent the projections of the parameters along the best-fit, second best, etc. directions, and are thus the measure of the "importance" of the parameter in determining that direction.

We applied the PCA to the space of our parameters for the three joint Blazar samples (57 objects) and to the RBLs alone (28 objects), trying different combinations of the independent variables. In all cases, we reached the same conclusions, and we chose to report in Table 5.5 the results obtained for the N = 5 (α_{ro}, α_{ox}, α_x, L$_p$, z) parameter space. We report the derived eigenvalues, in order of decreasing variance. We consider only the first two eigenvectors (corresponding to variance of 55% and 20% respectively). The best-fit direction (eigenvector 1) is principally contributed to by z (54%), L$_p$ (51%), α_{ro} (46%), and α_x (42%); the second best direction (eigenvector 2) is principally determined by α_{ox} (85%).

In conclusion, the PCA confirms that a good choice of "fundamental" parameters is given by (α_{ro}, α_{ox}, α_x, L$_p$, z). It indicates that the principally related parameters are α_{ro} with both L$_p$ and z, with a trend of increasing α_{ro} for increasing distances/luminosities.

However, when dealing with flux limited samples, it is necessary to take into account possible spurious correlations induced by obvious dependences, in this case of the luminosity on the redshift. The PCA is not capable of distinguishing genuine from spurious correlations. The proper way to handle this is to use a partial correlation analysis.

b) Partial Correlation Analysis

This method (e.g., Padovani 1992b) consists of calculating the partial correlation coefficient $r_{12,34}$ associated to the probability that parameters 1 and 2 are correlated excluding the effects of their correlations with parameters 3 and

Table 5.5: PCA Results

	Eig.1 (54.9%)	Eig.2 (20.4%)	Eig.3 (11.3%)	Eig.4 (9.7%)	Eig.5 (3.8%)
$\alpha_{\rm X}$	0.4230	0.4933	0.1982	0.6813	0.2725
$\alpha_{\rm OX}$	–0.2349	0.8519	–0.1579	–0.4391	0.0352
$L_{\rm P}$	–0.5120	0.1381	0.5104	0.3101	–0.6018
$\alpha_{\rm RO}$	–0.4574	–0.0075	–0.7374	0.4967	0.0180
z	–0.5427	–0.1083	0.3628	0.0100	0.7497

4. This coefficient is a combination of the two-point correlation coefficient τ_{12} (Padovani 1992b).

We performed the partial correlation analysis for the N=4 set of parameters given by α_{ro}, $\alpha_{ox} - \alpha_x$, L_p, z. We first checked the RBLs alone (28 objects) and the three joint samples (57 sources). The two-point correlation matrices are reported in Table 5.6a (RBLs) and 5.6b (RBLs + XBLs + FSRQs), while the $\tau_{12,34}$ and corresponding probabilities are given in Table 5.6c. The threshold for a significant and a marginally significant correlation are fixed at 95% and 90%, respectively.

From Table 5.6c it appears that the strongest correlations for RBLs are between $\alpha_{ox} - \alpha_x$ and α_{ro} ($\sim$ 97%), α_{ro} and L_p (99.98%), and α_{ro} and z (>99.99%). When XBLs and FSRQs are added, only the first correlation survives, with increased significance (99.9%). The correlation probability of α_{ro} and the redshift drops to a marginally significant value ($\sim$ 92%).

The trend obtained for α_{ro} versus $\alpha_{ox} - \alpha_x$ (Figure 5.6), is for objects with higher radio-to-optical indices also having flatter X-ray spectra. If we interpret the emission from radio to optical as due to synchrotron, and the emission at higher energies as related to a Self-Compton component, the correlation in the Figure means that when the synchrotron peak migrates to lower energies, giving steeper α_{ro} values, the Compton component becomes more and more important in X-rays. This would imply that the balance between the physical parameters accounting for the two emission mechanisms changes in a systematic way along the sequence XBLs/RBLs/FSRQs, or that Blazars are dominated in their continuum emission by the same mechanism operating on different physical scales.

From the α_{ro} versus z plot (Figure 5.8a), there is a hint that the backward shift of the synchrotron peak is related to the distance of the objects, the more distant sources having the bulk of the emission at lower frequencies compared to the more nearby sources. However, the correlation is clearly dominated by RBLs (Figure 5.8a). When this class is considered alone there is also a strong correlation of α_{ro} with the peak luminosity, as shown in Figure 5.8b, where XBLs and FSRQs have also been added for comparison.

In conclusion, the correlation analysis shows that, when the three Blazar samples are considered together, the strongest correlation is between the spectral parameters describing the shape of the X-ray continuum and the position of the energy cutoff. A second, weaker correlation is present between α_{ro} and the redshift; however, this correlation is introduced by the RBL class alone, for which α_{ro} is also strongly correlated with the peak luminosity. On the basis of

Table 5.6: Correlation matrix
A. RBLs

	$\alpha_{ox} - \alpha_x$	α_{ro}	L_p	z
$\alpha_{ox} - \alpha_x$	1.0000	0.3457	- 0.0073	0.0716
α_{ro}	...	1.0000	0.1497	0.6783
L_p	...	...	1.0000	0.7226
z	...	...	...	1.0000

Correlation matrix
B. XBLs + RBLs + FSRQs

	$\alpha_{ox} - \alpha_x$	α_{ro}	L_p	z
$\alpha_{ox} - \alpha_x$	1.0000	0.6617	0.5164	0.4953
α_{ro}	...	1.0000	0.6103	0.6290
L_p	...	...	1.0000	0.8033
z	...	...	...	1.0000

C. Partial Correlation Analysis

		RBLs		XBLs+RBLs+FSRQs	
Var. 1	Var. 2	$r_{12,34}$	P_S (%)	$r_{12,34}$	P_S (%)
$\alpha_{ox} - \alpha_x$	L_p	0.2744	79.49	0.1337	65.54
$\alpha_{ox} - \alpha_x$	α_{ro}	0.4707	97.66	0.4921	99.98
$\alpha_{ox} - \alpha_x$	z	- 0.3513	89.97	0.0094	5.25
α_{ro}	L_p	- 0.6979	99.98	0.1300	64.17
α_{ro}	z	0.8544	>99.99	0.2513	92.77

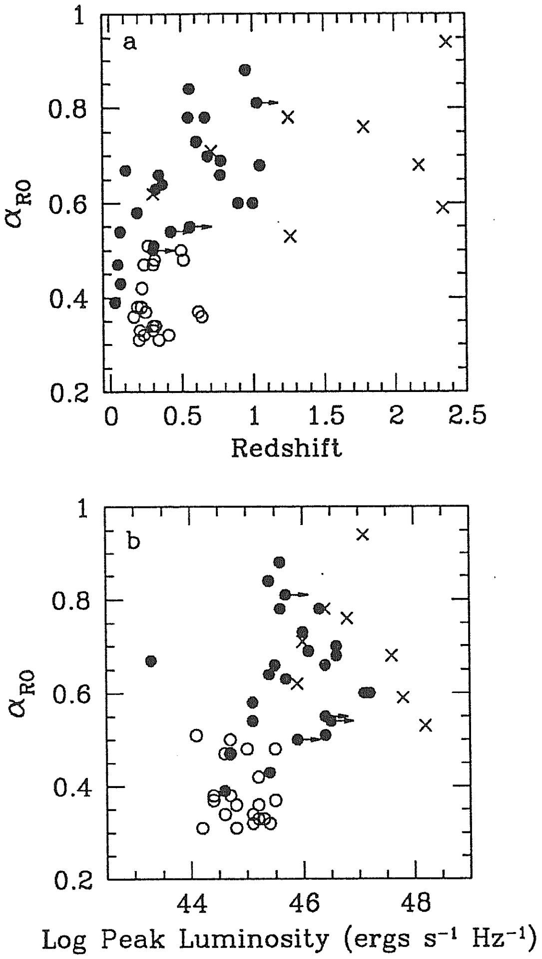

Figure 5.8: In both panels, RBLs are depicted as filled circles, XBLs as open circles, and FSRQs as crosses. *Panel a:* The radio-to-optical spectral index correlates (92%) with the redshift, and increases with increasing distance. The trend is dominated by RBLs, for which the correlation is highly significant ($>$ 99.99%). *Panel b:* α_{ro} correlates with the peak luminosity for RBLs alone, with high significance (99.9%). The trend is no longer significant (64%) when XBLs and FSRQs are added.

the present data, it is not clear whether redshift or luminosity is the dominant parameter. In order to disentangle the two, a larger sample of increased statistics at the higher distances/luminosities would be necessary.

CHAPTER VI

Modelling the Continuum Emission from Blazars

The observational scenario presented so far indicates that, from the point of view of their continuum emission, Blazars appear to be a single class of objects with properties smoothly changing along the sequence XBLs/RBLs/FSRQs. The present data suggest that one or only a few physical quantities are leading the continuous transition, that is, Blazars are all dominated by the same emission mechanism but with different values of the physical parameters.

The aim of this Chapter is to address the question of which physical quantity(ies) is responsible for the "appearance" of a Blazar like an XBL, or RBL, or an FSRQ. We pursue the answer by applying current theoretical models to our data.

Simple, homogeneous Synchrotron-Self Compton (SSC) models have been used extensively in the literature to compare the radio and X-ray fluxes of Blazars; in Section 6.1 they are reconsidered in a new perspective. Section 6.2 deals with more complex, inhomogeneous jet models, which have already proven to be successful to in interpreting the radio to X-ray spectral distributions of Blazars. Final remarks concern the spectral variability of Blazars, briefly addressed in Section 6.3.

6.1 Homogeneous Synchrotron-Self Compton Models

The basic theory of the SSC emission was developed by Ginzburg & Syrovatskii (1965), Jones, O'Dell, & Stein (1974), Tucker (1975), Gould (1979), and Marscher (1980). In all cases, a population of relativistic electrons uniformly filling a given volume (sphere or slab) radiates isotropically as they are accelerated in a magnetic field, i.e., via the synchrotron mechanism, and they Compton-scatter the synchrotron photons to higher energies (the "Self-Compton" component). Assuming relativistic motion of the emitting plasma, with a bulk Lorentz factor Γ_B, the flux received by an observer at an angle ϑ from the direction of the motion is $F_m = F_{rest} \times \delta^n$, where $\delta = [\Gamma_B - (\Gamma_B^2 - 1)^{0.5} cos\vartheta]^{-1}$ is the Doppler beaming factor, and the index n depends on the assumed geometry and on the spectral index of the thin synchrotron emission, α.

In an unpublished work, Urry (1984) showed that published calculations of synchrotron and Self-Compton fluxes varied by several orders of magnitudes. In the following, we adopt the formalism of Jones, O'Dell, & Stein (1974) for a slab geometry, using the convenient formulae given in Urry (1984).

A lower limit on the beaming factor can be derived by requiring that the predicted SC flux, typically emitted at X-ray frequencies, should not exceed the observed one. The inferred lower limit for δ depends on the synchrotron flux, F_m and the SC flux, F_x (Jy), the angular size, θ_d (mas), and the redshift, z, through

$$\delta = K_\alpha\ (1+z)\ F_m\ [\frac{\ln(\nu_b/\nu_m)}{F_x\ \theta_d^{6+4\alpha}\ \nu_x^\alpha\ \nu_m^{5+3\alpha}}]^{1/(4+2\alpha)}, \qquad (6.1)$$

where ν_m and ν_b are the self-absorption and break frequencies, respectively, in

[GHz], and ν_x is the SC frequency in [keV]. The constant K_α is given by the following expression:

$$\mathrm{K}_\alpha = (4.14 \times 10^{-6})^{\frac{1}{2\alpha+4}} \; (3.66 \times 10^{-4})^{\frac{\alpha}{2\alpha+4}} \; \mathrm{e}_\alpha{}^{\frac{1}{2\alpha+4}} \; \mathrm{i}_\alpha{}^{-\frac{\alpha+1}{\alpha+2}}, \tag{6.2}$$

where e_α and i_α are functions of α tabulated in Urry (1984).

The magnetic field [Gauss] is related to the self-absorption turnover of the synchrotron spectrum:

$$\mathrm{B} = \mathrm{A}_\alpha \; \theta_\mathrm{d}^4 \; \nu_\mathrm{m} \mathrm{F}_\mathrm{m}^{-2} \; \frac{\delta}{(1+\mathrm{z})}, \tag{6.3}$$

and $\mathrm{A}_\alpha = 4.04 \times 10^{-3} i_\alpha^2$ (Urry 1984). We choose $\alpha = 0.75$, as a typical value for these sources, with the above functions becoming $\mathrm{K}_{0.75} = 9.33 \times 10^{-2}$ and $\mathrm{A}_{0.75} = 1.81 \times 10^{-4}$. For different choices of α, for example $\alpha = 0.5$ and $\alpha = 1.0$, the functions become $\mathrm{K}_{0.5} = 7.44 \times 10^2$ and $\mathrm{K}_{1.0} = 0.1105$, with a maximum change of a factor ~ 1.5, and $\mathrm{A}_{0.5} = 3.26 \times 10^{-4}$ and $\mathrm{A}_{1.0} = 1.12 \times 10^{-4}$ changing by a factor 3.

Our goal is to understand the trend of the radio versus the X-ray flux observed in Figure 4.12a. Specifically, we want to see if the separation of RBLs and XBLs in this diagram, and the correlation of the radio and X-ray fluxes within the single classes, can be interpreted in terms of varying beaming factors, or, as argued in Section 4.4.2, whether these can be effects of the variations of intrinsic parameters, such as, for example, the magnetic field and/or the angular size. In fact, from the equations (6.1) and (6.3) above, one derives the basic dependences of the synchrotron and SC fluxes:

$$\mathrm{F}_\mathrm{m} \propto \theta_\mathrm{d}{}^2 \; \delta^{0.5} \; \mathrm{B}^{-0.5}, \tag{6.4}$$

$$\mathrm{F_{SC}} \propto \theta_\mathrm{d}^2\ \delta^{-(2+\alpha)}\ \mathrm{B}^{-(2+\alpha)}. \qquad (6.5)$$

Thus for a fixed size, one needs *higher* Doppler factors and *lower* magnetic fields to reproduce the higher radio fluxes of RBLs. On the other hand, the spread of X-ray fluxes can likely be due to an intrinsically large range of magnetic fields and/or beaming factors. It is also possible that θ_d has large variations.

a) B, δ for Single Sources

To get a feeling of the order of magnitude of these parameters, we first apply the SSC model to the single sources, using for the radio the fluxes and angular sizes measured with the VLBI and reported in Ghisellini et al. (1993) for 19 of the 28 RBLs and 12 of the 13 FSRQs of our sample. No high resolution radio data are available at present for the EMSS XBLs.

Table 6.1 reports the values of δ and B derived for the RBLs and FSRQs in common with the Ghisellini et al. sample. Following Ghisellini et al. we included in the calculation the objects for which the redshift is poorly or not known, assigning to the latter objects a lower limit of 0.2 derived by their stellar appearance (Stickel et al. 1991). Lower limits on z yield upper limits on the magnetic field (see above).

In Table 6.1, the Doppler factors were recalculated for consistency. They differ by those listed in Ghisellini et al., calculated after Marscher (1980), by a negligible factor ($\sim$ 0.2). The average δ is 2.64 $\pm$ 2.22 (standard deviation) and 3.39 $\pm$ 2.94 for RBLs and FSRQs, respectively. A large spread is also present for the magnetic field; for RBLs $\langle B \rangle$ = 116 milligauss with a large dispersion ($\pm$ 315 milligauss). However, if 2254+074, which has a magnetic field much higher than the other sources, is removed, the mean drops to 47 ($\pm$ 99) milligauss. For FSRQs $\langle B \rangle$ = 69 ($\pm$ 76) milligauss. Although variable from source to source the angular sizes are more tightly distributed ($\langle\theta_d\rangle = 0.48\pm$ 0.27 mas for RBLs, $\langle\theta_d\rangle = 0.46\pm$ 0.16 mas for FSRQs).

The intrinsic spread in δ and B is shown in Figure 6.1, where the Doppler factors are plotted as a function of the magnetic fields for RBLs and FSRQs. A highly significant ($P_{SK} \sim 99.99\%$) trend of decreasing δ with increasing B is present for RBLs ($P_{SK} \sim 92.5\%$ for FSRQs). This is predicted by eq. (6.5), specifically $B \propto \delta^{-1} F_x^{-0.36} \theta_d^{-2.4}$; because the variations of the angular size are small with respect to the variations of the other three quantities, this relationship predicts that, for a given X-ray flux, B and δ are anticorrelated. Note that the slope of the anticorrelation in Figure 6.1 is roughly –1. In addition, eq. (6.5) shows that the spread in F_x is due to a large variation of *both* the Doppler factor and the magnetic field.

b) F_m, F_x as a Function of δ, B

In the previous example we learned that, besides δ, the magnetic field also plays a fundamental role in the SSC emission. We now use this information to interpret the diagram of Figure 4.12a.

The diagram of Figure 4.12a is repeated in Figures 6.2 and 6.3, where the flux of the radio core component (from VLA measurements) is plotted versus the Rosat flux at 1 keV for the RBLs (filled circles), the EMSS and LASS XBLs (open circles), and the FSRQs (crosses). On top of it we have drawn lines of flux densities for constant Doppler factors (dotted lines) and constant magnetic fields (solid lines), in the case $\theta_d = 0.1$ and 0.6 mas, respectively (from the average θ_d of the distribution; see above). The position of the lines is weakly dependent on the value of the redshift; we show the results for a redshift fixed at the average of RBLs.

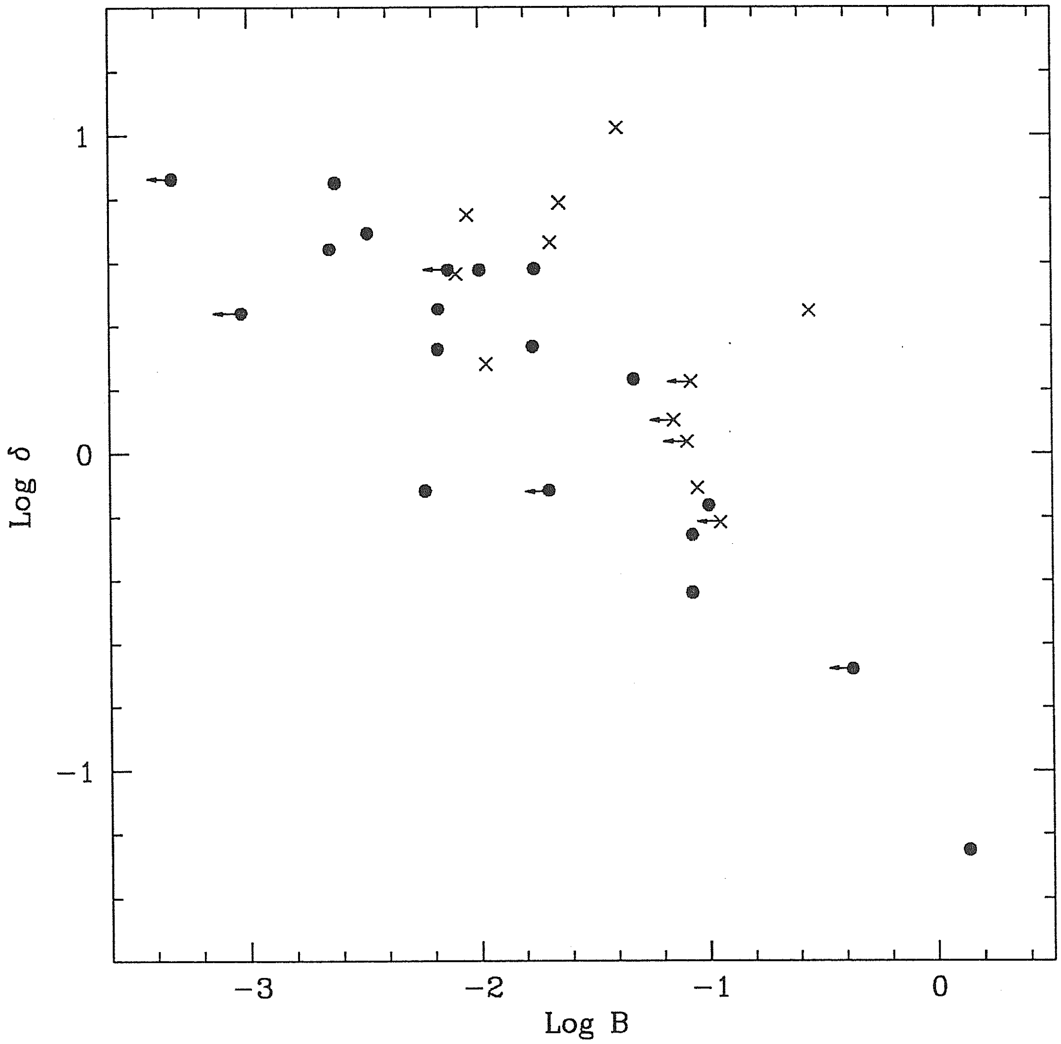

Figure 6.1: Plot of the Doppler factors, δ, and magnetic field intensities, B, derived applying the homogeneous SSC model of Jones, O'Dell, & Stein (1974) to the VLBI data of RBLs (filled circles) and FSRQs (crosses). Upper limits to B due to both lower limits to the redshift and upper limit on the angular size are indicated. The two parameters anticorrelates well (99.9%); in both cases a large spread is present.

Independently of the values of the angular size, the value of δ increases from the bottom to the top of the diagram, while B decreases in the same sense. Note that the trend of the datapoints for radio-selected and X-ray selected objects lies approximately along a line of $\delta \approx$ constant, contrary to the scheme described in Section 4.4.2 (see Figure 4.10). The Doppler factor is higher for radio-selected than for X-ray selected Blazars. However, the spread within the single class is accounted for by variations of the magnetic field. Specifically, radio and X-ray fluxes for RBLs and FSRQs are produced in regimes of higher Doppler factors and lower magnetic fields than for XBLs.

We recall that the radio data in Figures 6.2 and 6.3 are from the VLA, a choice motivated by the fact that no high resolution radio data are available for XBLs. In fixing θ_d we implicitly assumed that the dimensions are also the same for XBLs, which may not necessarily be true (see below). In addition, fixing the angular size is *per se* arbitrary, the single source being characterized by a specific value of θ_d. However, in Figures 6.2 and 6.3 we are not interested in deriving the correct values of B and δ (which, in fact, change considerably in the two plots), but to show the trend of these two parameters going from XBLs to FSRQs. This is independent on the choice of the angular size.

Figures 6.2 and 6.3 shows that beaming alone can not account for differences between radio-selected and X-ray selected Blazars, and that the spread within classes probably reflects intrinsic differences (e.g., in B or θ_d) rather than δ. These must include the effect of a variable magnetic field, which increases going from radio-selected to X-ray selected objects. Because the maximum synchrotron frequency is proportional to $\gamma_{max}^2 \times$ B, where γ_{max} is the maximum energy of the electron population, the difference in B implies a spectral difference in the BBEDs, which qualitatively accounts for the fact that radio-loud

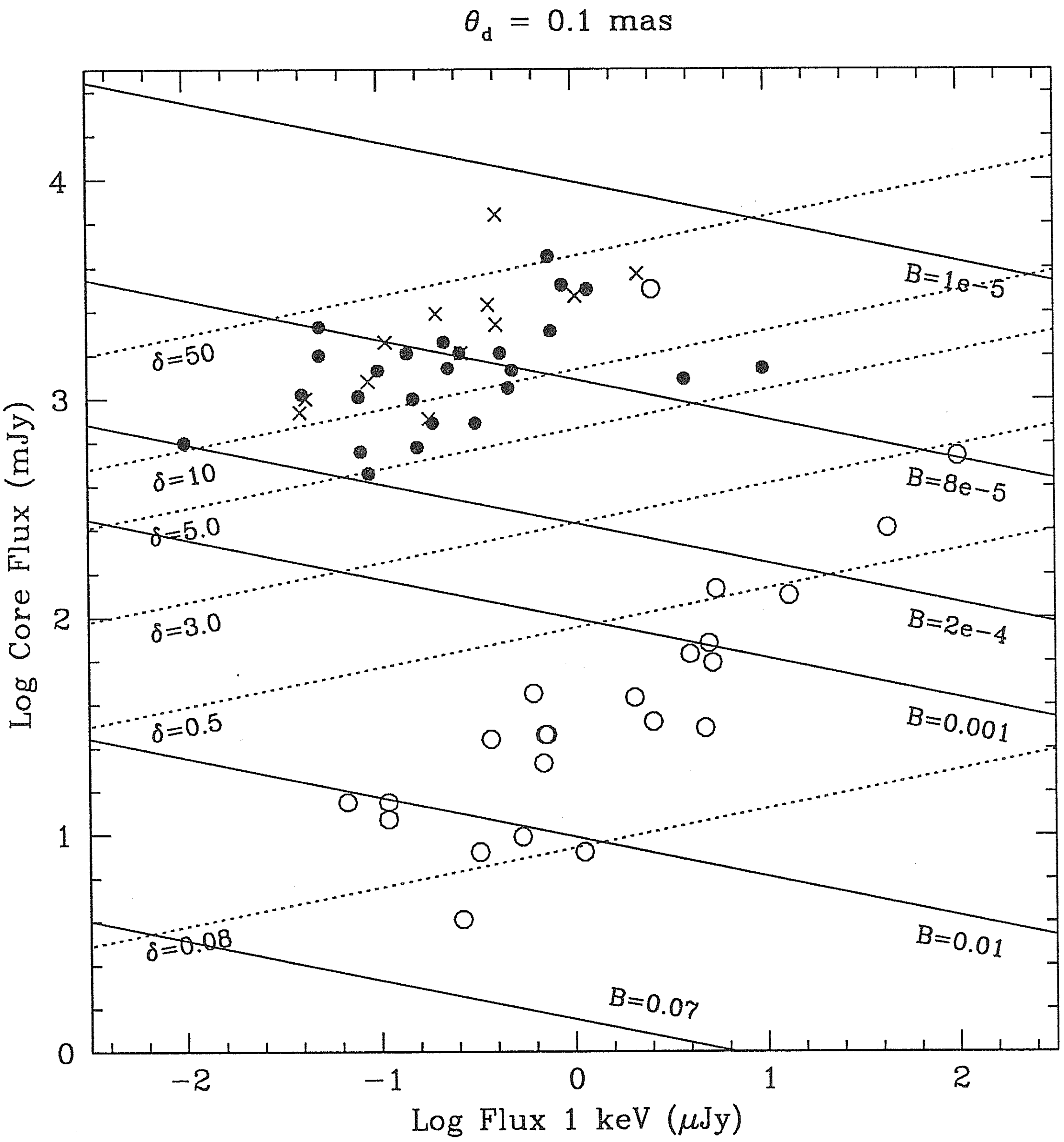

Figure 6.2: The same plot as in Figure 4.12a, with lines δ = constant (dotted lines) and B = constant (solid line) on top. The lines are calculated fixing the angular size to 0.1 mas (see text). The higher radio fluxes of radio-selected Blazars are produced in regimes of higher δ and lower B than for XBLs. While the trend of the points is consistent with $\delta \approx$ constant, the spread within the *single* class is related to variations of the magnetic field.

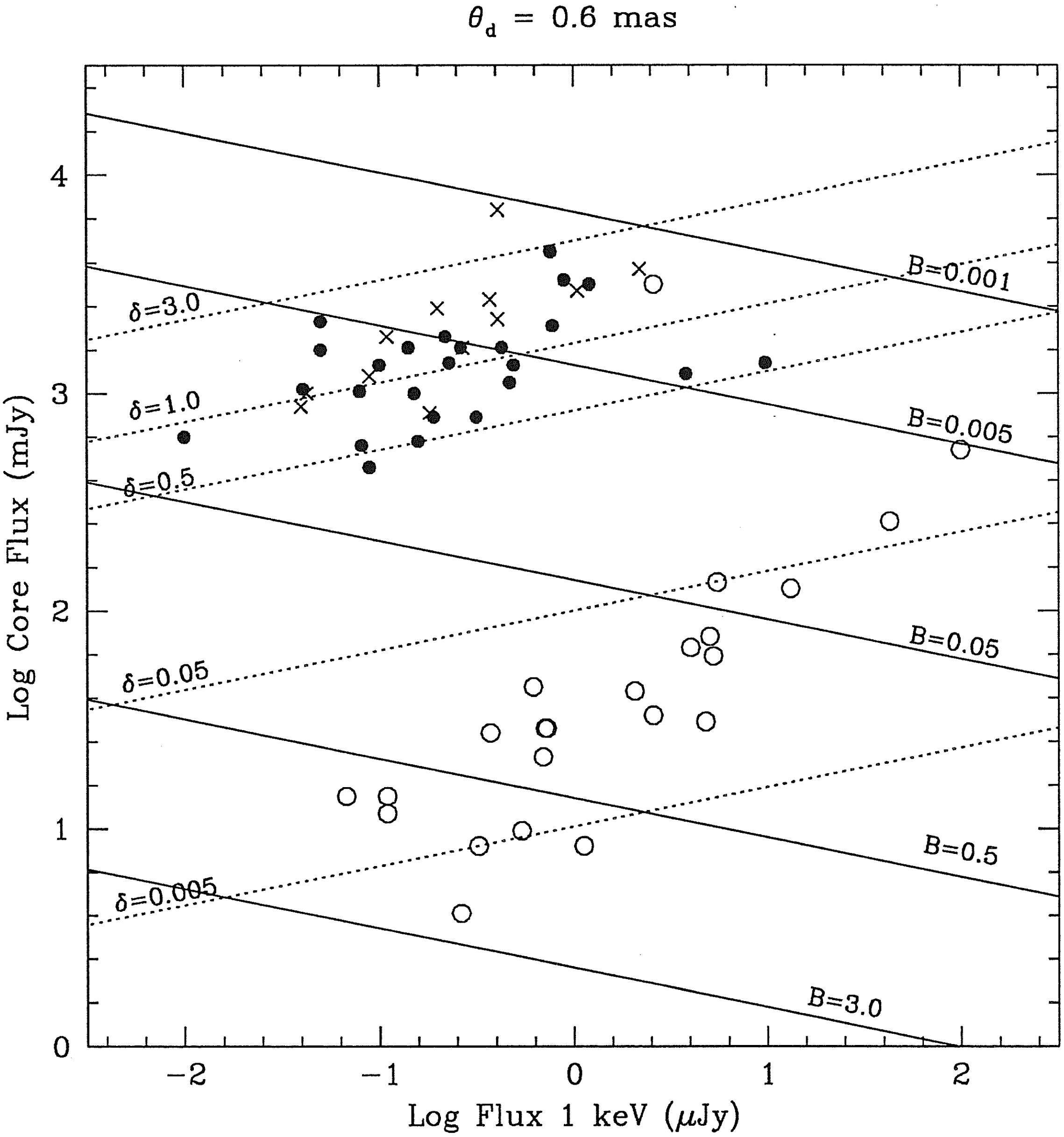

Figure 6.3: Same as Figure 6.2, but for angular size = 0.6 mas. The numerical values of δ and B are smaller and larger, respectively, but the trend in Figure 6.2 is unaffected.

Blazars have the peak of the emission at lower energies than radio-weak Blazars.

6.2 Inhomogeneous Jet Models

In Chapter 5 we showed that RBLs can be divided into three subgroups. This subdivision was based on the $\alpha_{ox} - \alpha_x$ index, i.e., on the basis of how the X-ray continuum connects to the lower frequencies. "Quasar-like" and "XBL-like" objects were identified by $\alpha_{ox} - \alpha_x \gtrsim 0.5$ and $\lesssim -0.5$, respectively, while the sources with the index in the range (–0.5, 0.5) were called "RBL-like". Averaging the spectral distributions of the single sources we worked out the mean BBED of each subgroup (Figure 5.7), which summarized the principal observational differences among quasar-like, RBL-like, and XBL-like Blazars. Beside the gradual steepening of the X-ray spectrum, the ratio of the radio-to-optical flux also decreased going from quasar-like to XBL-like objects.

In the following sections we compare the observed energy distributions of selected sources to the spectra calculated with current inhomogeneous jet models. Our aim is the obtain a quantitative description of the three subclasses in terms of more physical parameters.

6.2.1 BBEDs of Selected Sources

The inhomogeneous jet models are an attempt to model Blazars in terms of their radiative mechanisms, composition of the emitting plasma, and geometry of the jet. The complexity of the physical processes involved translates into a large number of free parameters on which even these relatively simple models depend.

Table 6.1: Homogeneous SSC Model

	VLBI Data [a]			SSC Parameters	
Source	ν_m (GHz)	F_m (Jy)	θ_d (mas)	δ	B (10^{-3} Gauss)
			RBLs		
0048–097	2.3	0.62	0.34	2.76	< 0.9
0454+844	5.0	1.30	0.55	1.71	47.2
0537–441	2.3	4.20	1.10	4.40	2.3
0716+714	5.0	0.50	0.35	0.76	< 20
0735+178	5.0	1.29	< 0.30	3.80	< 7.3
0851+202	5.0	2.30	0.30	4.94	3.3
0954+658	5.0	0.48	0.19	2.84	6.7
1147+245	5.0	0.39	0.90	0.21	< 426
1308+326	5.0	1.97	0.50	3.82	17.5
1519–273	2.3	1.59	0.36	7.30	< 0.5
1538+149	5.0	0.56	0.60	0.69	100
1652+398	5.0	0.45	0.23	0.76	5.8
1749+096	5.0	1.43	0.20	7.1	2.4
1749+701	5.0	0.22	0.39	0.55	84.8
1803+784	5.0	1.80	0.40	3.78	10
1807+698	5.0	0.95	0.79	0.36	84.8
2007+777	5.0	1.17	0.40	2.17	17.1
2200+420	5.0	1.60	0.35	2.13	6.6
2254+074	5.0	0.14	1.00	0.06	1355
			FSRQs		
0016+731	5.0	1.58	0.46	6.14	22.5
0133+476	22.3	2.40	0.08	10.5	40.3
0153+744	5.0	0.64	< 0.59	1.68	< 84.4
0212+735	5.0	1.36	0.47	4.61	20.5
0615+820	5.0	0.61	< 0.50	1.27	< 70.8
0836+710	5.0	1.05	0.34	3.68	8.0
0923+392	5.0	6.90	0.69	5.62	9.0
1039+811	5.0	0.29	< 0.5	0.61	< 113
1150+812	5.0	0.46	< 0.5	1.09	< 81
1633+382	5.0	0.43	0.57	0.78	89.6
1641+399	22.0	6.90	0.30	2.80	280
1928+738	5.0	2.11	0.49	1.91	10.8

Notes to Table 6.1: a = Collected by Ghisellini et al. (1993).

In order to provide constraints to the free parameters, BBEDs with as much data coverage as possible should be used. We thus concentrated on the spectra of sources representative of each subgroup, adding to the data at the three fiducial frequencies of Chapter 5 the fluxes published (in the period 1900 – 1994) at all observed frequencies.[1]

The representative sources were chosen on the basis of a value of $\alpha_{ox}-\alpha_x$ close to the average of the corresponding subgroup, and a sufficient number of published data. These criteria yielded 1538+149, 0118–272, and 2005–489 as typical "quasar-like", "RBL-like", and "XBL-like" Blazars, respectively. Figure 6.4a-c shows their BBEDs (filled circles) converted to rest-frame frequencies, in units of intrinsic power (νL_ν versus ν). The maximum and minimum observed powers are plotted at each frequency.

In the X-ray band, the Rosat spectrum has been plotted together with the range of uncertainties allowed by the spectral index, except for 2005–489 for which the error on the slope is smaller than the symbol size. Besides Rosat, the spectra obtained by previous satellites in a different brightness state/spectral slope of the object are also plotted, when available. For 0118–272, the Rosat data provided the first determination of the spectrum in the X-ray band. 1538+149 was previously observed with the IPC with a slope slightly steeper than with Rosat (Table 4.3a). For 2005–489, the X-ray spectra plotted are the Rosat observation of Oct-Nov, corresponding to a low state (Table 3.1a), the EXOSAT lowest state (Sambruna et al. 1994b), which is a state very close to the Rosat Oct-Nov observation ($\alpha_x = 2.20^{+0.20}_{-0.14}$), and the highest EXOSAT state, which is the brightest and flattest ($\alpha_x = 1.62 \pm 0.02$) state observed so far for 2005–489 in X-rays.

---

[1] A similar analysis for all the sources in the sample is in progress.

All three objects have at least a 3σ upper limit for the γ-ray flux at 100 MeV in the GRO database. For 2005–489, a flux corresponding to a marginal detection (2σ) is also available.

6.2.2 NON-ACCELERATING AND ACCELERATING JET MODELS

The continuum distribution of BL Lacs has been successfully interpreted, for a long time, in the frame of inhomogeneous jet models. We will consider a particular class of these models, where the jet consists of an inner paraboloid smoothly connected to an external cone (Ghisellini, Maraschi, & Treves 1985; GMT). Along the jet, the magnetic field and particle density are parameterized such that $B=B_0x^{-m}$, $K=K_0x^{-n}$, respectively, where $x=(R_0/R)$ is the distance from the initial radius R_0. The spectrum of the relativistic particles radiating via synchrotron is a power law distribution with constant spectral index, extending up to a maximum electron energy γ_{max} which is allowed to vary with x. The maximum synchrotron frequency, ν_{max}, is thus a function of x, with the largest frequencies typically being emitted in the innermost part of the jet.[2] For typical parameters, the energetically dominant part of the jet is the inner paraboloid, which accounts for the emission above 10^{13-14} Hz, while the cone accounts for the radio emission.

In the GMT model the bulk Lorentz factor of the emitting plasma is kept constant (non-accelerating jet model). The total spectrum of the jet is obtained by integrating the contributions of local blobs, each emitting via SSC. At a given frequency, the total synchrotron luminosity goes like $KB^{1+\alpha} \propto \tau B^{1+\alpha}$,

---

[2] ν_{max} corresponds to the maximum energy to which the synchrotron emission extends. It should not be confused with the peak frequency, which is the frequency at which the synchrotron output peaks.

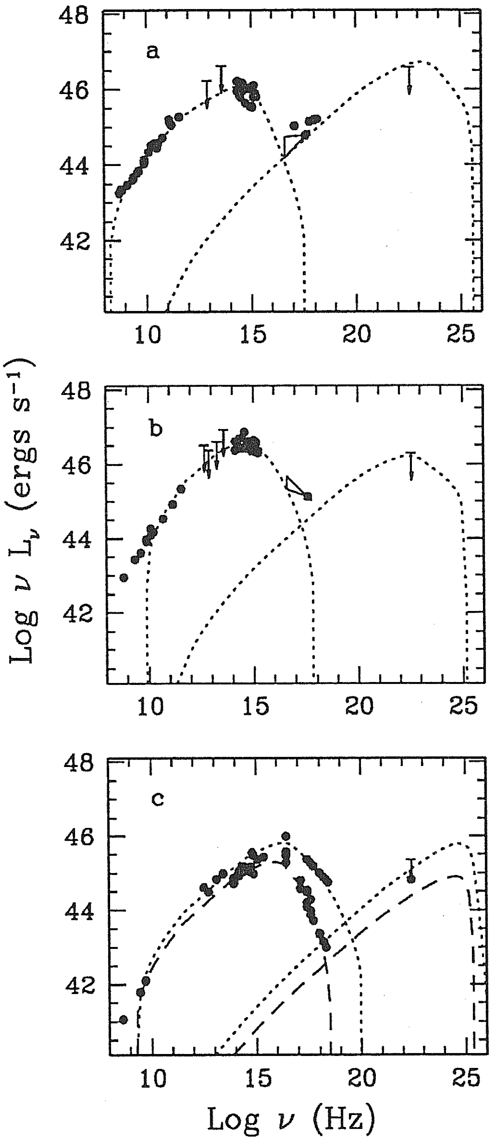

Figure 6.4: Broad-band energy distributions for the quasar-like object 1538+149 (top), the RBL-like source 0118–272 (middle), and a typical XBL-like, 2005–489 (bottom). The data are not simultaneous; average flux densities are plotted at each frequency. The distributions have been converted to rest-frame frequencies and K-corrected. Shown in dotted lines are the SSC spectra calculated within the accelerated jet model of GM (see text). A separate calculation for the lower state of 2005–489 is indicated in dashed line.

where τ is the optical depth, while the IC component is $\propto \tau^2 B^{1+\alpha}$.

This model was successfully applied by GMT to interpret the flux distributions of a few sources. Motivated by the *systematic* differences observed between radio-selected and X-ray selected BL Lacs, Ghisellini & Maraschi (1989; GM) considered a variant of the GMT model, where the bulk Lorentz factor Γ_B of the emitting plasma is an increasing function of the distance. The plasma's internal energy is converted into bulk motion in the parabolic region, and the plasma accelerates along the jet, $\Gamma_B = \Gamma_{B,0} x^a$. The radiation at the higher frequencies, which is emitted in the inner regions, is less beamed than the radiation coming (at smaller energies) from the external ones.

The net result is that the observed spectrum depends on the viewing angle (see Figure 3 of GM). In the limit of small viewing angles, the emission from the outer jet regions is enhanced with respect to the intrinsic, "unbeamed" spectrum, while little variation is expected in the contributions from the inner parts of the jet. This situation would lead to the typical spectrum of an RBL (Figure 4 of GM). In contrast, the case of large orientations of the jet axis, where the emission from radio is dimmed, would correspond to an XBL. In the context of this model, therefore, the viewing angle is the basic parameter leading the RBL/XBL appearance. However, our earlier analysis (Section 6.1) shows that it cannot be the only parameter.

a) Accelerated Jet Model

We now test the accelerated jet model against the BBEDs of our representative sources illustrated in Figure 6.4. Because of the large number of free parameters of the model, a fit procedure (based on the minimization of the χ^2) is impractical. Instead, we changed the various parameters one at a time until we found a solution (not unique) consistent with the data. The synchrotron and IC spectra calculated for the three cases are compared to the observed BBEDs in Figure 6.4a-c (solid lines). The corresponding parameters are reported in Table 6.1a.

The models obtained in the three cases indicate very different situations. In particular, the X-ray emission is differently interpreted. In the quasar-like object 1538+149 (Figure 6.4a), the synchrotron component ends at $\approx 10^{15}$ Hz and the X-ray spectrum is entirely consistent with an SC origin. Here, higher states in the X-ray band are due to variations of the Compton component only, as suggested by the IPC data. At the other extreme, the X-ray emission in the XBL-like source 2005–489 (Figure 6.4c) is due to the high energy tail of the synchrotron component.[3] An intermediate situation is represented by the typical RBL-like 0118–272 (Figure 6.4b), where both the synchrotron and Compton components are likely contributing to the X-ray spectrum. An analogous case is 0537–441 (Treves et al. 1993).

Table 6.1a shows the parameters which affect the relative importance of the synchrotron and SC components. First, the intrinsic acceleration of the plasma is similar in the three cases ($\Gamma_{\rm B,max} \approx 5$), but, as a result of the different viewing angles, the Doppler boosting is remarkably different, with the quasar-like object having a higher beaming factor ($\delta \sim 10$) than the XBL-like one ($\delta \sim 3$).

However, other physical quantities in Table 6.1a change appreciably from one object to the other. In particular, the XBL-like object is consistent with higher magnetic fields and lower dimensions than the quasar-like source.

---

[3] Note that in 2005–489 the Compton component peaks at $\approx 10^{25}$ Hz. Because of its proximity (z=0.071), TeV emission from 2005–489 could be detected, as in Mrk 421, because their absorption by the IR background radiation should be modest. However, 2005–489 is in the southern emisphere, so that it can not be observed by the Whipple Observatory.

In both cases the particle density is the same, as a consequence of the required decrease of the optical depth and of the length scale. In addition, the maximum synchrotron frequencies derived here in the two cases are also different, being larger in 2005–489 (10^{18-20} Hz) than 1538+149 (10^{17}). Intermediate values of the parameters are found for the RBL-like object 0118–272.

A change in viewing angle alone is not sufficient to account for the different observed spectra. An example is shown in Figure 6.5a. The upper curve (solid line) is the theoretical spectrum of 1538+149 calculated with the parameters in Table 6.1a. The filled circles are the continuum energy distribution of 2005–489. Plotted in different linestyles are the spectra predicted by the accelerating model starting from the spectrum of 1538+149, and increasing the viewing angle. The curves plotted in dotted, dashed, and dot-dashed lines correspond to $\vartheta = 8^\circ$, 12°, and 16°, respectively. The "debeaming" of the quasar-like spectrum yields a decrease of the peak flux of the synchrotron component, with a corresponding decrease of the SC component. The X-ray luminosity remains approximately unchanged.

As discussed above, at larger angles we are intercepting decreasing amounts of the outer emitting regions, from where the radio to UV emission comes. However, Figure 6.5a shows that this rigid decrease of the spectrum is insufficient, and that to match the observed data one *also* needs a shift of the peak of the spectrum to higher energies. In fact, if the de-beamed spectrum corresponding to $\vartheta = 16^\circ$ (dot-dashed line in Figure 6.5a) is recalculated with a higher ν_{max} ($\sim 3 \times 10^{19}$ Hz), the energy distribution produced is closer to the higher state of 2005–489 (Figure 6.5b).

These arguments point toward a new, physical characterization of the Blazar classes, in terms of variations of fundamental quantities (magnetic field,

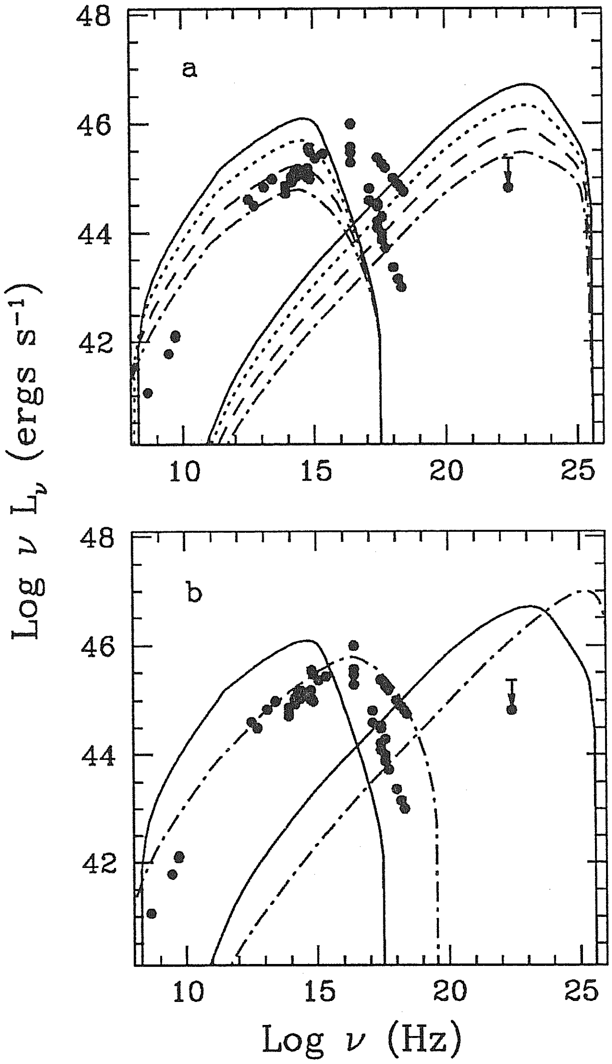

Figure 6.5: *Panel a:* The solid line represents the spectrum calculated with the GM model for the quasar-like object 1538+149, with a viewing angle of $\vartheta = 4°$. The filled circles are the observed spectrum for the XBL-like object 2005–489, which is consistent with $\vartheta = 16°$. The dotted, dashed, and dot-dashed lines are the SSC spectra obtained "de-beaming" the solid line by $\vartheta = 8°$, $12°$, and $16°$, respectively, leaving fixed all the other parameters. A change in viewing angle alone is not enough to go from a radio-selected to an X-ray selected object. *Panel b:* The "de-beamed" curve corresponding to $\vartheta = 16°$ is recalculated for a higher ν_{max}. The theoretical curve approaches the data of 2005–489.

dimensions, ν_{max}). The viewing angle, and consequently, the beaming of the radiation, are now proved not to be the primary leading quantities.

b) Non-accelerated Jet Model

Because the energy distributions appear to have only a weak dependence on the viewing angle, the assumption that the plasma is accelerated is also weakened. We thus looked for a modelling of the BBEDs using the non-accelerated jet models, where the Lorentz factor is constant (equal to $\Gamma_{\mathrm{B,0}}$) along the jet. This class of models (GMT) is obtained from the GM model setting the parameter a (the index of the acceleration law) equal to zero. Because the bulk Lorentz factor need not change much (Table 6.1a), we looked for solutions with $\Gamma_{\mathrm{B,0}}$ fixed to the same values in all three objects.

Figure 6.6a-c shows the calculated models, corresponding to the parameters reported in Table 6.1b. A Lorentz factor $\Gamma_{\mathrm{B,0}} = 5$ has been adopted in all three cases. The variation of this factor has the effect of rescaling the other parameters, but otherwise does not affect the results.

The viewing angles and the beaming factors derived for the three objects in the case of the non-accelerated jet model are found in a smaller range than for the accelerated jet model, $\vartheta \sim 6 - 10$ and $\delta \sim 5 - 8$, with the quasar-like (XBL-like) object at lower (higher) angles and higher (lower) δ. This indicates that some beaming is still necessary to account for the three energy distributions, albeit not sufficient. In fact, Table 6.1b shows that, again, the three sources differ in magnetic field intensity, dimensions, and maximum synchrotron frequency, with the quasar-like object having smaller field, larger dimension, and smaller ν_{max} than the XBL-like one.

From the magnetic field and synchrotron frequencies reported in Table 6.1, one obtains that the maximum electron energy, γ_{max}, reached in an XBL-like

Table 6.2: Inhomogeneous Jet Models

	1538+149 (a)	0118 272 (b)	2005 489 (c)		Notes
			High State	Low State	
A. Accelerated Jet					
R_0	1×10^{15}	1×10^{15}	2×10^{14}	2×10^{14}	[cm], initial radius of parab.
$R_{max,par}$	1×10^{18}	1×10^{18}	4×10^{17}	4×10^{17}	[cm], max. length of parab.
$R_{max,cone}$	5×10^{21}	1×10^{20}	1.2×10^{20}	1.4×10^{20}	[cm], max. length of cone
B_0	6.5	78	135	135	[Gauss], magnetic field at R_0
τ_0	3.6×10^{-5}	8.9×10^{-6}	1×10^{-6}	2×10^{-6}	Optical depth at R_0
ν_{max}	3.5×10^{17}	6×10^{17}	1.1×10^{20}	3×10^{18}	[Hz], max. synchro. frequency at R_0
m	1.0	1.0	1.0	1.0	$B=B_0(r/r_0)^{-m}$
n	0.50	0.50	0.10	0.50	$K=K_0(r/r_0)^{-n}$
$\Gamma_{B,0}$	1.0	1.0	1.0	1.0	Initial bulk Lorentz factor
a	0.25	0.25	0.20	0.20	$\Gamma_B = \Gamma_{B,0}(r/r_0)^{-a}$
ϑ	4°	10°	16°	16°	Viewing angle
K_0	5.5×10^4	1.3×10^4	7.5×10^3	1.5×10^4	[cm^{-3}], el. density at R_0
$\Gamma_{B,max}$	5.6	5.6	4.6	5.0	Final value of bulk Lorentz factor
δ	9.7	5.8	3.5	3.4	Doppler factor
U_r/U_B	7.63	0.71	0.84	0.27	Photon/magnetic densities at R_0
β	3.7	5.5	4.3	4.6	Predicted superl. speed
B. Non-accelerated Jet					
R_0	1×10^{15}	5×10^{14}	1×10^{14}	1×10^{14}	[cm], initial radius of parab.
$R_{max,par}$	1×10^{18}	1×10^{17}	1×10^{17}	1×10^{17}	[cm], max. length of parab.
$R_{max,cone}$	5.3×10^{21}	1×10^{20}	3×10^{20}	3×10^{20}	[cm], max. length of cone
B_0	10	90	130	110	[Gauss], magnetic field at R_0
τ_0	4×10^{-5}	2×10^{-5}	2.8×10^{-6}	4.5×10^{-6}	Optical depth at R_0
ν_{max}	2.5×10^{15}	1×10^{17}	1.7×10^{19}	4×10^{17}	[Hz], max. synchro. frequency at R_0
m	1.0	1.0	1.0	1.0	$B=B_0(r/r_0)^{-m}$
n	0.50	0.50	0.20	0.50	$K=K_0(r/r_0)^{-n}$
$\Gamma_{B,0}$	5.0	5.0	5.0	5.0	Initial bulk Lorentz factor
ϑ	6°	7°	10°	10°	Viewing angle
K_0	6×10^4	6×10^4	4.2×10^4	6.8×10^4	[cm^{-3}], e- density at R_0
δ	7.8	7.3	5.7	5.7	Doppler factor
U_r/U_B	0.58	0.61	0.92	0.25	Photon/magnetic densities at R_0
β	4.0	4.3	4.8	4.8	Predicted superl. speed

Notes to Table 6.2: (a) = quasar-like object; (b) = RBL-like object; (c) = XBL-like object.

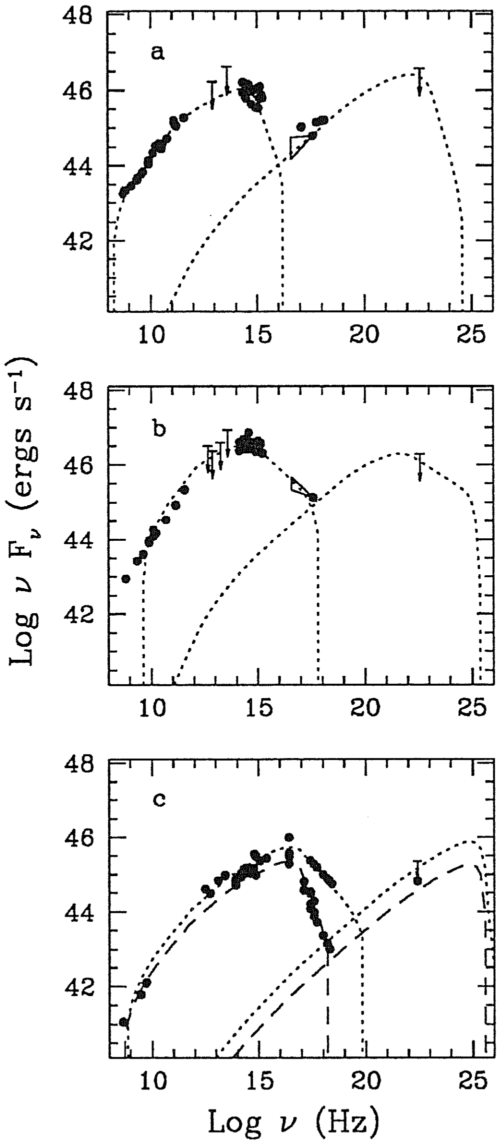

Figure 6.6: Same as Figure 6.4. The theoretical spectra are calculated within the non-accelerated jet model (GMT), for a fixed Lorentz factor 5.0. The derived Doppler factor are close ($\delta \sim 5$ for the quasar-like object, $\delta \sim 8$ for the XBL-like one). The quasar-like object has a lower magnetic field and larger dimension than the XBL-like one. The typical RBL in the middle panel has intermediate values.

object is a factor 4 (non-accelerated case) or 25 (accelerated case) higher than in a quasar-like source. This is just a manifestation of the observational fact that the mean peak of the synchrotron luminosity is different for the three classes. The most natural interpretation is that the acceleration mechanism(s) in the former objects are more powerful (continuous re-acceleration? multiple shocks?); however, this need not be the case if continuous injection occurs, where it can be shown that the peak frequency increases with the magnetic field (Maraschi et al. 1994a). In this scheme, peaks at the higher energies are simply a consequence of the higher magnetic field only.

The effect produced by the change of ν_{max} is schematically described in Figures 6.7a-c. In panel a, the solid line represents the theoretical model of 1538+149, while the filled circles are the observational data for 2005–489. The dotted line plotted in panel b represents the theoretical model of 1538+149 calculated with all the parameters in Table 6.1b but with $\nu_{max} = 5 \times 10^{17}$ Hz. This enhances the IR to X-ray portion of the synchrotron spectrum, and the related up-scattered Compton photons. The dotted spectrum in panel b has $\alpha_{ro} \approx 0.5$ and $\alpha_{ox} \approx 1.0$, moving the object into the region typical of an XBL-like object (Figure 5.5). The same migration happens in terms of $\alpha_{ox} - \alpha_x$, because the X-ray band ($10^{16} - 10^{18}$ Hz) is now entirely dominated by the steep synchrotron emission.

As far as the relative strength of the radio, optical, and X-ray fluxes is concerned the change in ν_{max} is sufficient to explain the migration of the points from quasar-like to XBL-like in the color-color plots. However, the change in ν_{max} is not sufficient to account for the shape of the whole flux distribution of the single sources. As it is clear in Figure 6.7b, the predicted synchrotron and SC fluxes are 2 and 3 orders of magnitudes higher than the observed ones,

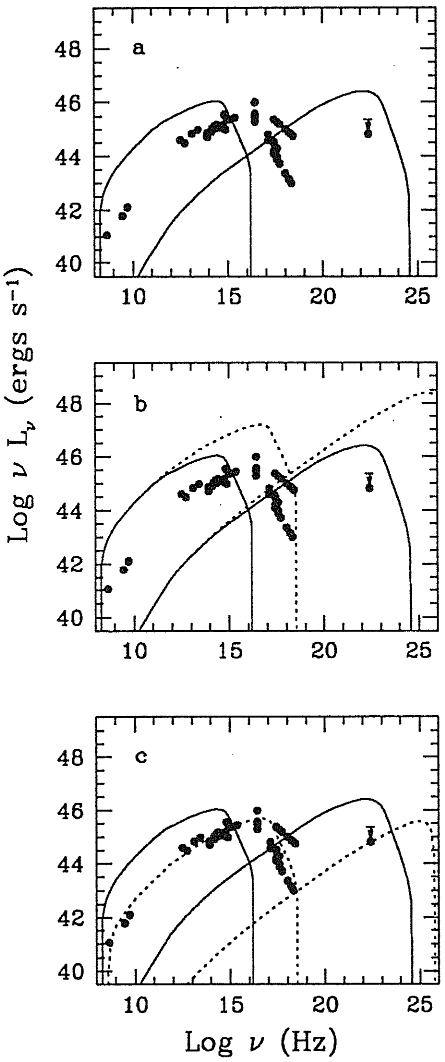

Figure 6.7: Transition from a radio-selected to an X-ray selected Blazar. *Panel a:* The data are the observed energy distribution of the XBL-like object 2005–489, the solid line is the theoretical spectrum of the quasar-like source 1538+149, from Figure 6.6. *Panel b:* The dotted line is the solid line recalculated with higher ν_{max} and all the other parameters fixed. The dotted line corresponds to an object with radio-to-optical and optical-to-X-ray colors typical of an XBL-like Blazar. *Panel c:* The spectral distribution of 2005–489 is better matched if the magnetic field is increased and the scale length is decreased. These steps do not change the colors.

respectively. The further decrease of R_0 (10^{14} cm), of τ_0 (4×10^{-6}), and increase of B_0 (100 Gauss), produces a better match to the observational data (panel c). During these steps, the colors of the spectrum produced are not significantly changed, as only a renormalization occurs.

During the sequence from Figure 6.7a to Figure 6.7c the beaming factor remained unvaried ($\delta \sim 7.8$, Table 6.1b). Clearly, a further fine tuning of the parameters would require changing the viewing angle to better match the data of 2005–489, however at zero-th order a different beaming is not strictly necessary to produce the transition from a quasar-like to an XBL-like object.

6.3 Spectral Variability

Despite the non-simultaneity of the data plotted in Figure 6.4c, the BBED of 2005–489 shows a clear spectral behavior. The continuum rises from radio to IR-Optical, reaching a peak in the soft X-ray band both in the low and in the high state. Above the peak, the spectrum then softens in the low state, a trend observed also in other XBLs (e.g., Sambruna et al. 1994a). The important point is that the major flux variations are localized *above* the peak of the emission, while below it the change is less dramatic. The modelling in Table 6.2a-b shows that the principal difference between the two states in terms of model parameters is the maximum synchrotron frequency, which varies by a factor 100 from the low to the high state. In addition, the particle density decreases more rapidly from inner to outer regions of the paraboloid in the low state.

The behavior of 2005–489 is similar to that of the bright Blazar 3C 279, which was the target of two recent multifrequency campaigns from radio to γ-rays. The BBED of 3C 279, based on simultaneous and near simultaneous data, showed a marked softening with decreasing flux of the synchrotron component, whose peak is located around 10^{14} Hz (Maraschi et al. 1994b). Also in this case the spectrum steepens above the peak when the flux decreases, accompanied by a even more dramatic variation of the Compton component. The variation amplitude of the latter strongly supports a whole SC origin for the X-ray/γ-ray radiation from 3C 279 (Maraschi et al. 1994b).

It is interesting that two objects with very different classifications like 2005–489 and 3C 279 show similar spectral behavior of the synchrotron component, but shifted by 2 orders of magnitude in frequency. This argues, again, for the same emission mechanism working in the Blazar classes, but with different physical scales. In 2005–489 the fact that radiative losses occur at higher frequencies indicates that either a more powerful acceleration mechanism is present, or can simply be related to higher magnetic fields.

Although the spectral coverage for 1538+149 is poorer we can argue from Figure 6.4a that its variability behavior should be close to that of 3C 279. The slightly higher state measured with the *Einstein* IPC is consistent with an enhancement of the Compton component.

A less clear case of variability is that of 0716+714. This object falls into the subgroup of XBL-like Blazars due to the steepness of its Rosat spectrum. However, a previous *Einstein* IPC observation measured a fainter state with a *flatter* spectral slope (Table 4.3a). A flat spectral component was also detected within the Rosat observation, corresponding to a dimming of the emission (Cappi et al. 1994). It is also unusual for its rapid intraday variability in the radio (Quirrenbach et al. 1989). Figure 6.8 shows the energy distribution of 0716+714,

Table 6.3: Model Parameters for 0716+714

	High State	Low State	Notes
Non-accelerated Jet			
R_0	1×10^{14}	1×10^{14}	[cm], initial radius of parab.
$R_{max,par}$	1×10^{17}	1×10^{17}	[cm], max. length of parab.
$R_{max,cone}$	3×10^{20}	3×10^{20}	[cm], max. length of cone
B_0	400	35	[Gauss], magnetic field at R_0
τ_0	3.8×10^{-7}	1×10^{-4}	Optical depth at R_0
ν_{max}	4×10^{18}	1×10^{16}	[Hz], max. synchro. frequency at R_0
m	1.0	1.0	$B=B_0(r/r_0)^{-m}$
n	-0.50	0.30	$K=K_0(r/r_0)^{-n}$
$\Gamma_{B,0}$	5.0	5.0	Initial bulk Lorentz factor
ϑ	8°	8°	Viewing angle
K_0	5.7×10^{3}	1.5×10^{6}	[cm^{-3}], el. density at R_0
δ	6.7	6.7	Doppler factor
U_r/U_B	0.04	1.54	Photon/magnetic densities at R_0
β	4.6	4.6	Predicted superl. speed

where the high state measured with Rosat and the low state of *Einstein* are shown. Plotted in solid and dotted lines are the spectra calculated with the non-accelerating jet model (see Table 6.3), for the high and low state, respectively.

In the higher state, the object behaves like an XBL-like object, with $\nu_{max} = 4 \times 10^{18}$ Hz and high magnetic densities ($U_r/U_B \sim 0.04$). The SC component peaks at the same frequency as in 2005–489. In the low state, $\nu_{max} = 1 \times 10^{16}$ Hz, and the system is now dominated by the radiation field density ($U_r/U_B \sim 1.5$). This spectrum resembles that of a typical quasar-like Blazar, with the bulk of the emission at $\sim 10^{22}$ Hz. Clearly, 0716+714 represents an interesting case of an object with mixed physical properties.

Multiwavelength spectral variability is a powerful tool to understand the emission processes in Blazars. Once again, the behavior exhibited by the different

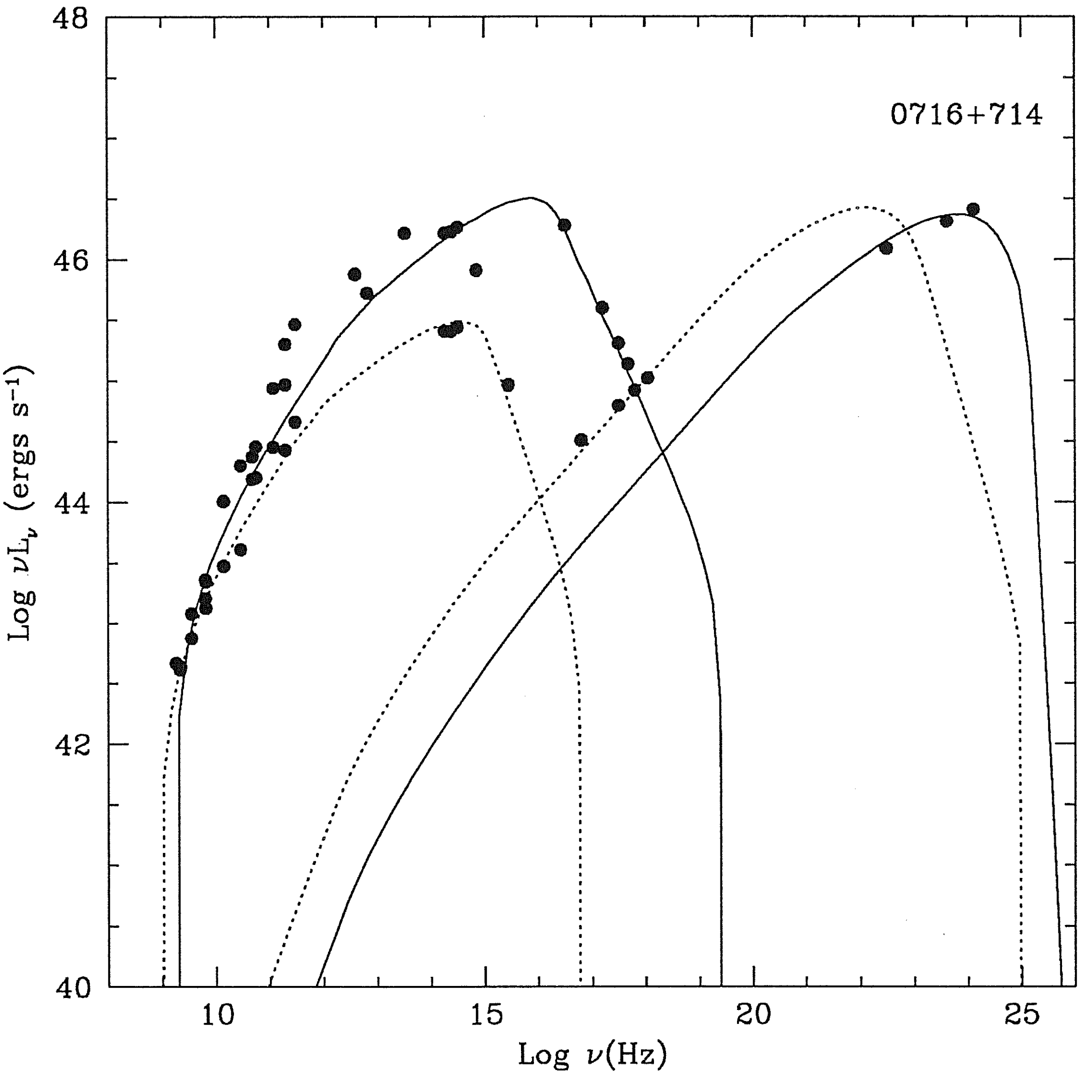

Figure 6.8: Spectral variability of 0716+714. Data are not simultaneous, being average values collected from the literature. The solid line is the theoretical spectrum calculated with the GMT model for the higher state. The spectrum calculated for the lower state is plotted in dotted line. During the higher state, the source has a spectrum similar to an XBL-like object, with a peak at $\approx 10^{16}$ Hz and a steep X-ray spectrum; during the lower state it is closer to a quasar-like object, with a peak of the synchrotron output in the IR/ optical and a flat X-ray continuum.

objects is the result of a different physical balance of the various quantities involved.

Conclusions: We have shown that the properties of the Blazar classes can not be explained exclusively in terms of varying viewing angles/beaming, but require different physical parameters. The transition from a quasar-like to an XBL-like object corresponds to increasing magnetic fields, decreasing scale lengths, and increasing maximum synchrotron frequencies. Blazars are thus a class of objects with similar underlying emission mechanisms, whose different continuum properties are the result of a different balance of the various physical parameters.

CHAPTER VII

Conclusions

7.1 Overview of the Results

The work presented in this dissertation can be divided in two parts. In the first, the analysis of the Rosat data for a complete sample of radio-selected BL Lacs have been performed. The second part deals with the study of the multifrequency continuum properties of Blazars and their theoretical interpretation.

In Chapters 3 and 4 we fitted the Rosat spectra of the single sources, using various spectral models, and studied the mean properties of the sample. The distribution of the Rosat spectral indices of RBLs was compared with the distributions obtained with Rosat for other samples of Blazars, including a complete sample of X-ray selected BL Lacs and Flat Spectrum Radio Quasars, and with those obtained from the *Einstein* IPC data, which were reconsidered for a self-consistent analysis. We explored correlations of the Rosat slopes and fluxes versus with meaningful quantities like the redshifts and the radio morphology parameters. The principal results are:

- *X-ray spectral shape: unabsorbed simple power laws*

No evidence for intrinsic absorption in the range 0.15 – 2.0 keV has been found from the fits with a single power law + free N_H, and in general the spectra are well described by a single power law with absorption fixed at the Galactic value. A more complex spectrum is indicated in the cases with a high number of counts ($> 10{,}000$). For 1652+398 (Mrk 501) and for 0716+714, a broken power law yields a significant improvement of the fit, with a convex and concave spectral shape, respectively. In 2005–489, a wide absorption feature around 0.5 keV seems to be observed. We showed that, because of the instrumental gain variations, no firm conclusions about the presence of a feature can be stated.

- *RBLs have broad, soft Rosat energy distributions...*

The distribution of the Rosat photon indices for RBLs is rather wide, spanning the range $1 < \Gamma < 3$ with a mean of 2.20 and standard deviation 0.46. The distribution is not consistent with a single value of the average slope, but has a steep ($\Gamma = 2.4 - 3.0$, 3 objects) and a flat ($\langle\Gamma\rangle = 1.66 \pm 0.07$, 4 objects) tail. The sources with flatter spectra exhibit quasar-like properties (FRII radio morphology, VLBI polarization, broad emission lines).

- *...similar to those of XBLs...*

No differences are found, on average, between the Rosat slopes of RBLs and XBLs, which are in both cases distributed around the same mean (~ 2.2). RBLs and XBLs are steeper than FSRQs, whose distribution of Rosat slopes spans the range $0.5 - 2.0$ with a mean ~ 1.6.

- *...and steeper than measured with the IPC*

Eleven RBLs previously observed with the IPC have spectra in $0.3 - 3.5$ keV which are flatter than the Rosat ones. This indicates a possible Compton component emerging at $\gtrsim 2.0$ keV in the X-ray spectra of RBLs. In contrast, the

IPC distributions for XBLs and FSRQs, although limited to a small number of objects, do not differ from the Rosat ones.

- *The X-ray flux correlates with the radio core flux*

The Rosat fluxes of RBLs are correlated ($P_{SK} \sim 96\%$) with the radio core fluxes, with a trend of higher X-ray intensities when the radio core fluxes increase. A higher correlation ($P_{SK} \sim 99\%$) is found for XBLs and FSRQs. The only correlation found for the Rosat slopes is with the redshift, in the sense of flatter slopes with increasing distances; however, it is dominated by the quasar-like objects.

In the second part of the Thesis (Chapters 5 and 6) we discussed the broad band continua of Blazars, on the basis of data collected from published works. We constructed the composite spectral indices α_{rx}, α_{ro}, α_{ox}, and $\alpha_{ox} - \alpha_x$, comparing the distributions of the composite indices for the three samples. We performed a partial correlation analysis of all the spectral indices, the redshift, and the bolometric (peak) luminosity. The Blazar emission properties were interpreted in the frame of current theoretical models. Our findings are:

- *Blazars have different but continuous spectral properties*

Radio-selected objects (FSRQs, RBLs) have steep radio-to-optical continua, peaking in the IR and IR/optical bands, respectively. In contrast, XBLs have flatter radio-to-optical indices, reaching maximum powers in UV/soft X-rays. The X-ray spectra of XBLs are typically a steep extrapolation of the optical continuum, while going from XBLs to RBLs and FSRQs the X-ray spectrum becomes progressively flatter. The three classes form a continuous spectral sequence rather than separate populations.

- *Principal parameters describing Blazars*

Our correlation analysis indicates that important parameters for the description of the continuum emission of Blazars are α_{ro}, $\alpha_{ox} - \alpha_x$, the peak luminosity, and/or the redshift. The strongest correlation is between α_{ro} and $\alpha_{ox} - \alpha_x$ (99.9%), with a trend of flatter X-ray spectra for steeper radio to optical continua. There is, in addition, a correlation between α_{ro} and z (93%), in the sense of higher radio to optical indices for more distant objects, which, however, is dominated by RBLs.

- *Beaming alone is not enough*

Using homogeneous SSC and inhomogeneous jet models we showed that the radio to X-ray emission of Blazars can not be explained in terms of varying Doppler factors alone, but rather require a spread in intrinsic parameters (magnetic field and/or sizes). Beaming alone can not explain the BBEDs of typical XBL-like, RBL-like, and quasar-like Blazars. Increasing magnetic field and decreasing dimensions are required going from radio-selected to X-ray selected Blazars.

7.2 What Did We Learn?

One of the principal contributions of this Thesis to the understanding of the Blazar phenomenon is the effort to better quantify the nature of the differences between radio-selected and X-ray selected objects, from both an observational and an interpretative point of view.

Our strongest conclusion is that the emission properties of the two classes can not be quantitatively reconciled in terms of the orientation of the jets to the observer, but instead require a systematic variation of intrinsic physical parameters. More precisely, the spectral distributions from radio to X-rays are accounted for in terms of a continuous variation of the physical parameters governing the balance between the synchrotron and the Self-Compton emission. In particular, XBLs appear to be the objects more strongly dominated by the synchrotron component, with higher magnetic fields and lower dimensions, while in radio-selected Blazars the Compton component is becoming increasingly important. The similarity of the Rosat distributions of RBLs and XBLs, and the fact that for the former class the IPC spectra are flatter than the Rosat ones, suggests that in radio-selected objects the Compton component emerges at higher ($\gtrsim$ 2 keV) energies, although in some individual sources it can appear before (the "flat tail" of the Rosat distribution for RBLs).

A more subtle question concerns the observed continuity of spectral properties among XBLs, RBLs, and FSRQs. This is the observational manifestation of an "evolution" of the physical parameters. The next question is, clearly, why this smooth transition occurs. A first hypothesis is that the change is intrinsic, that is, related to a systematic variation of a leading quantity in the rest-frame of the sources, such as their total luminosities. Alternatively, it could be an effect related to some change of the ambient conditions around the BL Lacs as a result of cosmological evolution. It will be important to test both these scenarios using samples of better statistics at the higher distances/ luminosities.

A great deal of progress would be made in determining the principal variables of the Blazar phenomenology, something analogous to the HR diagram for stars. It is not now clear whether such a fundamental description would be possible (and whether it would be constrained in a two/three dimensional space!); but it is clear that this would *not only* be a matter of taxonomy.

References

Antonucci, R. 1993, *Ann. Rev. Astron. Astrophys.*, **31**, 473

Antonucci, R., et al. 1986, *AJ*, **91**, 1

Antonucci, R., & Ulvestad, J.S. 1985, *ApJ*, **294**, 158

Barr, P., Giommi, P., & Maccagni, D. 1988, *ApJ*, **324**, L11

Barr, P., Giommi, P., Pollock, A., Tagliaferri, G., Maccagni, D., & Garilli, B. 1989, in *BL Lac Objects*, Eds. L. Maraschi, T. Maccacaro, M.-H. Ulrich, (Berlin: Springer - Verlag), p. 267

Barthel, P.D. 1989, *ApJ*, **336**, 606

Bevington, T.R. 1969, "Data Reduction and Error Analysis for the Physical Sciences", (New York: McGraw - Hill)

Biermann, P.L., Schaaf, R., Pietsch, W., Schmutzler, T., Witzel, A., & Kühr, H. 1992, *A&AS*, **96**, 339

Blandford, R.D. 1993, in *Compton Gamma Ray Observatory*, Eds. M. Friedlander, N. Gehrels, & D. Macomb (AIP), p. 533

Blandford, R. & Rees, M.J. 1978, in *Pittsburgh Conference on BL Lac Objects*, Ed. A.M.Wolfe (Pittsburgh: Univ. of Pittsburgh Press), p. 328

Boroson, T.A., & Green, R.F. 1992, *ApJS*, **80**, 109

Bregman, J.N., et al. 1990, *ApJ*, **352**, 574

Brinkmann, W. & Siebert, J. 1994, *A&A*, in press

Browne, I.W.A. 1983, *MNRAS*, **204**, 23p

Brunner, H., Lamer, G., Worrall, D.M., & Staubert, R. 1994, *A&A*, in press

Burbidge, G. & Hewitt, A. 1987, *AJ*, **92**, 1

Canizares, C.R., & Kruper, J. 1984, *ApJL*, **278**, L99

Cappi, M., Comastri, A., Molendi, S., Palumbo, G.G.C., Della Ceca, R., &

Maccacaro, T. 1994, *MNRAS*, submitted

Celotti, A., Maraschi, L., Ghisellini, G., Caccianiga, A., & Maccacaro, T. 1993, *ApJ*, **416**, 118

Celotti, A., Maraschi, L., & Treves, A. 1991, *ApJ*, **377**, 403

Della Ceca, R., Palumbo, G.G.C., Persic, M., Boldt, E.A., De Zotti, G., & Marshall, E.E. 1990, *ApJS*, **72**, 471

Dermer, C.D., & Schlickeiser, R. 1993, *ApJ*, **416**, 458

Edelson, R.A., Pike, G.F., Saken, J.M., Kinney, A., & Shull, J.M. 1992, *ApJS*, **83**, 1

Elvis, M. Lockman, F.J, & Wilkes, B.J. 1987, *AJ*, **97**, 777

Falomo, R., Giraud, E., Maraschi, L., Melnick, J., Tanzi, E. G., & Treves, A. 1991, *ApJL*, **380**, L67

Falomo, R., Pesce, J.E., & Treves, A. 1993a, *AJ*, **105**, 2031

Falomo, R., Pesce, J.E., & Treves, A. 1993b, *ApJ*, **411**, L63

Falomo, R., Pesce, J.E., & Treves, A. 1994, *ApJL*, submitted

Fasano, G., Franceschini, A. 1987, *MNRAS*, **225**, 155

Feigelson, E.D., et al. 1993, Proposal to NASA for observations with Rosat

Fichtel, C.E., et al. 1993, *A&AS*, **97**, 13

Fink, H.H., Thomas, H.-C., Hasinger, G., Predhel, P., Schaeidt, S., Makino, F., & Warwick, R.S. 1991, *A&A*, **246**, L6

Fink, H.H., et al. 1992, MPE Rep. 235, 181

Fiore, F., Elvis, McDowell, J.C., Siemiginowska, A., & Wilkes, B.J., 1994, *ApJ*, **431**, 515

Fleming, T.A., Green, R.F., Jannuzi, B.T., Liebert, J., Smith, P.S., & Fink, H. 1993, *AJ*, **106**, 5

Gabuzda, D.C., Cawthorne, T.V., Roberts, D.H., & Wardle, J.F.C. 1989, *ApJ*, **347**, 701

Gabuzda, D.C., Cawthorne, T.V., Roberts, D.H., & Wardle, J.F.C. 1992, *ApJ*, **388**, 40

Gabuzda, D.C., & Sitko, M.L. 1994, *AJ*, **107**, 884

Garilli, B., & Maccagni, D. 1990, *A&A*, **229**, 88

Gear, W.K. 1993, *MNRAS*, **264**, 919

George, I.M., Warwick, R.S., & Bromage, G.E. 1988, *MNRAS*, **232**, 793

Ghisellini, G. & Maraschi, L. 1989, *ApJ*, **340**, 181

Ghisellini, G., Maraschi, L., Tanzi, E.G., & Treves, A. 1986, *ApJ*, **310**, 317

Ghisellini, G., Maraschi, L., & Treves, A. 1985, *A&A*, **146**, 204

Ghisellini, G., Padovani, P., Celotti, A., & Maraschi, L. 1993, *ApJ*, **407**, 65

Ginzburg, V.L., & Syrovatskii, S.I. 1965, *Ann. Rev. Astron. Astrophys.*, **3**, 297

Gioia, I., Maccacaro, T., Schild, R., Wolter, A., Stocke, J.T., Morris, S., & Henry, J.P. 1990, *ApJS*, **72**, 567

Giommi, P., Ansari, S., & Micol, A. 1994, *A&A*, in press

Giommi, P., Barr, P., Garilli, B., Maccagni, D., & Pollack, A.M.T. 1990, *ApJ*, **356**, 432

Giommi, P., & Padovani, P. 1994, *MNRAS*, in press

Giommi, P., Tagliaferri, G., Beuermann, K., Branduardi-Raymont, G., Brissenden, R., Graser, U., Mason, K.O., Mittaz, J.D.P., Murdin, P., Pooley, G., Thomas, H.-C., & Tuohy, I. 1991, *ApJ*, **378**, 77

Gould, R.J. 1979, *A&A*, **76**, 306

Hartman, R.C., et al. 1993, in *Proceedings of the 2nd Compton Symp.*, (College Park: Univ. Maryland), Sept. 1993, in press

Hutter, D.J., & Mufson, S.L. 1986, *ApJ*, **301**, 50

Jannuzi, B.T., Green, R.F., & French, H. 1994, *ApJ*, **404**, 100

Jones, T.W., O'Dell, S.L., & Stein, W.A. 1974, *ApJ*, **188**, 353

Kawai, N., et al. 1991, *ApJ*, **382**, 508

Kollgaard, R.I. 1994, *Vistas in Astronomy*, **38**, 29

Kollgaard, R.I, Wardle, J.F.C., Roberts, D.H., & Gabuzda, D.C. 1992, *AJ*, **104**, 1687

Königl, A. 1981, *ApJ*, **243**, 700

Kühr, H. & Schmidt, G.D. 1990, *AJ*, **99**, 1

Kühr, H., Witzel, A., Pauliny-Toth, I.I.K., & Nauber, U. 1981, *A&AS*, **45**, 367

Kurfess, J.D. 1993, in *Proceedings of the Second Compton Symposium*, (College Park: Univ. of Maryland), Sept. 1993, in press

Lampton, M., Margon, B., & Bowyer, S. 1976, *ApJ*, **208**, 177

Landau, R., et al. 1986, *ApJ*, **308**, 78

Laurent-Muehleisen, S.A., Kollgaard, R.I., Moellenbrock, G.A., & Feigelson, E.D. 1993, *AJ*, **106**, 875

Lawson, A.J., Turner, M.J.L., Williams, O.R., Stewart, G.C., & Saxton, R.D. 1992, *MNRAS*, **259**, 743

Ledden, J.E., & O'Dell, S.L. 1985, *ApJ*, **298**, 630

Maccacaro, T., Gioia, I.M., Wolter, A., Zamorani, G., & Stocke, J.T. 1988, *ApJ*, **326**, 680

Macchetto, F., et al. 1991, *ApJL*, **369**, L55

Madejski, G.M., Mushotzky, R.F., Weaver, K.A., Arnaud, K.A., & Urry, C.M. 1991, *ApJ*, **370**, 198

Madejski, G.M., et al. 1994, *ApJ*, in press

Madejski, G.M., & Schwartz, D.A. 1989, in *BL Lac Objects*, Eds. L. Maraschi, T. Maccacaro, M.-H. Ulrich, (Berlin: Springer – Verlag), p. 267

Maraschi, L. 1992, in *Variability of Blazars*, Eds. E.Valtoja & M.Valtonen, (Cambridge: Cambridge University Press), p. 447

Maraschi, L., Ghisellini, G., & Celotti, A. 1992, *ApJL*, **397**, L5

Maraschi, L., Ghisellini, G., & Celotti, A. 1994a, in *Multiwavelength Continuum Emission of AGNs*, IAU Symp. 159, Eds. T.J.-L. Courvoisier & A. Blecha

Maraschi, L., Ghisellini, G., Tanzi, E.D., & Treves, A. 1986, *ApJ*, **310**, 325

Maraschi, L., et al. 1994b, *ApJL*, in press

Maraschi, L., & Maccagni, D. 1988, *MSaIt*, **59**, 277

Maraschi, L., & Rovetti, F. 1994, *ApJ*, in press

Marscher, A.P. 1980, *ApJ*, **235**, 386

Marscher, A.P., Marshall, F.E., Mushotzky, R.F., Dent, W.A., Balonek, T.J., & Hartman, M.F. 1979, *ApJ*, **233**, 498

Morris, S.L., Stocke, J.T., Gioia, I.M., Schild, R.E., Wolter, A., Maccacaro, T., & Della Ceca, R. 1991, *ApJ*, **380**, 49

Morrison, R., & McCammon, D. 1983, *ApJ*, **270**, 119

Murphy, D.W., et al. 1993, *MNRAS*, **264**, 298

Murtagh, F., & Heck, A. 1987, "Multivariate Data Analysis", (Dordrecht: D. Reidel)

O'Dea, C., et al. 1988, *AJ*, **96**, 435

Ohashi, T. 1989, in *BL Lac Objects*, Eds. L. Maraschi, T. Maccacaro, M.-H. Ulrich (Berlin: Springer - Verlag), p. 296

Ostriker, J.P. & Vietri, M. 1985, *Nature*, **318**, 445

Ostriker, J.P. & Vietri, M. 1990, *Nature*, **344**, 45

Padovani, P. 1992a, *MNRAS*, **257**, 404

Padovani, P. 1992b, *A&A*, **256**, 399

Padovani, P., & Giommi, P. 1994, *ApJ*, submitted

Padovani, P., & Urry, C.M. 1990, *ApJ*, **356**, 75

Padovani, P., & Urry, C.M. 1991, *ApJ*, **368**, 373

Peacock, J.A. 1983, *MNRAS*, **202**, 615

Pearson, T.J., & Readhead, A.C.S. 1988, *ApJ*, **328**, 114

Perley, R.A. 1982, *AJ*, **87**, 859

Perlman, E. 1994, PhD Thesis, Univ. of Colorado, Boulder

Perlman, E., & Stocke, J.T. 1993, *ApJ*, **406**, 430

Perlman, E., et al. 1994, in preparation

Pesce, J.E., Falomo, R., & Treves, A. 1994, *AJ*, **107**, 494

Pian, E., Falomo, R., Scarpa, R., & Treves, A. 1994a, *ApJ*, in press

Pian, E., Falomo, R., Ghisellini, G., Maraschi, L., SAmbruna, R.M., Scarpa, R., & Treves, A. 1994a, *ApJ*, submitted

Pian, E., & Treves, A. 1993, *ApJ*, **416**, 130

Piccinotti, G., Mushotzky, R.F., Boldt, E.A., Holt, S.S., Marshall, F.E., Serlemitsos, P.J., & Shafer, R.A. 1982, *ApJ*, **253**, 485

Quirrenbach, A., et al. 1989, *Nature*, **337**, 442

Remillard, R.A., et al. 1990, *The HEAO-1 MC-LASS Catalog of Identified X-ray Sources* (July 1990 draft), unpublished

Sambruna, R.M., Barr, P., Giommi, P., Maraschi, L., Tagliaferri, G., & Treves, A. 1994a, *ApJ*, in press

Sambruna, R.M., Barr, P., Giommi, P., Maraschi, L., Tagliaferri, G., & Treves, A. 1994b, *ApJS*, in press

Sambruna, R.M., Barr, P., Maraschi, L., Tagliaferri, G., & Treves, A. 1993, *ApJ*, **408**, 452

Schachter, J.F., Stocke, J.T., Perlman, E., Elvis, M., Remillard, R., Granados, A., Luu, J., Huchra, J.P., Humphreys, R., Urry, C.M., & Wallin, J. 1993, *ApJ*, **412**, 541

Schwartz, D.A., Brissenden, R.J.V., Tuohy, I.R., Feigelson, E.D., Hertz, P.L., & Remillard, R.A. 1989, in *BL Lac Objects*, Eds. L. Maraschi, T. Maccacaro, M.-H. Ulrich (Berlin: Springer – Verlag), p. 209

Schwartz, D.A., & Ku, W. H.-M. 1983, *ApJ*, **266**, 459

Schwartz, D.A., et al. 1978, *ApJL*, **224**, L103

Sembay, S., et al. 1993, *ApJ*, **404**, 112

Shafer, R.A., Haberl, F., Arnaud, K.A., & Tennant, A.F. 1991, XSPEC User's Guide, Version 2 (ESA TM – 09)

Sikora, M., Begelman, M.C., & Rees, M.J. 1994, *ApJ*, **421**, 153

Smith, E. P., O'Dea, C. P., & Baum, S. A. 1993, *BAAS*, **25**, #2, 791

Stark, A.A., Gammie, C.F., Wilson, R.W., Bally, J., Linke, R.A., Heiles, C., & Hurwitz, M. 1992, *ApJS*, **79**, 77

Stein, W.A., O'Dell, S.L., & Strittmatter, P.A. 1976, *Ann. Rev. Astron. Astrophys.*, **14**, 173

Stickel, M., Fried, J.W., & Kühr, H. 1993, *A&AS*, **98**, 393

Stickel, M., Padovani, P., Urry, C.M., Fried, J.W., & Kühr, H. 1991, *ApJ*, **374**, 431

Stocke, J.T., et al. 1993, Proposal to NASA for observations with Rosat

Stocke, J.T., Liebert, J., Schmidt, G., Gioia, I., Maccacaro, T., Schild, R., Maccagni, D., & Arp, H. 1985, *ApJ*, **298**, 619

Stocke, J.T., Morris. S.L., Gioia, I.M., Maccacaro, T., Schild, R., Wolter, A., Fleming, T.A., & Henry, J.P. 1991, *ApJS*, **76**, 813

Tashiro, M., Ueda, Y., Kii, T., Makino, F., Mushoztky, R.F., Makishima, K., & Yamashita, A. 1994, in *New Horizons of X-ray Astronomy*, in press

Treves, A., Belloni, T., Falomo, R., Fink, H., Maraschi, L., Sambruna, R.M., Tagliaferri, G., & Zimmermann, H.O. 1993 *ApJ*, **406**, 447

Treves, A., Morini, M., Chiappetti, L., Fabian, A., Falomo, R., Maccagni, D., Maraschi, L., Tanzi, E.G., & Tagliaferri, G. 1989, *ApJ*, **341**, 733

Trümper, J. 1984, *Phys. Scripta*, **T7**, 209

Tucker, W.H. 1975, "Radiation Processes in Astrophysics", (Cambridge, Mass.: The MIT Press)

Turner, T.J., & Pounds, K.A. 1989, *MNRAS*, **240**, 833

Ulrich, M.-H. 1978, *ApJ*, **222**, L23

Urry, C.M. 1984, Ph.D. Thesis, Johns Hopkins University, Baltimore, Maryland

Urry, C.M. 1988, in *Multiwavelength Astrophysics*, Ed. F.A. Cordova, (Cambridge: Cambridge University Press), p. 279

Urry, C.M., et al. 1993b, *ApJ*, **411**, 693

Urry, C.M., & Mushotzky, R.F. 1982, *ApJ*, **253**, 38

Urry, C.M., Mushotzky, R.F., & Holt, S.S. 1986, *ApJ*, **305**, 369

Urry, C.M., & Padovani, P. 1994, in *The Physics of Active Galaxies*, Eds. G. Bicknell, M. Dopita, P. Quinn, ASP Conf. Ser., 54, p. 215

Urry, C.M., Padovani, P., & Stickel, M. 1991, *ApJ*, **382**, 501

Urry, C.M., et al. 1993a, Proposal to NASA for observations with Rosat

Vagnetti, F., Giallongo, E., & Cavaliere, A. 1991, *ApJ*, **368**, 366

Vagnetti, F., & Spera, R. 1994, *ApJ*, in press

Wagner, S., Witzel, A., Heidt, J., et al. 1993, *A&A*, submitted

Whitmore, B.C. 1984, *ApJ*, **278**, 61

Wolter, A., Caccianiga, A., Della Ceca, R., & Maccacaro, T. 1994, *ApJ*, in press

Wood, K.S., et al. 1984, *ApJS*, **56**, 507

Worrall, D.M., & Wilkes, B.J. 1990, *ApJ*, **360**, 396

Wurtz, R., Ellingson, E., Stocke, J.T., & Yee, H.K.C. 1993, *AJ*, 106, 869

APPENDIX A

Fits To the Rosat Spectra of Five FSRQs

Rosat Data for five FSRQs of the Pearson & Readhead (1988) sample.

Results of the fits to the Rosat data with a power law with fixed (Galactic) and free absorption (model a1 and a2, respectively):

Column 1: object

Column 2: redshift

Column 3: Galactic N_H

Columns 4, 5: photon index and reduced χ^2 from model a1

Column 5,6,7: fitted absorption, photon index, and reduced χ^2 for model a2

Column 8: Flux at 1 keV from model a1

FSRQs: Fits with the single power law

			N_H fixed (Gal. value)				N_H free				
Object (1)	z (2)	Date (3)	(4)	N_H ($\times 10^{20}$ cm^{-2}) (5)	Γ (6)	χ^2_r/d.o.f. (7)	(8)	N_H (9)	Γ ($\times 10^{20}$ cm^{-2}) (10)	χ^2_r/d.o.f. (11)	Flux$_{1keV}$ (μJy) (12)
0133+476	0.859	Aug 92		11.1	$1.90^{+0.56}_{-0.61}$	0.50/14		$6.79^{+26.82}_{-0.10}$	$1.55^{+1.66}_{-0.95}$	0.45/13	0.27 ± 0.04
0153+744	2.338	Mar 92		23.0	$0.96^{+0.72}_{-0.80}$	0.81/14		54.85 (< 20.44)	$2.46^{+6.94}_{-3.26}$	0.81/13	0.10 ± 0.07
0836+710	2.170	Mar 92		2.92	$1.43^{+0.05}_{-0.09}$	1.06/24		$3.36^{+0.55}_{-0.51}$	1.55 ± 0.15	0.96/23	2.20 ± 0.06
0923+392	0.699	Apr 91		1.53	$2.14^{+0.12}_{-0.13}$	0.60/21		$1.33^{+1.34}_{-0.97}$	$2.05^{+0.55}_{-0.0.46}$	0.61/20	0.37 ± 0.05
1633+382	1.814	Aug 92		1.06	1.58 ± 0.08	1.16/26		$1.89^{+1.00}_{-0.86}$	$1.89^{+0.37}_{-0.0.34}$	1.04/25	0.41 ± 0.03
1641+399	0.595	Jul 90		1.02	2.03 ± 0.09	1.56/24		1.68 (< 8.25)	$1.63^{+0.33}_{-0.19}$	1.32/23	0.41 ± 0.04
2155-15	0.672	Nov 93		3.91	2.27 ± 0.07	0.68/24		$5.09^{+1.76}_{-1.57}$	$2.55^{+0.49}_{-0.46}$	0.60/23	0.22 ± 0.02

APPENDIX B

Bibliography

Publications in Refereed Journals

- Sambruna, R.M., Barr, P., Giommi, P., Maraschi, L., Tagliaferri, G., and Treves, A. 1994, ApJ, in press, *"The X-ray Spectra of Blazars Observed with EXOSAT"*
- Sambruna, R.M., Barr, P., Giommi, P., Maraschi, L., Tagliaferri, G., and Treves, A. 1994, ApJ Suppl., in press, *"The X-ray Spectra of Blazars: Analysis of the Complete EXOSAT Archive"*
- Sambruna, R.M., Barr, P., Maraschi, L., Tagliaferri, G., and Treves, A. 1993, *Ap.J.*, **408**, 452, *"A Spectral Study of Four X-ray Selected BL Lac Objects with EXOSAT"*
- Sambruna, R.M., Chiappetti, L., Treves, A., Bonnet-Bidaud, J.M., Bouchet, P., Maraschi, L., Motch, C., and Mouchet, M. 1991 *Ap.J.*, **374**, 744, *"X-ray to Infrared Observations of the AM Her System E1405-451 (V834 Cen)"*
- Sambruna, R.M., Chiappetti, L., Treves, A., Bonnet-Bidaud, J.M., Bouchet, P., Maraschi, L., Motch, C., Mouchet, M., and Van Amerongen, S. 1992, *Ap.J.* **391**, 750, *"X-ray to Infrared Observations of the Cataclysmic Variable KO Velorum (E1013-477)"*
- Sambruna, R.M. *et al.* 1994, *Ap.J.* **424**, 947, *"Transition in the X-ray Light Curve of the AM Her System E1405-451 (V834 Cen): 1985 – 1986 EXOSAT Observations"*
- Treves, A., Belloni, T., Falomo, R., Fink, H., Maraschi, L., Sambruna, R.M., Tagliaferri, G., and Zimmermann, H.U. 1993, *Ap.J.*, **406**, 447, *"ROSAT Observations of the Blazar PKS 0537-441"*
- Pian, E., Falomo, R., Ghisellini, G., Maraschi, L., Sambruna, R.M., Scarpa, R. and Treves, A. 1994, *Ap.J.*, submitted, *"The Broad-Band Energy Distribution of the Misaligned γ-ray Blazar PKS 0521–365"*

Proceedings of Meetings and Conferences

- Chiappetti, L., Maraschi, L., Sambruna, R.M., and Treves, A. 1989, in Proc. 23 ESLAB Symp., *"Two Topics in X-ray Astronomy"*, ESA SP-296 (Bologna: ESA), 349, *"Is KO Velorum (E1013-477) an Intermediate Polar?"*

- Kollgaard, R.I., Feigelson, E.D., Gabuzda, D.C., Sambruna, R.M., and Urry, C.M. 1994, Proc. of the 2nd ROSAT Meeting, *"X-rays and Relativistic Beaming in Radio-selected BL Lacertae Objects"*

- Sambruna, R.M., Barr, P., Giommi, P., Maraschi, L., Tagliaferri, G., and Treves, A. 1993, 27th ESLAB Symp., *"The X-ray Spectra of Blazars. Analysis of the Complete EXOSAT Archive"*

- Sambruna, R.M. *et al.* 1994, Proc. of the 2nd ROSAT Meeting, *"PSPC Observations of the 1 Jy BL Lacs"*

- Sambruna, R.M. *et al.* 1994, 183rd AAS Meeting, *"Observations of the 1 Jy BL Lacs with ROSAT"*